# Activity patterns in the septal-hippocampal network predict voluntary locomotion

Dissertation

zur

Erlangung des Doktorgrades (Dr. rer. nat.)

der

Mathematisch-Naturwissenschaftlichen Fakultät

der

Rheinischen Friedrich-Wilhelms-Universität Bonn

Vorgelegt von:

**Christian Hannes**

aus Koblenz

Bonn 2017

Angefertigt mit Genehmigung der Mathematisch-Naturwissenschaftlichen Fakultät der Rheinischen Friedrich-Wilhelms-Universität Bonn.

1. Gutachter: Prof. Dr. Stefan Remy
2. Gutachter: Prof. Dr. Walter Witke

Tag der Promotion: 03.05.2018

Erscheinungsjahr: 2018

für meine Eltern

# Contents

Abstract.....

Foreword.....

1. **Introduction**.....1

1.1. Voluntary movement in animals ..... 1

1.2. Behavior and its neuronal representation..... 2

1.3. Basal forebrain ..... 4

1.3.1. The medial septum and the diagonal band of Broca..... 5

1.3.2. Subpopulations and connections ..... 7

1.4. The hippocampal formation..... 8

1.5. Septal-hippocampal network..... 10

1.6. Oscillatory activity in the hippocampus ..... 12

1.7. Central hypothesis ..... 15

2. **Methods**.....17

2.1. Transgenic mouse lines ..... 17

2.2. Surgical procedures ..... 18

2.2.1. Stereotactic injections ..... 18

2.2.1.1. Vectors……..18

2.2.1.1. Cre-loxP system……..19

2.2.2. Chronic implantations ..... 21

2.3. Data acquisition and software ..... 23
2.3.1. Habituation ..... 23
2.3.2. Fiberoptometry ..... 23
2.3.3. Local field potential recordings ..... 23
2.3.4. Multi-unit recordings ..... 24
2.3.4.1. Transcardial perfusion fixation ..... 24
2.3.4.2. Confocal slice microscopy ..... 24
2.4. Data analysis ..... 25
2.4.1. Analysis of locomotion ..... 25
2.4.2. Alignment and slope analysis ..... 28
2.4.3. Analysis of electrophysiological recordings ..... 29
2.4.3.1. Analysis of local field potential recordings ..... 28
2.4.3.2. Analysis of multi-unit recordings ..... 29
2.4.4. Analysis fiberoptometric recordings ..... 30
2.4.5. Modulation analysis ..... 31
2.4.6. Time shift analysis ..... 32
2.4.7. Statistical analysis ..... 33

3. **Results** ..... 35
3.1. In-vivo cell-type specific population activity in the MS ..... 35
3.1.1. Locomotion associated activation of VGluT2$^+$ neurons in the MS ..... 35
3.1.2. Velocity-correlated increases in VGluT2$^+$ population activity ..... 36
3.1.3. Movement-state related VGluT2$^+$ activity occurs prior to onset and deceleration phases ..... 37
3.2. Increased activity in MS PV neurons during episodes of movement ..... 39
3.2.1. Changes in PV$^+$ population activity correlated to the speed ..... 40

3.2.2. Onset and offset of locomotion is represented in the activity of septal $PV^+$ neurons ..... 41

3.3. In-vivo monitoring of oscillatory activity in hippocampal CA1 stratum pyramidale 44

3.3.1. Power and peak frequency of HC CA1 LFP increased in theta range ..... 44

3.3.2. Frequency specific representation of locomotion in hippocampal CA1 pyramidal layer ..... 46

3.3.3. Hippocampal theta oscillations increase in both peak frequency and amplitude in correlation to the movement speed ..... 48

3.3.4. Hippocampal theta oscillation frequency bands contain information on changes in the movement state ..... 50

3.4. Intraseptal neuronal ensemble activity represents movement ..... 52

3.4.1. MS unit activity heterogeneously modulated by velocity ..... 54

3.4.2. Theta coupling in MS single-units ..... 54

3.4.3. MS multi-unit activity heterogeneously encodes movement phases ..... 57

3.4.4. MS single-units predict future movement states ..... 59

3.5. HC CA1 unit firing increased during running ..... 60

3.5.1. HC single-units display diverse speed-modulation ..... 60

3.5.2. Single-units in HC CA1 coupled to theta phase and frequency ..... 63

3.5.3. Hippocampal multi-unit activity predicts the onset of locomotion ..... 65

3.5.4. A small proportion of units in HC CA1 predict upcoming movement states 65

3.6. Kinetics of hippocampal theta oscillation’s amplitude and peak frequency predictively change prior to the velocity ..... 68

3.7. Locomotion predictively encoded in a subset of neurons in the MS ..... 70

3.8. Predictability of locomotion on the basis of single-unit activity in HC CA1 ..... 72

4. **Discussion** ..... 75

4.1. Movement associated activity in the MS ..... 76

4.1.1. Population activity of VGluT2$^+$ and PV$^+$ neurons in the MS display a movement related increase in activity ..... 76

4.1.2. Unit activity in the MS is heterogeneous during locomotion ..... 80

4.2. Movement associated activity in the hippocampal CA1 region ..... 82

4.2.1. HC CA1 theta amplitude and peak frequency increase during running ..... 82

4.2.2. Hippocampal units are diversely activated during locomotion ..... 84

4.3. Predictive encoding of locomotion ..... 87

5. **Conclusion** ..... 91

6. **Appendix** ..... 93

6.1. Abbreviations ..... 93

6.2. Contributions ..... 96

7. **Bibliography** ..... 97

# List of figures

**Figure 1**: Hierarchical organization of the motor system in mammals from the central nervous system to the periphery ..... 2
**Figure 2**: Scheme of parameters investigated in this study ..... 4
**Figure 3**: Basal forebrain nucleus MSDB forming a highly effective micro network ..... 6
**Figure 4**: Anatomical organization in the hippocampal formation and tri-synaptic circuit 9
**Figure 5**: Septal-hippocampal connectivity map ..... 11
**Figure 6**: Recurrent intrahippocampal network generates oscillatory activity ..... 13
**Figure 7**: Illustration of cre-dependent expression of virally transferred constructs in neurons ..... 20
**Figure 8**: Principle of a mono fiber-optic cannula ..... 21
**Figure 9**: Scheme illustrating locations of chronic implants ..... 22
**Figure 10**: Illustration of distinct states during a movement phase and functional criteria ..... 27
**Figure 11**: Exemplary slope analysis of a parameter prior to an alignment point ..... 28
**Figure 12**: Mathematical description of oscillations in local field potential recordings ... 29
**Figure 13**: Illustration of a time shift analysis for a parameter against the corresponding velocity ..... 32
**Figure 14**: VGluT2-GCaMP5G transients increase during locomotion ..... 36
**Figure 15**: VGluT2-GCaMP5G fluorescence is positively correlated to the velocity of locomotion ..... 37
**Figure 16**: Movement related VGluT2-GCaMP5G transients display state specific changes during onset and deceleration ..... 38
**Figure 17**: PV-GCaMP5G fluorescence increases during locomotion ..... 40
**Figure 18**: PV-GCaMP5G fluorescence is positively correlated to the velocity of locomotion ..... 41
**Figure 19**: Movement related PV-GCaMP5G transients display state specific changes during onset and termination phases ..... 42
**Figure 20**: Theta oscillation power and peak frequency increase during locomotion .... 45
**Figure 21**: HC Theta frequency bands change in amplitude during locomotion ..... 46
**Figure 22**: Theta oscillations are positively correlated to the velocity of locomotion ..... 48

**Figure 23**: Theta frequency band-specific changes during states of movement ..... 51
**Figure 24**: MS unit firing frequency shows dependence on locomotor activity..... 53
**Figure 25**: Global MS unit activity sensitive to changes in velocity ..... 55
**Figure 26**: MS single-unit firing is modulated by speed and theta..... 56
**Figure 27**: Global MS unit activity heterogeneously adapts to the state of locomotion . 58
**Figure 28**: Individual MS units change their firing frequency prior to change in locomotion ..... 59
**Figure 29**: Elevated AP firing rates in HC neurons during locomotion ..... 61
**Figure 30**: Global HC unit activity sensitive to changes in velocity ..... 62
**Figure 31**: Distinct modulation of HC CA1 single-unit firing ..... 64
**Figure 32**: Hippocampal multi-unit activity predicts the start of movement ..... 66
**Figure 33**: Movement state prediction of single-units in hippocampal CA1..... 67
**Figure 34**: Time shift analysis reveals different time points of highest prediction for individual theta bands..... 69
**Figure 35**: AP firing rates of septal single-units predict locomotor behavior..... 69
**Figure 36**: AP firing rates of hippocampal single-units reliably predict locomotion..... 74

# List of tables

**Table 1**: List of mouse lines used in this study ..... 17
**Table 2**: Stereotactic coordinates of brain regions targeted in this study ..... 19
**Table 3**: List of viral vectors used in this study ..... 20
**Table 4**: Functional definition of movement phases ..... 26

# Abstract

In the brain of animals, locomotion is encoded and represented in multiple ways. During locomotion, the hippocampus (HC) displays characteristic activity patterns that change from asynchronous states when the animal is resting to synchronous rhythmic activity during movement. The increase in firing rates of principal neurons in CA1 and the presence of oscillations in the HC both correlate to the velocity of the animal. It has been shown previously that glutamatergic neurons in the medial septum (MS) increase their activity prior to movement onset. However, the time-course of activation of individual MS neuron types during an episode of locomotion is unknown.

I investigated the MS-HC circuitry with cell-type specificity by expressing the genetically encoded calcium indicator GCaMP5G in inhibitory ($PV^+$) and excitatory ($VGluT2^+$) cells of the MS. I have monitored activity-dependent changes in fluorescence with a fiberoptometer coupled to an implanted fiber optic cannula in head fixed mice on a linear treadmill. In addition, I obtained CA1 local field potentials and recorded multi-unit activity in both CA1 and the MS. I aligned and correlated the recorded parameters with different phases of locomotion (onset, acceleration, deceleration, offset). My results show that there is a significant representation of locomotion in both CA1 and MS neuronal populations. I demonstrate that both glutamatergic $VGluT2^+$ and GABAergic $PV^+$ cells in the MS show an increase in activity several hundred milliseconds before movement.

My experiments provide evidence on the single neuron activity level for CA1 and MS cellular activity that predicts movement onset. A simultaneous activation of glutamatergic and GABAergic neurons within the MS suggests the activation of an excitatory-inhibitory feedback loop controlling motion execution and HC information processing.

# Foreword

“That’s one small step for [a] man, but a giant leap for mankind.” (Neil Armstrong, 1969)

Every step on the moon and every step on earth is controlled by our brain. While sensory systems gather information about our surroundings, movement is the only ability we possess to interact with the environment. Understanding how the brain initiates and controls movement, how the initial idea of a movement is created, and how distinct movements are fine-tuned and finally executed is one of the big tasks of our field. Up to now we still lack profound knowledge of the neuronal basis underlying this seemingly primitive behavior.

Modern neuroscience is focusing more and more on the connectivity of neurons rather than investigating properties of the individual cells. Therefore the term of *neuronal networks* has become a part of the neuroscientific landscape. By manipulating and monitoring neuronal networks we might one day be able to control and predict movement in animals. Moreover, we will be able to understand how neuronal dysfunction in various brain regions effecting locomotion can lead to movement disorders. The ultimate goal is to develop better treatments for disorders such as Parkinson’s disease.

This work is based on the assumption that if we want to understand a behavior we have to find the neuronal correlates underlying this behavior. Even though this project cannot give a general answer to this big question it still may shed some light on it.

And step by step we are getting closer to know.

Ancient Egyptian Sign for Brain from 17$^{th}$ century BC

(Breasted JH (1930): The Edwin Smith Papyrus. University of Chicago Press. 2)

# 1. Introduction

## 1.1. Voluntary movement in animals

In order to interact with the environment, animals depend on their ability to move. In higher animals respiration, chewing, digestion, and even the heartbeat are regulated by the autonomic nervous system while voluntary locomotion is controlled by the central nervous system (Campbell and Reece, 2006). Even single-cell organisms rely on equivalent subcellular features which enable them to move (Jahn and Votta, 1972) as locomotion is the only possibility to interact with an environment.

Locomotion in vertebrates is encoded and represented in multiple ways within the brain. Elementary movement circuits are organized by nuclei of the brain stem and the spinal cord. In mammals, the voluntary and goal-driven locomotor system is structured hierarchically into motor cortex, motor areas in the brain stem, and the spinal cord (Kandel et al., 2000). The ultimate origin of movement, the “initial command” to perform any behavior is still unknown. Yet, studies in humans have shown that there is a clear dissociation between preparation and initiation of movement implying adaptions of encephalic activity prior to the first physical output (Haith et al., 2016). In this regard, the primary motor cortex (PMC) is the central region that transmits signals to the spinal cord and to subsequent muscles evoking voluntary movement (Sherrington, 1906). Many brain regions downstream of the PMC affect locomotor activity (**Figure 1**). The cerebellum, the basal ganglia, and prefrontal cortical areas (Purves et al., 2001) project to the PMC and pathological studies have given proof for their involvement in movement production (Delmaire et al., 2007; Neychev et al., 2008; Pawela et al., 2017). By sending feedback signals to the PMC and relevant brain stem areas (Holmes, 1917; Kemp and Powell, 1971), the cerebellum and the basal ganglia compare the intended movement to the actual movement in real-time. Patients with severe damage in these areas suffer from an inability to reduce such discrepancies, thereby displaying coordination deficits (Purves et al., 2001). The prefrontal cortex (PC) upregulates rhythmic activity in brain regions associated with the integration of sensory information (Vanderwolf, 1969; Buzsaki et al., 1983). These peripheral inputs originating from the visual system, the vestibule-cochlear system, or the proprioceptive system contain important information for both PMC and associated feedback regions and are crucial for the successful execution and adaption of movement

(Salinas and Romo, 1998; Hooks et al., 2015). Damage to the feedback projections from the basal forebrain to the PMC severely impairs cognitive behavior tasks like navigation or spatial learning (Hagan et al., 1988) as well as associative learning (Roland et al., 2014).

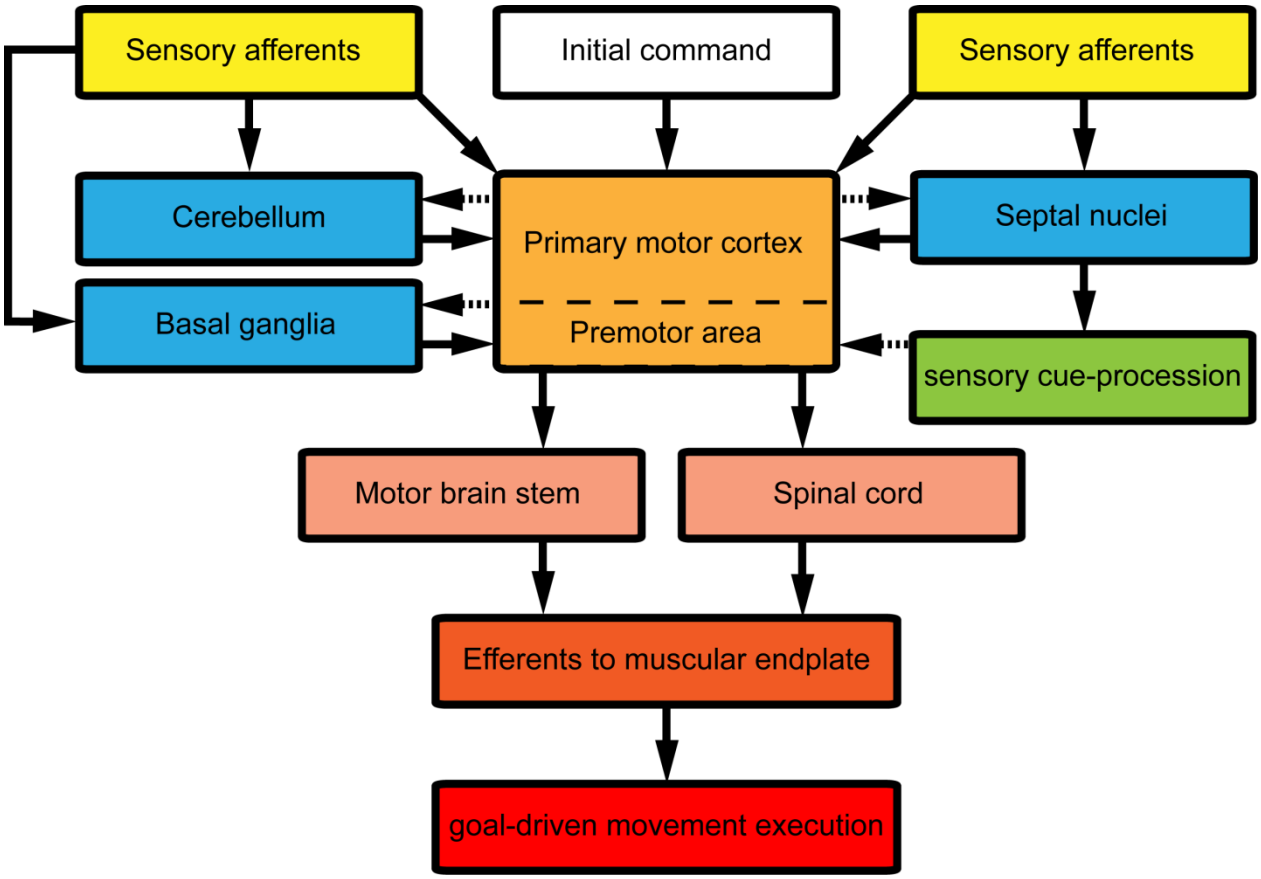


**Figure 1:** Hierarchical organization of the motor system in mammals from the central nervous system to the periphery

## 1.2. Behavior and its neuronal representation

Studying and understanding the neuronal correlates of behavior is a major challenge in modern neuroscience. To do so, it may be important to consider a neuron not as an isolated entity, but to understand it as a part of a neuronal network. Therefore, behavioral studies in animals require simultaneous recording of coherent parameters that can be correlated and linked to each other, as well as to the behavior itself (**Figure 2**). The links between the electrophysiological processes within single neurons and the network

signaling within the brain are extremely complex. On the one hand, a single cell view focusses on the microscopic scale, ignoring the magnitude and diversity of neuronal processing. On the other hand, studying a single aspect of movement does not do the complexity of this matter justice. Considering neuroscientific findings such as spatially dependent neuronal depolarization (O'Keefe and Conway, 1978), we begin to understand the magnitude and the diversity of the brain as a network.

The neuroscientific toolbox has rapidly expanded during the last century. The population activity within brain regions can now be monitored by using genetically encoded calcium indicators (GECIs), e.g. GCaMP. Upon excitation cells expressing these proteins emit fluorescence when the intracellular calcium concentration ($Ca^{2+}$) increases (Mank and Griesbeck, 2008). The influx of calcium via voltage-sensitive and ligand-gated $Ca^{2+}$-channels correlates directly to the activation of AMPA/NMDA receptors and can be used as a proxy for cellular activity. Electrophysiological recording of local field potentials (LFP) and monitoring of neuronal action potential (AP) output with electrodes inserted into neuronal tissue are additional valuable tools for detection of neuronal network activity. The LFP signal (see chapter 1.6) represents a summation of electrical currents flowing in the close area around the electrode as a result of synaptic activity. AP firing of multiple cells can be monitored by using multi-unit electrodes which record electrical currents in a much smaller area due to a smaller contact area with the surrounding neuronal tissue (Legatt et al., 1980). Combining these methods in this study sets the basis for a correlation of electrical brain activity in distinct areas with behavior (**Figure 2**). Additionally, by manipulating parts of a neuronal network the functional principles of the system can be investigated. These manipulations can be conducted by pharmacologically blocking or activating receptors or channels (e.g. by using a $GABA_A$ agonist like Muscimol), or by activation of light sensitive proteins such as channelrhodopsin or halorhodospin. The activity of these proteins (“opsins”) can be controlled by light of a defined wavelength. They can either mediate inward or outward ion flux (Nagel et al., 2002; Mattis et al., 2011). This study used the GECIs for detailed investigation and monitoring of cellular activity without manipulating network activity.

The list of activity indicator proteins is long and constantly increases in size. Moreover, in-vivo electrophysiology has developed up to a state that recordings in the intact and

behaving animal are possible from thousands of neurons (Alivisatos et al., 2013; Jun et al., 2017). But further progress on the toolbox is made on a daily basis and our experiments are mostly limited by our scientific imagination only.

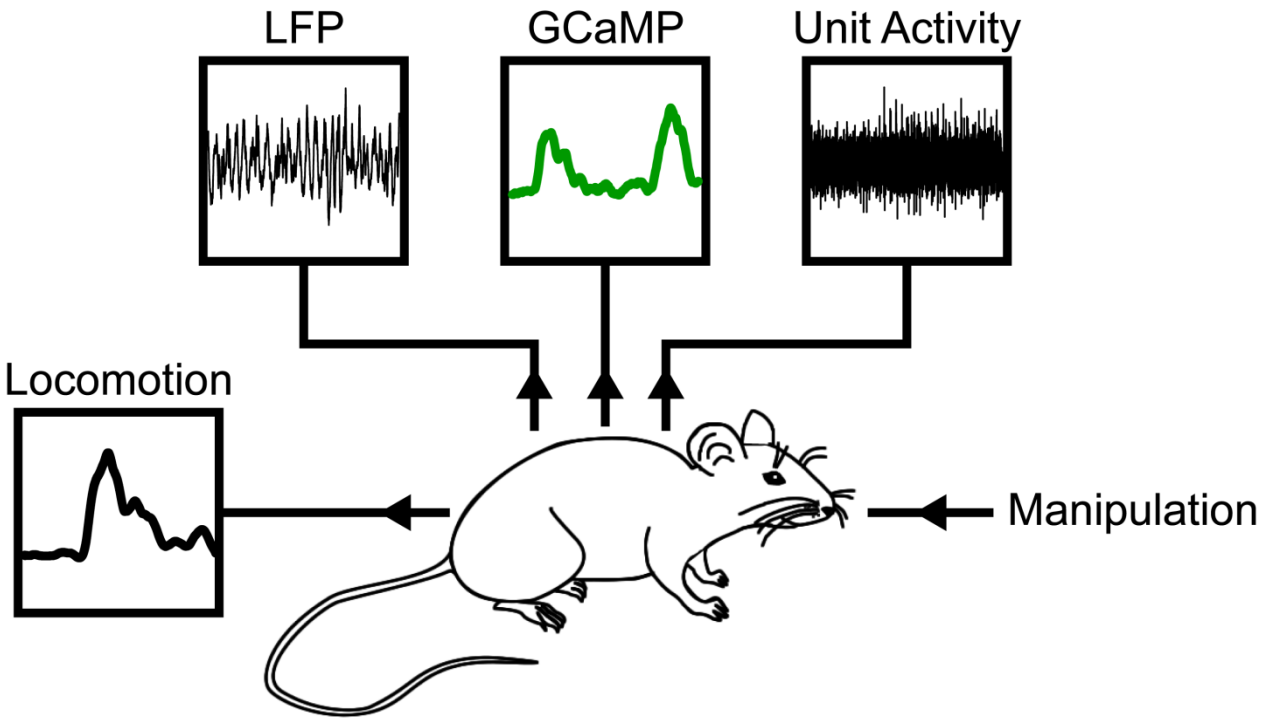


**Figure 2:** Scheme of parameters investigated in this study

In this study different parameters were recorded simultaneously during locomotion: the local field potential (LFP) and the fluorometric signal of a genetically encoded Ca2+ marker protein (GCaMP) were monitored as readout of electrical population activity; the action potential (AP) frequency of individual neurons was recorded as the unit activity in a population of cells; manipulations such as pharmacological blocking of synaptic transmission or optogenetic control of neuronal activity were not used in this study.

### 1.3. Basal forebrain

The basal forebrain consists of several nuclei. Together with other brain regions such as the locus coeruleus (LC), the parabrachial nucleus, and the raphe nucleus it belongs to an ascending arousal system (Kandel et al., 2000). The basal forebrain can be subdivided into septal nuclei, the diagonal band of Broca (DB), and the nucleus basalis. The major

output is mediated via cholinergic neurons while GABAergic and glutamatergic populations have also been described as relevant (Sotty et al., 2003). Each functionally distinct region in the basal forebrain with special subpopulations of neurons connects to different target areas. For instance, the medial septal nucleus (MS) mainly innervates the hippocampal formation (HCF), whereas the DB is intensively connected to the HCF and the cingulate cortex (Gritti et al., 1993). The nucleus basalis forms strong projections to the neocortex and amygdala (Mayse et al., 2015). The presence of highly heterogenic magnocellular corticopetal projection neurons allows the basal forebrain to play an important role in a variety of tasks (Zaborszky et al., 1999). These connections keep the target regions in a state which enables fast and appropriate reactions to incoming sensory information by boosting or inhibiting neuronal activity in the affected target regions (Gritti et al., 1993; Gritti et al., 2003).

### 1.3.1. The medial septum and the diagonal band of Broca

Located in the central part of the basal forebrain (**Figure 3A**), the MS and the DB are strongly innervated and massively projecting central nuclei, together referred to as MSDB (**Figure 3B**). Its medial localization and its dorsal-ventral extension support relaying various inputs and outputs throughout the whole brain (Kandel et al., 2000). Efferents of MSDB cells exit the septal nucleus via the dorsal fornix-fimbria, the medial forebrain bundle, or the stria medullaris (Meibach and Siegel, 1977a). Primary targets of these projections (**Figure 3D**) are the hypothalamus, the habenular nucleus, and the HCF, the latter receiving the strongest input (Kohler et al., 1984; Frotscher and Leranth, 1985; Freund and Antal, 1988). Furthermore, synaptic terminals of MSDB neurons can be found in the lateral septum (LS) and the ventral tegmental area (VTA;(Meibach and Siegel, 1977a; Lynch et al., 1978; Unal et al., 2015). Mono-transsynaptic tracing experiments identified the hypothalamic nuclei including the supramammillary nuclei, the preoptic nuclei, the periventricular nuclei, and the median raphe nucleus as the main input regions to the MSDB (Swanson and Cowan, 1979; Fuhrmann et al., 2015). Due to this strong connection between the MSDB and the rest of the brain it is suggested to function as a relay station involved in the procession of sensory information (Swanson and Cowan, 1979; Wallenstein and Hasselmo, 1997).

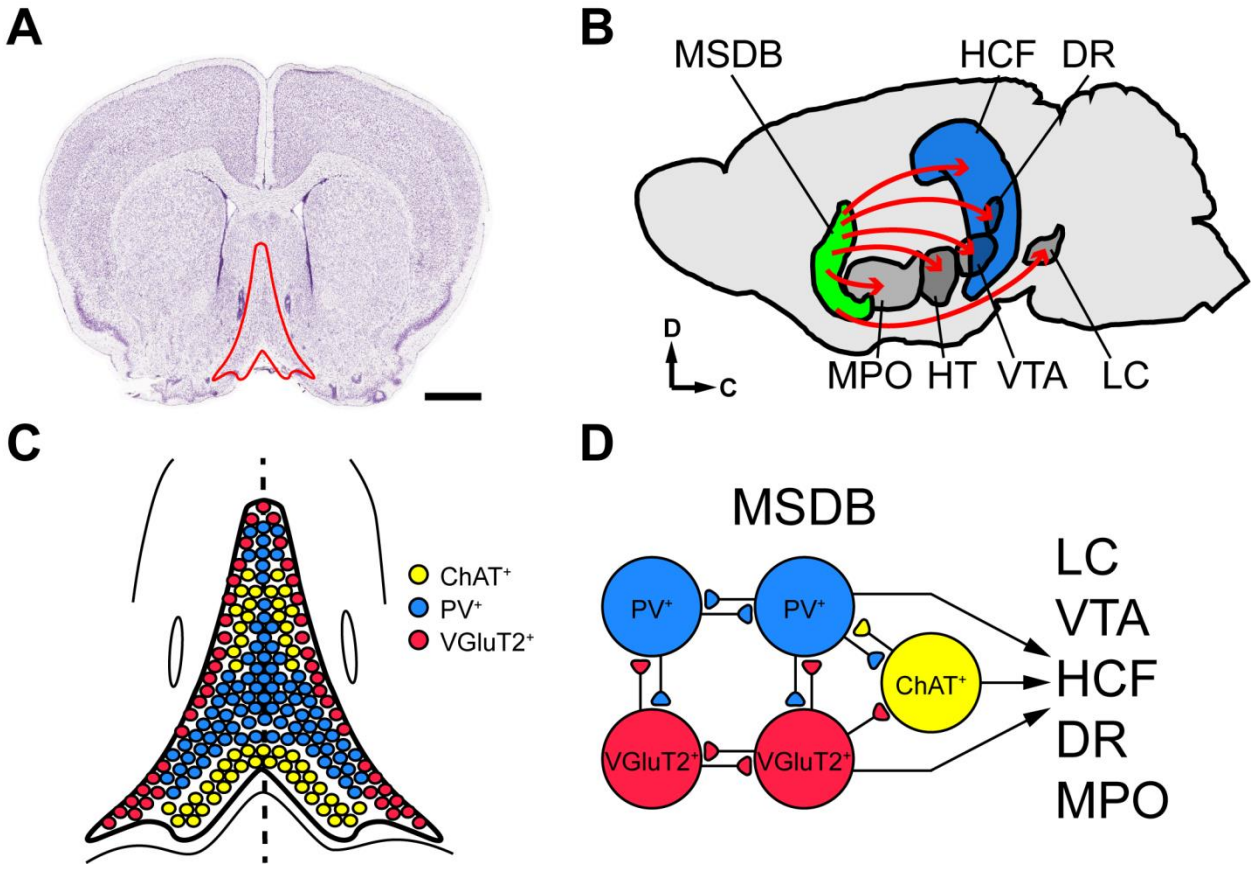


**Figure 3:** Basal forebrain nucleus MSDB forming a highly effective micro network

**A** Nissl staining of a brain section depicting the MSDB region (red outline; modified from: Allen Institute); scale bar = 1 mm. **B** Scheme displaying MSDB localization in the basal-frontal parts of the rodent brain and its main efferents (inspired by Swanson & Cowan, 1979); MSDB medial septum and diagonal band of Broca, HCF hippocampal formation, DR dorsal raphe, MPO medial preoptic area, HT hypothalamic area, VTA ventral tegmental area, LC locus coeruleus; D dorsal, C caudal. **C** Schematic distribution of MSDB neuron populations, displaying ChAT$^+$ (yellow), PV$^+$ (blue), and VGluT2$^+$ (red) neurons (inspired by Kiss et al., 1997). The dashed line indicates the medial line. **D** Illustration of the MSDB micro network and target regions (inspired by Manseau et al., 2005; Fuhrmann et al., 2015); colors as in C.

The MSDB transmits a speed-signal to downstream regions adjusting the general excitability to a state of increased excitability (Fuhrmann et al., 2015; Hinman et al., 2016; Justus et al., 2017). Studies have shown that the MSDB is crucially involved in proper execution of spatial navigation, learning tasks, and locomotion per se (Hagan et al., 1988; Sutherland and Rodriguez, 1989; Fuhrmann et al., 2015). During these behaviors rhythmic oscillations of the LFP in the range of 4 to 12 Hz (theta oscillation) can be

observed in the HCF. These rhythms are thought to be partially generated by rhythmic activity in MS neurons (Buzsaki, 2002). Studies involving lesions in the MS showed that disturbing the connection between MS and HCF leads to severe impairment of spatial representation in the HCF (Leutgeb and Mizumori, 1999). A short inactivation of the MS is sufficient to eliminate theta in the HCF. Simultaneously, such a manipulation disrupts existing spatial maps in the hippocampus (HC) and the entorhinal cortex (EC). Moreover, new and highly distinct and stable spatial activity patterns are formed immediately (Brandon et al., 2014).

### 1.3.2. Subpopulations and connections

Several distinct neuronal subpopulations have been reported in the MS, which form functional intraseptal networks (Hajszan et al., 2004; Halasy et al., 2004). These subsets of cells differ significantly from each other with respect to their anatomical localization, their molecular composition, and their physiology (**Figure 3C**). Immunohistochemically, four subpopulations can be defined: choline-acetyl-transferase positive ($ChAT^+$), parvalbumin positive ($PV^+$), and vesicular glutamate transporter 1/2 positive ($VGluT2^+$) cells (Kiss et al., 1990; Kiss et al., 1997; Manseau et al., 2005). $VGluT2^+$ neurons are mainly localized in the DB and at the MS/LS border and display very low spontaneous firing episodes. The $PV^+$ neurons are highly abundant in the central parts of the MS, delivering firing bursts to intra- and extraseptal targets. The $ChAT^+$ neurons are distributed more medial (**Figure 3C**) and display the highest rhythmicity in their firing (Kiss et al., 1997; Hajszan et al., 2004; Halasy et al., 2004; Leao et al., 2012; Leao et al., 2015).

Intraseptally, $VGluT2^+$ neurons release glutamate onto other $VGluT2^+$ cells, $ChAT^+$, and $PV^+$ cells. The latter form reciprocal connections onto $VGluT2^+$ neurons and connect to $ChAT^+$ cells in the MSDB. $ChAT^+$ neurons have been shown to release acetylcholine onto MSDB $PV^+$ cells (**Figure 3D**) while a direct connection to $VGluT2^+$ neurons is not described (Manseau et al., 2005; Leao et al., 2015; Mysin et al., 2015). All cell types project onto neurons in various target regions including the HCF. The combination of rhythmic septal-hippocampal GABAergic and excitatory glutamatergic input onto hippocampal neurons is thought to play an important role for the control of hippocampal

field activity. On the other hand, septal choline release mediates slow depolarization of neurons in the HC (Colom et al., 2005).

## 1.4. The hippocampal formation

The HCF is essential for spatial learning, memory consolidation as well as sensory processing. In humans, this region is thought to be crucial for maintaining our quality in life. The HCF has been in the focus of many studies dealing with neurodegenerative diseases such as Alzheimer's disease, epilepsy, and Parkinson's disease that link pathologies in the HCF to behavioral deficits such as learning deficits, disorientation, and memory formation impairment (Stephan et al., 2001; Costa et al., 2012).

The HC and the adjacent parahippocampal regions, the subiculum (SC) and the EC are subregions of the HCF. During embryonal development the HC is derived from medial parts of the telencephalic vesicle. Its final orientation in the temporal lobe (**Figure 4A**) depends strongly on developmental processes and differs among species (Caronia-Brown et al., 2014). This precursor structure differentiates into the cornu ammonis (CA) and the tooth-shaped dentate gyrus (DG). Defined by Lorente de Nó in 1934 (Lorente de Nó, 1934), the CA contains the molecular distinct areas CA1, CA2, and CA3 (**Figure 4B**). The neuroanatomy of the CA regions (**Figure 4C**) is strictly organized in layers (Andersen et al., 2007). The *alveus* is located on the surface of the stratum oriens (s.o.) and contains the fibers of the major efferent outputs of the HC. Containing only few cells, the s.o. is located below the alveus. Yet, this layer contains different types of interneurons (Freund and Buzsaki, 1996; Andersen et al., 2007). In addition, the axons and basal dendrites of pyramidal cells from the subjacent stratum pyramidale (s.p.) reach out into the outer s.o. The cell bodies of these principal neurons are densely packed in the s.p. Below the s.p. the stratum radiatum (s.r.) is located.

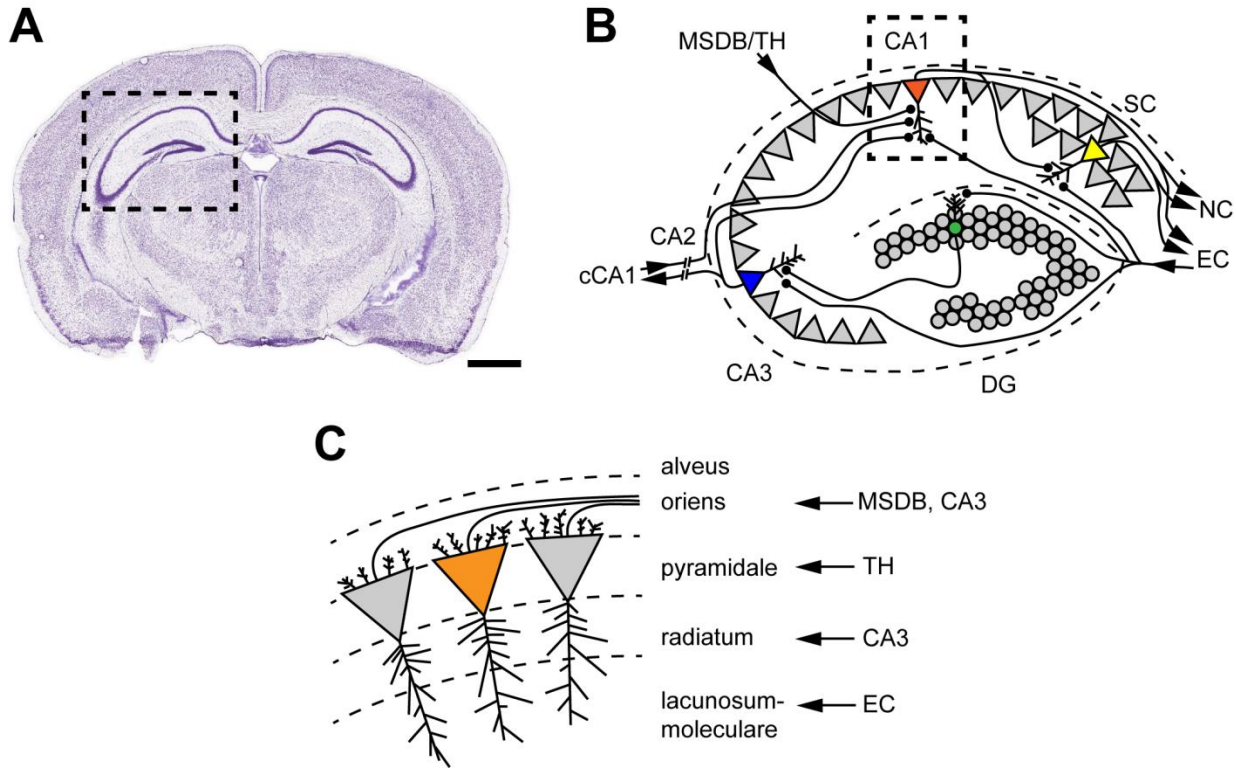


**Figure 4:** Anatomical organization in the hippocampal formation and tri-synaptic circuit

**A** Nissl staining of a coronal brain section containing the hippocampal formation (modified from: Allen Institute). **B** Magnification of the box in A: scheme of the hippocampal formation (HCF), consisting of the dentate gyrus (DG), the cornu ammonis 3 (CA3), the cornu ammonis 2 (CA2), the cornu ammonis 1 (CA1), and the subiculum (SC). Connections are shown for granule cells in DG (green) and pyramidal cells in CA3 (blue), CA3 to CA1 (orange), CA1 to SC (yellow), and SC to neocortex (NC). Well described inputs to the HCF originate from entorhinal cortex (EC), medial septum and diagonal band of Broca (MSDB), and thalamus (TH); projections terminate in the contralateral CA1 (cCA1), EC, and the neocortex (NC). **C** Magnified inset from A; layered structure of hippocampal CA regions consisting of stratum oriens (s.o.), stratum pyramidale (s.p.), stratum radiatum (s.r.), and stratum lacunosum-moleculare (s.l.m.). The soma of pyramidal cells in CA1 are located in the s.p.; the apical dendritic tree reaches out to s.r. and s.l.m.; the basal dendrites and the axon face to s.o. Inputs from CA3 terminate in s.o. and s.r., inputs from TH terminate in s.p., synapses from EC cells are located in s.l.m. Scale bar in A: 1 mm.

This suprapyramidal layer contains most of the apical dendritic arbor and by this receives most afferents (Lynch et al., 1978). Subjacent to s.r. is the stratum lacunosum-moleculare (s.l.m.), a layer that receives significant input from EC (Deadwyler et al., 1987). This pattern in CA is different from the three layers in the DG. Here, the most superficial layer close to the hippocampal fissure is called the molecular layer (m.l.) which contains only

few cells. Deep within the m.l. is the granule cell layer (g.c.l.) containing the principal neurons in the DG (Andersen et al., 2007). Together, the g.c.l. and its surrounding m.l. are referred to as the *fascia dentata*. The EC, CA3, and CA1 are unidirectionally linked in the tri-synaptic circuit (Andersen et al., 2007). In this micro network, cells in the EC project onto granule cells in the DG which is referred to as the *perforant path*. Excited granule cells send signals to pyramidal cells in CA3 via the so called *mossy fibers*. The axons of CA3 neurons which transmit the excitation further onto pyramidal cells in CA1 are called *Schaffer collaterals* (**Figure 4B**) and terminate both in s.o. and s.r. (Andersen et al., 2007; Stepan et al., 2015). In addition to this circuit, there are more synaptic connections linking the HC to various brain regions. The *temporoammonic pathway* mediates the direct synaptic input from EC to CA1, forming synapses mainly in s.l.m.; subcortical afferents from MSDB and thalamus (TH) to the HC terminate in CA1 s.o., and inputs from the contralateral CA3 to ipsilateral CA1 are mediated via the *associational commissure*, terminating in s.r. (Doherty, 1999; Witter et al., 2000; Hartley et al., 2014). There is also evidence for monosynaptic connectivity between CA3 to EC (Agster and Burwell, 2013).

### 1.5. Septal-hippocampal network

The MSDB in the basal forebrain and the HCF are strongly interconnected to each other (**Figure 5A**). This network is part of the sensory integration system of the central nervous system and it adjusts its network activity depending on the behavioral state (Deadwyler et al., 1987; Fuhrmann et al., 2015; Justus et al., 2017). The MSDB directly influences the general activity of cells in the CA1 region of the hippocampus and controls the occurrence and intensity of rhythmic activity in the respective areas (Bland and Bland, 1986). This modulation is mediated by neurons in the MSDB that are connected to different cell populations in the dorsal CA1 (Meibach and Siegel, 1977a, b; Wainer et al., 1985; Nyakas et al., 1987). Hippocampal afferents originating from the MS release acetylcholine (Lewis and Shute, 1967), GABA (Kohler et al., 1984), and glutamate (Sotty et al., 2003), activating respective receptors in the HC (**Figure 5B**). $PV^+$ neurons in the MS fire at high frequency and evoke strong inhibition in hippocampal interneurons and pyramidal cells (Sun et al., 2014). Activity of MS $ChAT^+$ projections into the HC increases excitability of hippocampal pyramidal neurons by slow depolarization (Frotscher and Leranth, 1985).

The synapses of MS VGluT2$^+$ neurons release glutamate onto hippocampal interneurons and pyramidal neurons which has recently been described as a key element in the regulation of hippocampal activity (Sotty et al., 2003; Huh et al., 2010; Robinson et al., 2016). This connection is suggested to be crucial for the generation of theta oscillations in the HC (Fuhrmann et al., 2015) which are important to the integration of various sensory cues during behavior such as locomotion (Deadwyler et al., 1987).

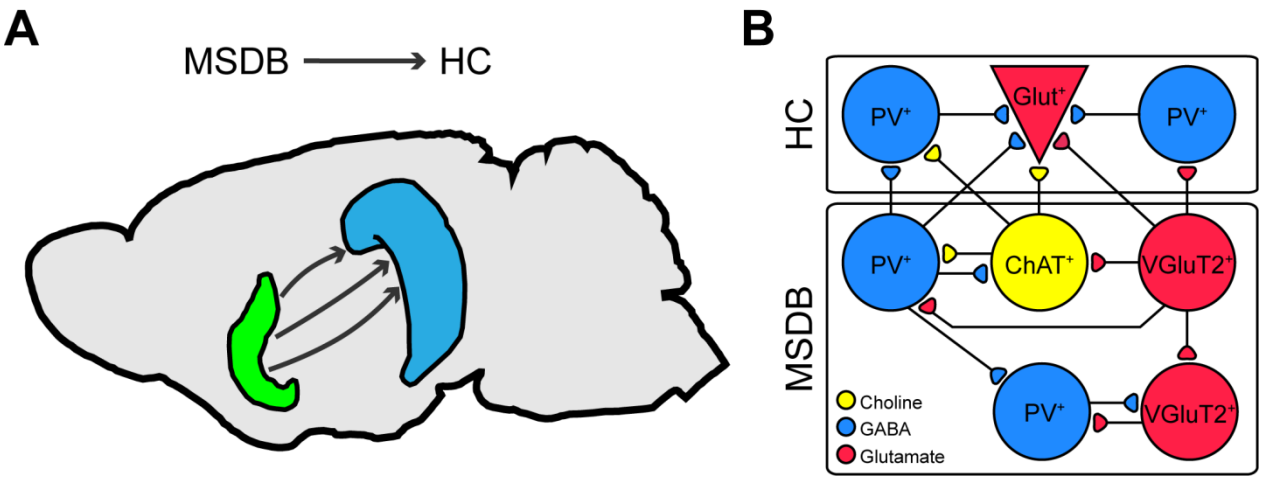


**Figure 5:** Septal-hippocampal connectivity map

**A** Schematic localization of the MSDB (green) sending projections to the HC (blue). **B** Illustration of intraseptal/intrahippocampal and MSDB-HC connectivity, including ChAT$^+$ (yellow), PV$^+$ (blue), and VGluT2$^+$ (red) neurons in both brain regions. ChAT$^+$ neurons release choline, PV$^+$ neurons release GABA, and VGluT2$^+$ neurons use glutamate as neurotransmitter (inspired by Sun et al., 2014).

The MS-HC connection has also been shown to play an important role in the generation of place fields, sequential learning, and phase precession (Wallenstein and Hasselmo, 1997). Septal lesion experiments have exposed behavioral deficits (see chapter 1.3). These findings underline the importance of the MS-HC connectivity for theta generation and resulting behavior (Green and Arduini, 1953; Stewart and Fox, 1990).

## 1.6. Oscillatory activity in the hippocampus

Sensory information during behavior passes the HC before it reaches the cortex (Green and Arduini, 1953). To deal with the flow of information the HC adjusts its general state of activity depending on the current requirements (Buzsaki, 1986). Electroencephalographic monitoring of hippocampal activity revealed the presence of rhythmic slow activity (RSA or theta oscillation) during episodes of voluntary movements such as locomotion or manipulations of objects (**Figure 6A**), as well as during REM sleep (Winson, 1972; Buzsaki, 1986). In contrast, irregular hippocampal activity patterns were found during periods of immobility, alertness, and elementary movements such as chewing or lapping water (Vanderwolf, 1969; Whishaw and Vanderwolf, 1971). Similar rhythmic theta activity was also described to be present in many other structures throughout the brain like cingulate cortex and amygdala (Leung and Borst, 1987; Pare and Collins, 2000). Using pharmacological approaches, two types of theta oscillations could be defined: the atropine-sensitive, low frequency oscillation type I theta and the atropine-insensitive, fast frequency oscillation type II theta (Kramis et al., 1975). The frequency of the oscillation is determined by the MSDB which is also referred to as the pacemaker of theta oscillations (Meibach and Siegel, 1977a, b; Holsheimer et al., 1982; Buzsaki et al., 1983). Inactivation of the MSDB resulted in complete abolishment of theta in rabbits, implying that the MSDB is the ultimate generator of theta (Petsche et al., 1962). Theta activity is defined as an oscillation ranging from 4-12 Hz in frequency and can increase its amplitude 4-fold compared to the baseline (Whishaw and Vanderwolf, 1973). Even though the exact control mechanisms of theta oscillation remains enigmatic, recent studies suggest a crucial role of VGluT2$^{+}$ neurons (Fuhrmann et al., 2015; Robinson et al., 2016). The repetitive occurrence of electrical currents in CA1 pyramidal cells underlying theta oscillations (**Figure 6A**) is mainly generated by inputs received via the perforant path (originating from EC), the Schaffer collaterals (arising from CA3), and dendritic voltage-dependent currents (Skaggs et al., 1996). CA3 neurons provide the strongest theta drive by coherently exciting CA1 pyramidal cells (Csicsvari et al., 2003). This rhythmicity is caused by a recurrent connection between CA3 pyramidal cells and DG mossy cells creating an intrahippocampal oscillator (**Figure 6B**).

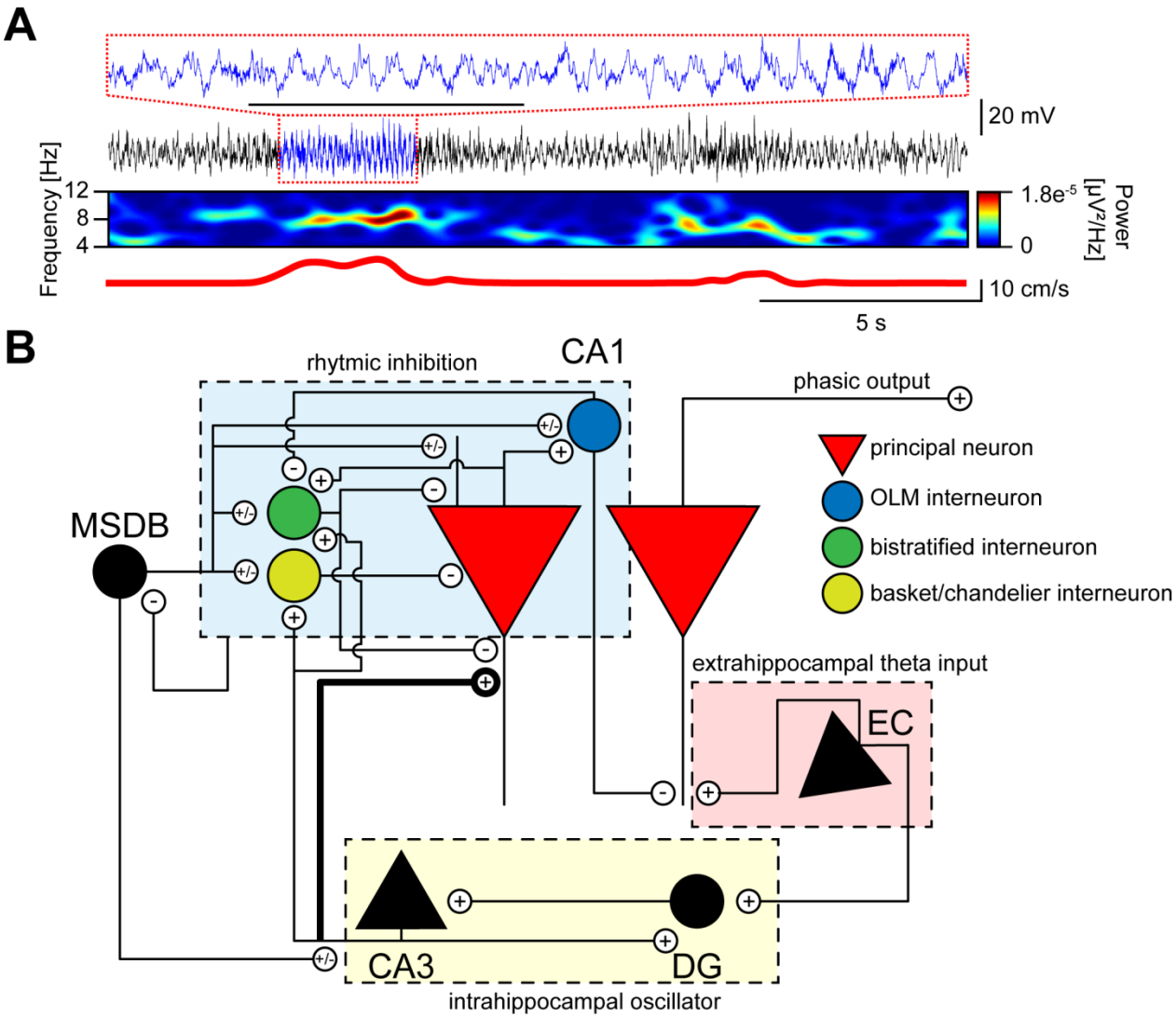


**Figure 6:** Recurrent intrahippocampal network generates oscillatory activity

**A** Recorded raw LFP signal (blue, magnified from black, scale bar indicates 1 s), the calculated power spectrum and the corresponding changes in velocity (red) are shown below. **B** CA1 pyramidal cells (red) receive rhythmic extrahippocampal excitatory input from EC layer II/III neurons, excitatory MSDB neurons, and CA3 cells. The strongest theta drive (thick black line) originates from CA3 pyramidal cells. These cells form a recurrent network with mossy cells in DG, representing the intrahippocampal oscillator (light yellow box) and depending on cholinergic input which possibly originates from the MSDB. CA1 pyramidal cells receive MSDB inhibition and excitation. Rhythmic inhibition (light blue box) is mainly created by MSDB stimulation of CA1 OLM (blue), bistratified (green), and basket/chandelier (yellow) interneurons. OLM cells project onto bistratified cells and onto distal dendrites of CA1 pyramidal cells; bistratified interneurons provide inhibition in the basal and proximal apical dendrites; basket and chandelier interneurons target the perisomatic area of pyramidal cells, while receiving additional inputs from CA1 pyramidal cell collaterals and CA3 Schaffer collaterals. The EC provides extrahippocampal theta input (light red box) onto the distal dendrites of CA1 pyramidal cells via the perforant path, as well as excitation onto mossy cells in DG.

The hippocampal micro network receives cholinergic inputs from the MSDB and further inputs from the EC (Amaral and Witter, 1989; Kocsis et al., 1999). Additionally, extrahippocampal theta input via the perforant path from EC (**Figure 6B**) results in rhythmic excitation in CA1 (Kocsis et al., 1999). In contrast, rhythmic inhibition of CA1 pyramidal cells is mediated by excitatory and inhibitory projections of MSDB neurons onto interneurons and pyramidal cells in CA1, evoking cholinergic modulation in interneurons coupled with phasic septal inhibition, respectively (Freund and Antal, 1988). Bistratified cells involved in this rhythmic inhibition circuit receive additional theta inputs from CA3 neurons (Müller and Remy, 2014). OLM and bistratified interneurons get direct input from CA1 pyramidal cells and provide feedforward inhibition, feedback inhibition, and lateral inhibition in CA1 (Müller and Remy, 2014). Moreover, direct phasic stimulation of CA1 cells by MSDB synapses (**Figure 6B**) can increase rhythmicity (Petsche et al., 1962). Theta oscillations are referred to as the “on-line” state of the HC (Buzsaki, 2002). They are crucial for the precise input/output transformation of the HC (Klausberger et al., 2004), involved in the induction of LTP (Hasselmo, 2005), and required for proper formation of spatial maps in the HC (Huxter et al., 2003). Furthermore, this oscillatory activity is responsible for the exchange of information among linked members in the ensemble (Buzsaki, 2002) and involved in the procession of spatial information and memory guided navigation (Hasselmo et al., 2002a; Hasselmo et al., 2002b).

## 1.7. Central hypothesis

The central hypothesis of this study builds up on recent findings by *Fuhrmann and colleagues* from 2015 who revealed that movement can be induced by optogenetic excitation of MS VGluT2$^{+}$ cells in mice. Furthermore they convincingly showed that theta oscillations in the hippocampal CA1 region are locked to the very stimulation frequency used in the MS. These findings prove the strong interconnection between MSDB and HC and indicate a crucial role of the MSDB-HC micro network for movement execution.

I hypothesize that an increase in activity in the MS precedes a corresponding increase of HC theta oscillations under physiological conditions, both correlated to the onset of locomotion. The presence of individual neurons with predictive function would strongly suggest that the MS is an important region mediating the preparation of the hippocampal network for increased sensory integration during movement. I suggest a reliable encoding of movement phases within the neuronal activity of the MS-HC network. Furthermore, I try to give proof for a neuronal representation of individual movement phases within the MS-HC network that can reliably predict upcoming changes in locomotion.

I investigated the physiological activity of the MS-HC network during spontaneous movement. To do so, I combined fiberoptometric imaging of the population activity in the MS, multi-unit recordings in both MS and HC, and recordings of the LFP in the HC during voluntary movement of head-fixed mice on a linear treadmill. In this study, locomotion is addressed as a sequence of initiation, acceleration, deceleration, and termination of motor actions rather than the simplified classification of running and resting. For this, I focused on how the rodent MS-HC network changes its activity during distinct movement phases. The fundamental assumption is that movement related activity in the MS can induce theta oscillations in the HC. Analyzing the locomotor behavior of the animal and correlating the simultaneous activity in the MS-HC network on a fine temporal scale should reveal the temporal relation between neuronal preparation in the MS-HC network and movement before, during, and after physical execution.

# 2. Methods

## 2.1. Transgenic mouse lines

The experiments were performed in adult mice of both sexes of the lines listed in **Table 1**. The animals were group-housed up to a maximum of five animals per cage and kept at 21 °C with 12 hours day and night alternation. Food and water were provided ad libitum. All experiments were in accordance to the *German law for the use of animals*. Experimental procedures were approved by the *Landesamt für Natur, Umwelt und Verbraucherschutz* in North Rhine-Westphalia, Germany, and performed in agreement with the European Committees Council Directive (RL2010/63/EU).

**Table 1:** List of mouse lines used in this study

| Mouse strain | Official nomenclature | Description |
|---|---|---|
| VGluT2-cre | Slc17a6$^{tm2(cre)Lowl}$/J | Expression of a cre recombinase variant under the promotor of the sodium-dependent inorganic phosphate cotransporter member 6. Functional enzyme activity has been shown in excitatory and VGluT2-positive neurons in the septal complex, the hippocampal formation, and other nuclei |
| PV-cre | B6.129P2-Pvalb$^{tm1(cre)Arbr}$/J | Expression of a cre recombinase variant under the promotor for somatic PV. Expression of functional cre has been detected in inhibitory and PV-positive neurons, including interneurons |

## 2.2. Surgical procedures

Prior to all surgical procedures, animals were deeply anesthetized by an intraperitoneal injection of anesthetics containing Ketamine (0.13 mg/g bodyweight) and Xylazine (0.01 mg/g bodyweight). Additionally, buprenorphine (0.05 µg/g bodyweight), carprofen (5 µg/g bodyweight), and cefotaxime (0.2 µg/g bodyweight) were injected. All following surgical steps were only conducted once responses to painful stimuli were abolished. In case of recurring responsiveness following tail/toe pinch an additional dose of Ketamine-Xylazine up to a maximum of 50 % of the initial dose was injected. During anesthesia, the animal was placed on a self-regulating heating mat (Fine Science Tools, Heidelberg, Germany) to maintain the physiological body temperature at 36-37 °C. Additionally, breath rate was monitored as the primary vital parameter. For surgical procedures the head of the animal was positioned in a stereotactic frame with ear bars and nose clamp (MA-6N, Narishige, Tokyo, Japan). Following every surgery, injections of buprenorphine (0.05 µg/g bodyweight) were administered twice a day for three days.

### 2.2.1. Stereotactic injections

Stereotactic injections of virus-based vectors were performed on anesthetized animals as described before. The skin on top of the skull was incised and the periosteum was removed. The tip of the injection cannula (34G cannula Hamilton syringe, World Precision Instruments, Berlin, Germany) was placed onto the *bregma* and moved to the stereotactic coordinates taken from *Frankling & Paxinos* (The Mouse Brain in Stereotaxic Coordinates, Third Edition, Academic Press), listed in **Table 2**. Movement of the syringe was motorized (Luigs&Neumann, Ratingen, Germany) and target areas were approached in a 10 ° medial-lateral angle to circumvent major blood vessels. A small hole was drilled into the skull (Ideal micro drill, World Precision Instruments, Berlin, Germany) above the target region and the injection needle was pushed slowly into the brain until it reached the final position. A total volume of 1 µl virus solution (see **Table 3**) was injected with an UltraMicroPump (World Precision Instruments, Germany) at 0.1 µl/min pump speed followed by 10 minutes pause to enable the virus solution to sink into the surrounding tissue. After the injection, the needle was slowly removed from the tissue. The craniotomy was sealed with an absorbable gelatin sponge (Gelfoam, Pfizer, New York, USA). A

biodegradable sewing thread (Vicryl Plus, Johnson & Johnson Medical GmbH, Norderstedt, Germany) was used to suture the skin.

**Table 2:** Stereotactic coordinates of brain regions targeted in this study

| Target brain region | Stereotactic coordinates relative to bregma | |
|---|---|---|
| Medial septum diagonal band of Broca | + 1000 µm | rostral-caudal |
| | + 750 µm | lateral |
| | - 4400 µm | dorsal-ventral |
| Hippocampal formation (CA1) | - 2300 µm | rostral-caudal |
| | + 2000 µm | lateral |
| | - 1200 µm | dorsal-ventral |

#### 2.2.1.1. Vectors

An adeno-associated virus (AAV) was used as a vector to express proteins in specific brain regions by stereotactic injections. These nonpathogenic human parvoviruses have a limited replication capability and can transduce dividing and non-dividing cells. The vectors contain a single-stranded DNA fragment and are suitable for long-term expressions in the living animal due to little immunogenicity. The vector used is shown in **Table 3**. The virus contained the DNA sequence for a floxed version of the GCaMP5G protein under a synapsin promoter. An additional posttranscriptional regulatory element (WPRE) was added to enhance expression of the protein of interest (**Figure 7**). The virus was commercially available and purchased from *Penn Vector Core* (Penn Vector Core, Philadelphia, USA).

**Table 3**: Viral vector used in this study

| Plasmid | Type | Promotor | Fusion protein | Titer | Manufacturer |
|---|---|---|---|---|---|
| hSyn.Flex.GCaMP5G (GCaMP3-T302L.R303P.D380Y).WPRE.SV40 | AAV2 | hSynapsin | GFP | $2.49e^{13}$ | Penn Vector Core |

### 2.2.1.2. Cre-loxP system

In order to monitor and manipulate specific neuronal subpopulations in the target areas, viral vectors containing the necessary constructs were introduced into the brain areas. Cell-type specific transduction was achieved by cre-regulated gene expression (**Figure 7**).

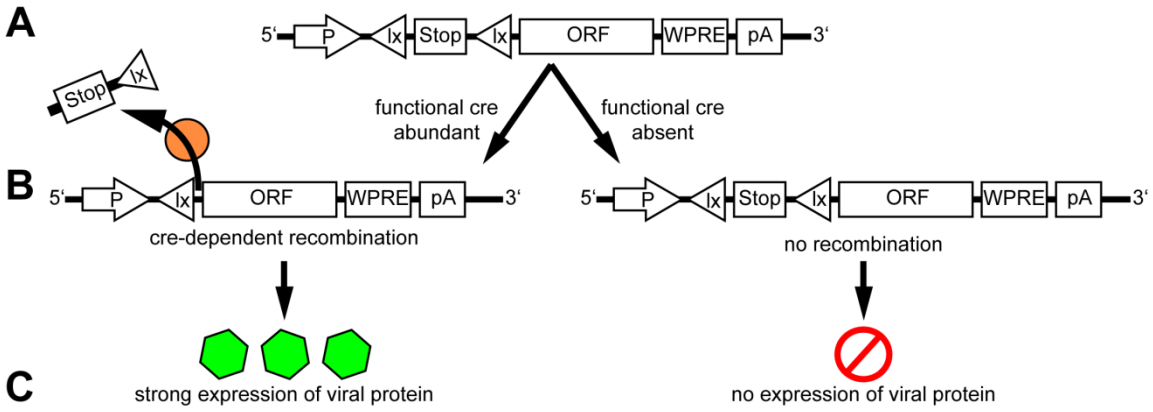


**Figure 7:** Illustration of cre-dependent expression of virally transferred constructs in neurons

**A** Single-stranded DNA including a promotor (P), a stop codon (Stop) flanked by loxP sites (lx), an open reading frame containing the genome for the desired protein (ORF), a post-regulatory element (WPRE, woodchuck hepatitis posttranscriptional regulatory element; increases expression by a magnitude), and a poly-A cassette (pA). **B** Cells with active cre recombine the viral DNA and excise the stop codon between the loxP sites. **C** Cre-positive cell start expressing the protein encoded in the ORF while cells without active cre are not able to recombine and do not express the introduced protein.

The viral construct required a special design for this purpose. For this, loxP sites were positioned on either side of a stop codon preceding the gene of interest (*here* GCaMP) that repressed expression in the absence of the cre-recombinase protein. In cells that contained functional cre the stop codon was excised and the gene was translated during protein biosynthesis.

### 2.2.2. Chronic implantations

For optical monitoring of changes in GCaMP5G fluorescence mono fiber-optic cannulas (**Figure 8A**) were implanted into the brain of anaesthetized animals.

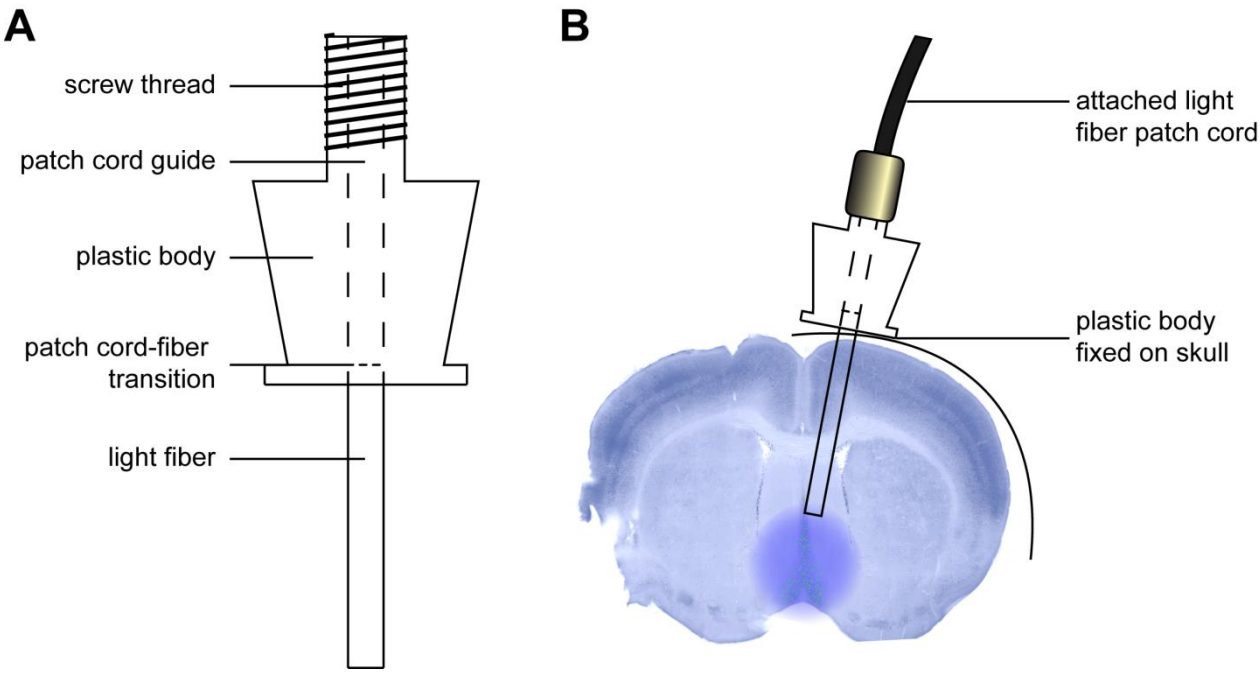


**Figure 8:** Principle of a mono fiber-optic cannula

**A** Mechanical composition of a mono fiber-optic cannula. **B** Scheme of an implanted mono fiber-optic cannula at a 10° angle attached to the skull; light fiber patch cord inserted into patch cord guide canal. Blue halo indicates spread of excitation light for fluorometric recordings from the tip of the light fiber.

After sedation the scalp and the periosteum were removed and the surface of the cranial bone was etched with phosphoric acid (Phosphoric Acid Gel Etchant 37.5 %, Kerr Italia, Italy). Coating the skull with a volatile primer solution (OptiBond FL Prime, Kerr Italia, Italy) followed by an adhesive substance (OptiBond FL Adhesive, Kerr Italia, Italy) created a solid basis for implants. Afterwards, a craniotomy was performed above the MSDB and a mono fiber-optic cannula (MFC_400/430-0.37_5mm_SM3(P)_FLT, Doric Lenses, Quebec, Canada; **Figure 8A**) was inserted into the tissue in a 10 ° angle and pushed to its final position in the immediate vicinity to the MS (**Figure 8B**). For local field potential recordings monopolar tungsten electrodes (W558511, Advent Research Materials, Oxford, England) were implanted in the CA1. Implants were permanently attached to the head with a light-curable flowable composite (Gradia Direct Flo, GC Corporation, Japan).

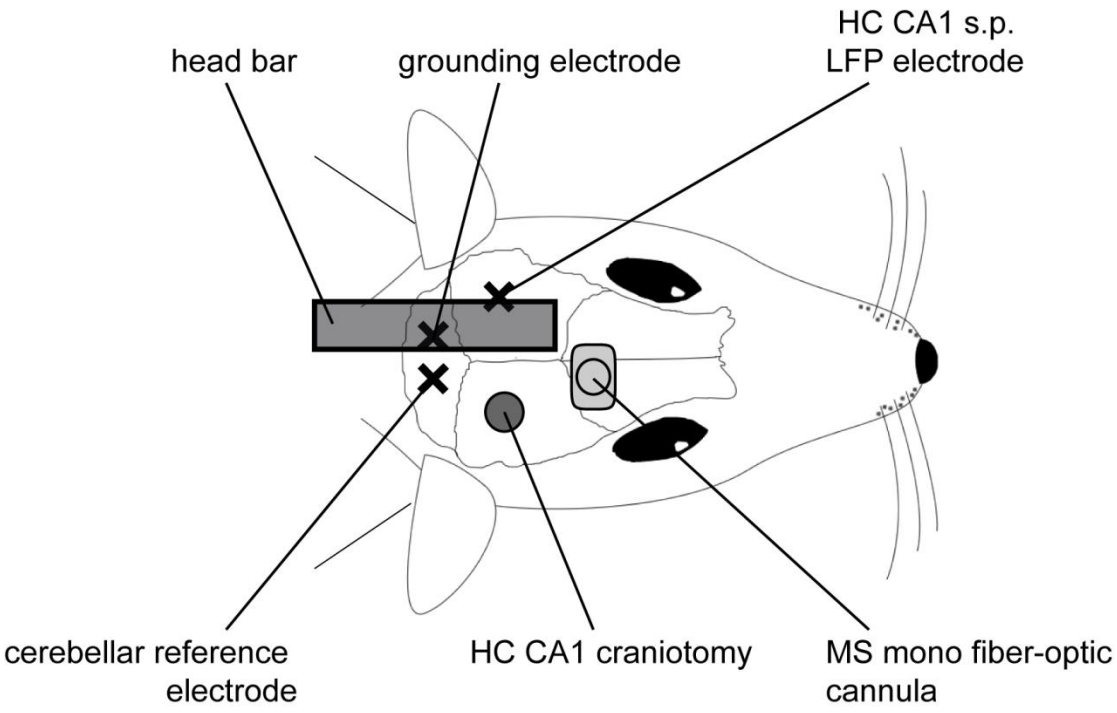


**Figure 9:** Scheme illustrating locations of chronic implants

A local field potential electrode was implanted into the left hippocampal CA1 stratum pyramidale; a grounding electrode was implanted above the cerebellum; a reference electrode was implanted into the cerebellum; a craniotomy was performed above hippocampus CA1 or the MS and sealed with a removable silicone plug; the fiber-optic hybrid cannula was implanted proximate to the medial septum.

For experiments involving tetrode recordings in either MSDB or hippocampal CA1, smaller craniotomies were performed similarly on the opposite hemisphere. These craniotomies were immediately covered by silicon. For head-fixation during the experiment a metal-bar (Luigs&Neumann, Ratingen, Germany) was positioned on the skull (**Figure 9**). The positions of the implanted fibers were checked post-mortem in the sliced tissue using a confocal laser microscope (LSM700, Zeiss, Germany). Animals with badly positioned implants were excluded from the analysis.

## 2.3. Data acquisition and software

All acquired data was recorded at 10 kHz sampling rate and down sampled for the offline analysis to 1 kHz. The higher sampling rate was necessary for proper detection of unit activity in tetrode recordings.

### 2.3.1. Habituation

The animals used in *in vivo* experiments were habituated to both the experimenter and the setup for at least one week prior to the first recording session. Habituation to the experimenter included physical contact and head restraining.

### 2.3.2. Fiberoptometry

Fluorometric recordings of fluorescence signals were performed using an implanted glass fiber (see 2.2.2) connected to a light fiber patch cord transporting blue light-evoked fluorescence to a photon multiplier tube (PMT). The signal was pre-amplified and analog-digital converted by an ITC 18 board (NPI, Germany).

### 2.3.3. Local field potential recordings

Electrical local population activity in the HCF was measured via implanted tungsten wire electrodes in CA1 s.p. During the recording the electrodes were connected to an EXT-02F extracellular amplifier (NPI, Germany). Electrical signals were filtered with a 3 Hz high pass and a 500 Hz low pass filter and amplitudes were amplified 500-fold. Data were

recorded with an ITC-18 board (NPI, Germany), operated with the Igor Pro software (Wavemetrics, Oregon, USA).

### 2.3.4. Multi-unit recordings

The electrical activity of multiple cells (“units”) was monitored by placing tetrodes (probe with an array of four electrodes) or heptodes (probe with an array of seven electrodes) in the brain region of interest. The animals that had been prepared for these experiments had received a craniotomy that had been covered with a silicone plug (**Figure 9**). The plug was removed for the course of the experiment and placed back afterwards. The tetrode was stereotactically placed into the brain through the opening in the skull until it reached the outer borders of the MS (3500 µm ventral in 10 ° angle from brain surface) or the HCF (1100 µm ventral in 10 ° angle from brain surface). The tetrode was then lowered deeper into the tissue until AP like unit activity was detected using a digital oscilloscope (Rigol, Beaverton, USA). The electrophysiological data were analog-digital converted with an EXT-16DX board (NPI, Germany) and acquired with the Igor Pro software.

#### 2.3.4.1. Transcardial perfusion fixation

After completion of the in-vivo experiments the brain tissue of each animal was extracted from the skull and positioning of electrodes and cannulas was checked. For this, the animal was anesthetized with a lethal dose and the thorax was opened. After opening of the pericardium, the left ventricle was pierced with an injection needle for perfusion. The right atrium was incised and a peristaltic pump (PeriStar Pro, World Precision Instruments, Germany) was used to perfuse PBS (Sigma Aldrich, Germany) in 5 ml/min. As soon as the leaking perfusion solution was free of blood the perfusion solution was switched to 4 % PFA (Roti-Histofix, Carl Roth, Germany). The perfusion was performed for 15 minutes. Afterwards, the head was detached and the brain was removed from the skull. The tissue was either stored in 4 % PFA for 1 hour at room temperature or overnight at 4 °C to improve fixation efficiency before being transferred into PBS for permanent storage.

#### 2.3.4.2. Confocal slice microscopy

For microscopic imaging the brain tissue was sliced with a Leica VT-1200S vibratome (Leica Microsystems, Wetzlar, Germany) into 100 µm thick sections. The slices were mounted with Aqua-Poly/Mount (1806-20, Polysciences, Inc.) and stored at 4 °C. High-resolution images were obtained with a confocal laser microscope (LSM700, Zeiss, Germany) using a 20x objective (PlanApochromat 20x/0.8, Zeiss, Germany).

## 2.4. Data analysis

### 2.4.1. Analysis of locomotion

Movement of the animal was tracked by the position readout of a custom-designed virtual reality setup recording the rotation of one rotating wheel of a linear treadmill. The virtual position of the animal was computed offline in MATLAB 2013b (MathWorks, Natick, USA) and locomotion speed could be calculated. The digital position signal was noise-compensated with a Kalman filter.

$$V = f'(Position)$$

$$V = \lim_{x_1 \to x_0} \frac{f(x_1) - f(x_0)}{x_1 - x_0}$$

$$V = \lim_{\Delta x \to 0} \frac{\Delta y}{\Delta x}$$

Immobility or resting was defined as every time point with a velocity slower than 0.1 cm/s and running as every velocity faster than 2 cm/s.

Detailed analysis of movement phases was performed by defining four distinct phases during locomotion: (1) Initiation of movement, (2) end of acceleration, (3) start of deceleration, and (4) termination of movement. By defining criteria, alignment points for the four movement phases (**Figure 10**) could be detected in the velocity traces of each recording (**Table 4**).

**Table 4:** Functional definition of movement phases

| Phase | Previous interval | Point of alignment | Following interval |
|---|---|---|---|
| **Initiation (onset)** | 0.1 cm/s > \|v\| for t ≥ 2 s | **v>0.1 cm/s** | v > 0.1 cm/s for t ≥ 1 s |
| **End of acceleration (acc)** | Detected onset → v > 0.1 cm/s for t ≥ 1 s | **v'=0** | v > 0.1 cm/s for t ≥ 1 s |
| **Start of deceleration (dec)** | v > 0.1 cm/s for t ≥ 1 s | **v'=0** | v > 0.1 cm/s for t ≥ 1 s → detected offset |
| **Termination (offset)** | \|v\| > 0.1 cm/s for t ≥ 1 s | **v=0 cm/s** | 0.1 cm/s > v for t ≥ 2 s |

In detail, the different phases are defined as:

**(1)** ***Initiation (onset):***

The absolute velocity is required to be slower than 0.1 cm/s for at least 2 s before crossing the threshold of 0.1 cm/s (putative onset point); if the velocity is faster than 0.1 cm/s for at least 1 s the initial threshold crossing is defined as an onset point.

**(2)** ***End of acceleration (acc):***

After a detected onset, the velocity is required to be faster than 1 cm/s for at least 1 s before the first derivative of the trace (v') is checked to be equal to 0 (putative acc

point); if the velocity stays faster than 0.1 cm/s for at least 1 s, the point with v'=0 is defined as an end of acceleration point.

**(3)** ***Start of deceleration (dec)***

The velocity is required to be at least 1 s faster than 0.1 cm/s backwards from a previously defined offset point (see 4) before the first derivative of the velocity trace (v') is checked to equal 0 (putative dec point); if the velocity is larger than 0.1 cm/s for at least 1 s prior to this, the point is defined as a start of deceleration point.

**(4)** ***Termination (offset)***

The absolute velocity is required to be faster than 0.1 cm/s for at least 1 s before crossing the 0.1 cm/s threshold (putative offset point); if the velocity is slower than 0.1 cm/s for at least 2 s the threshold crossing is defined as an offset point.

These intervals were automatically detected by the individual characteristics of each phase with custom-mage MATLAB 2013b scripts, as illustrated in **Figure 10**.

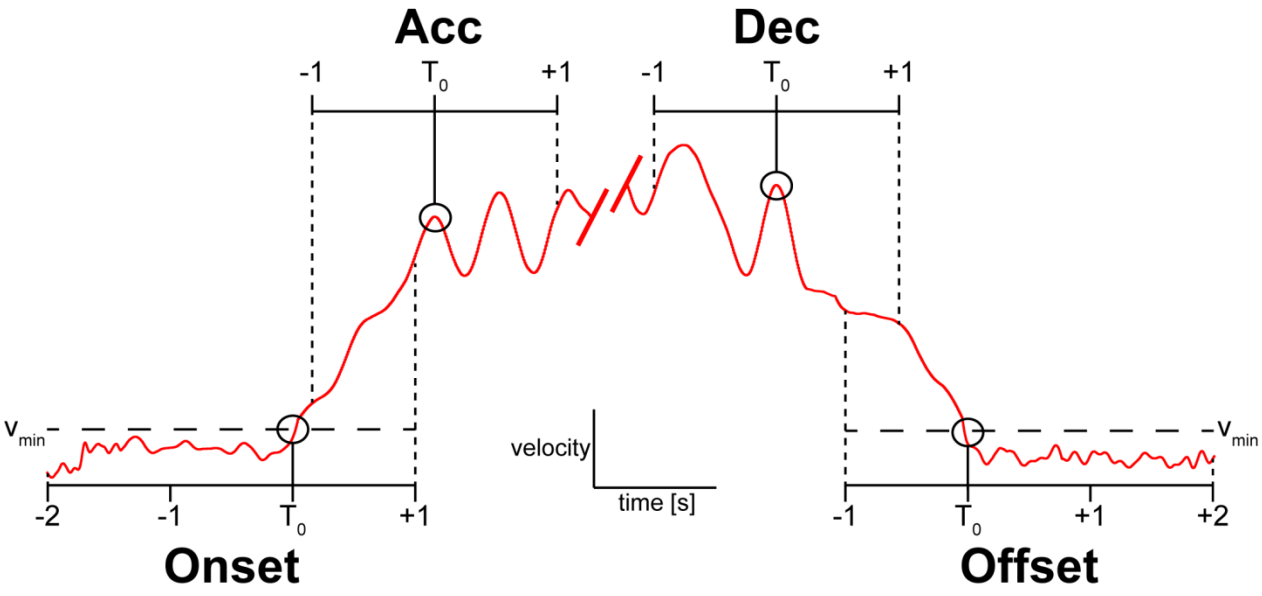


**Figure 10:** Illustration of distinct states during a movement phase and functional criteria

Schematic illustration of movement phase detection. The alignment points (circles close to $T_0$) are identified time points that fulfill all respective criteria during any movement.

### 2.4.2. Alignment and slope analysis

In the next step of the analysis the data of the fluoremetric recording, the LFP recording, and the multi-unit recording were aligned to the movement intervals as described before. Furthermore, dependencies and correlations between the parameters and the locomotion were analyzed using these short intervals. To investigate whether a parameter would predict the upcoming change in locomotion at the alignment, the slope of the linearly fitted data in the interval 400 ms prior to the alignment point was extracted for every alignment and statistically tested against zero (**Figure 11A**). In case of an onset of locomotion, a significant slope indicated that the parameter predicted the future movement behavior (**Figure 11B**).

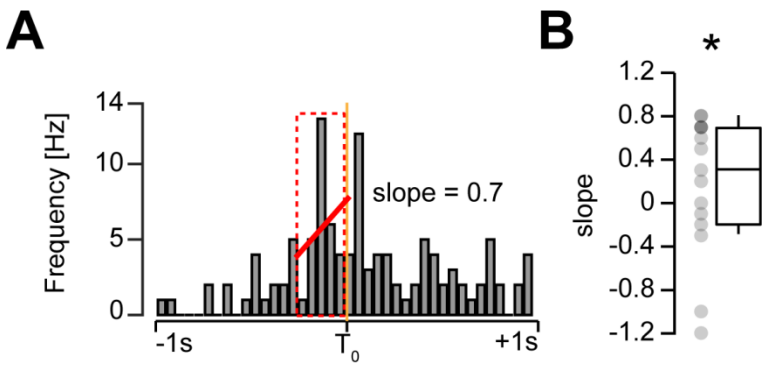


**Figure 11:** Exemplary slope analysis of a parameter prior to an alignment point

**A** Exemplary firing pattern of a single MS unit during an onset phase (onset point at $T_0$). The data in the 400 ms interval prior to the alignment point (dashed line) was linearly fitted (red line) and the slope value was extracted. **B** The slopes of the linear fit for each alignment were tested against zero. Significant slopes indicated that the unit/parameter tested could predict the upcoming initiation of locomotion.

### 2.4.3. Analysis of electrophysiological recordings

#### 2.4.3.1. Analysis of local field potential recordings

The spectral analysis of LFP data was performed using the Morlet-Wavelet transformation in Matlab 2013b. Spectrograms were generated with a resolution of ΔFreq=0.1 Hz and Δt=0.001 s and used for all calculations and correlations. The theta peak frequency was identified as the predominant frequency between 4 Hz up to 12 Hz while the theta power was the averaged amplitude of all frequencies in this theta range. Theta frequency bands were defined as 1 Hz integer bins covering the theta frequency range.

Theta phases were described as a sinus wave (**Figure 12A**) with sin(0 °) to sin(90 °) representing the rising phase, sin(90 °) to sin(270 °) describing the decaying phase, and sin(270 °) to sin(360 °) describing the following rising phase of the oscillation recorded in the hippocampal CA1 region (**Figure 12B**).

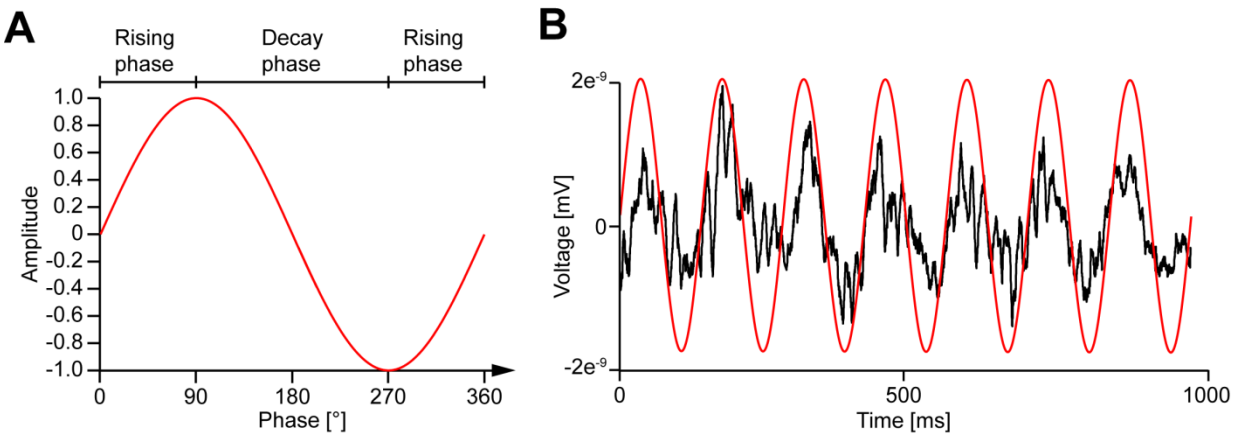


**Figure 12:** Mathematical description of oscillations in local field potential recordings

**A** Sinus wave indicating activation phases for increases in voltage (rising phase) or decreases in recorded voltage (decay phase). **B** Overlay of a mathematical sinus wave (red) and recorded 7-8 Hz local field oscillation (black).

#### 2.4.3.2. Analysis of multi-unit recordings

Multi-unit recordings were processed using the KlustaKwik software (Kenneth Harris, UCL). Automatically detected spike events were compared regarding their spike timing on the four electrodes of the tetrode. Spike waveforms were manually compared to all other waveforms of a recording session and similar waveforms were clustered as one *unit*. The spiking time points of combined units were combined and saved. Afterwards, spiking frequencies were calculated for every unit by counting events per 50 ms and these time bins were displayed in [Hz]. Only recordings with a minimum of 10 s running duration and a peak velocity faster than 5 cm/s were further processed. Units with an average firing rate of less than 0.5 Hz during periods of running were discarded to prevent imprecise conclusions due to insufficient firing frequencies.

### 2.4.4. Analysis fiberoptometric recordings

The fluorometric recordings of neuronal population activity using the GCaMP5G signal were corrected for bleaching and noise artefacts by subtracting 120 s average moving boxes from the original raw data. The average fluorescence of the raw signal was added afterwards to maintain relation between transients and baseline fluorescence. The change in fluorescence is presented as

$$\frac{\Delta F}{F}$$

or

$$\frac{recorded\ fluorescence}{baseline\ fluorescence}$$

with the average fluorescence intensity as baseline fluorescence. Individual fluorescence traces were smoothed by 50 ms intervals for display.

### 2.4.5. Modulation analysis

In order to analyze speed modulation of any of the parameters recorded, the velocity trace was binned into 1 cm/s velocity bins. For every bin faster than 2 cm/s, each parameter was averaged correspondingly and the overall average for each velocity bin was calculated. The averages per velocity bin were linearly fitted and weighted by the spare root of its duration. The continuous GCaMP5G and LFP data were considered as significantly speed-modulated if the slope of the linear fit was significantly different from zero among the animals recorded, tested with the one-sample Wilcoxon sign-rank test. Single-units were considered as positively speed-modulated if the 2.5 % confidence interval of the linear fit was positive or rather as negatively speed-modulated if the 97.5 % confidence interval of the slope was negative. Possible theta modulation of single-units was estimated by calculating the fast Fourier transform of the -500 ms to +500 ms interval of the autocorrelation for each unit. The amplitude was smoothed with a rectangular filter over ±1 Hz and the theta modulation index (TMI) was defined as the ratio of the squared amplitude in the 6-11 Hz and the 2-50 Hz bands. Significance of the TMI was tested by shifting the AP time points for every unit randomly between -10 s and +10 s. This procedure was repeated 1000 times. Every iteration generated an artificial TMI. The p-value of the real data was defined as the ratio of artificial modulation indexes larger than the original to the number of iterations.

Phase modulation of recorded units was calculated by estimating the respective theta phase for every AP time point, binned into 72 phase bins of 5° each (see chapter 2.4.3.1). The APs were counted for each bin. The preferred theta phase was detected as the phase bin containing the highest count of APs. The phase modulation index (PMI) was defined as the ratio between counts at the preferred phase minus the count at the phase with the lowest count divided by the sum of both counts.

$$\mathrm{PMI} = \frac{\mathrm{Count}_{\max} - \mathrm{Count}_{\min}}{\mathrm{Count}_{\max} + \mathrm{Count}_{\min}}$$

The significance of each PMI was calculated similar to the TMI by artificially time shifting every AP time point and repeating this procedure 1000 times. The ratio of artificial PMIs larger than the original PMI to the number of iterations was defined as the p-value. This approach is referred to as bootstrapping.

### 2.4.6. Time shift analysis

To analyze a movement-predictive character of LFP oscillations and unit firing, a time shift analysis was performed. The parameters were time shifted by +1 s in +50 ms steps and by -1 s in -50 ms steps respectively. After each step the time shifted parameter was correlated to the binned velocity trace (1 cm/s bins). After performing a linear fit of the time shifted correlation, the resulting slope was compared to the slope of the original data and taken as an indicator for the overlap of the parameter and the velocity trace. An increased slope indicated a higher degree of overlap; a decreased slope represented less overlap. For each time shift analysis, the "best overlap" was defined as the time shift step resulting in the largest slope and the corresponding "time shift" (**Figure 13**).

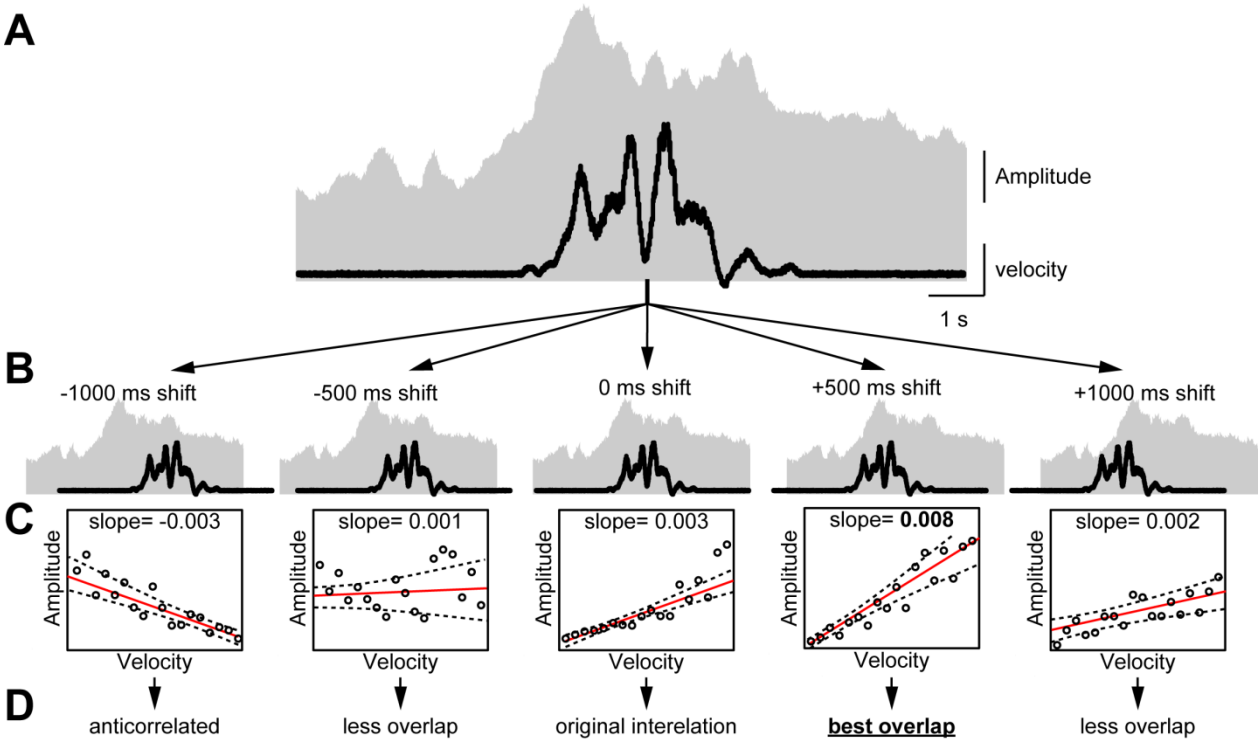


**Figure 13:** Illustration of a time shift analysis for a parameter against the corresponding velocity

**A** The original recording of an exemplary parameter (grey) and the corresponding velocity trace (black) are shown. **B** The parameter of interest is shifted in 50 ms steps by -1000 ms to +1000 ms. **C** Every shifted data is plotted against the underlying velocity and linearly fitted (red line). **D** The best overlap is determined depending on the resulting slope of the linear fit; in this example, the +500 ms shift yielded the largest positive slope and is referred to as the best fit.

To statistically validate the best overlap, the bootstrapping method was used on the recorded data. For this, all data points of the parameter traces were randomly shifted by -10 s to +10 s and the resulting traces were used in a time shift analysis. The best overlap of the shuffled data was compared to the best overlap of the real data. The best overlap of the real data was considered to be significant if this overlap was larger than the largest slope of the bootstrapped data in at least 975 out of 1000 iterations.

### 2.4.7. Statistical analysis

Statistical analysis of the data was done using SPSS Statistics 21 software (IBM). All data was first checked for Gaussian distribution with a Kolmogorov-Smirnov test. Normally distributed data was tested for significant differences with the paired or unpaired two-tailed Student's t-test. Heterogeneously distributed related and independent samples were tested with a non-parametric related-samples Wilcoxon signed rank test and Mann-Whitney U test, respectively. Slopes of fits without corresponding baseline data were tested for significant increase or decrease with the Wilcoxon rank-sum test. The significance levels were defined as $p<0.05$ = *, $p<0.01$ = **, $p<0.001$ = ***, and $p<0.0001$=****.

# 3. Results

## 3.1. In-vivo cell-type specific population activity in the MS

Activity analysis of neuronal populations in the MS was achieved by deep brain epifluorescence imaging via chronically implanted light fibers. To target genetically distinct groups of neurons, cre-expressing cells of mice were transduced with AAVs carrying a floxed version of GCaMP5G. The emitted fluorescence was detected by a fiberoptometer. The habituated animal was head-fixed on a linear treadmill under standardized conditions. Perception of external stimuli, acoustical or visual, was minimized to prevent irritations. Optical monitoring of changes in fluorescence intensity in the MS, electrophysiological recordings of local field potentials in the HC, and recording of the velocity of the animal were performed simultaneously. High sampling frequencies were used for high temporal resolution in the detection of onset, changes, and termination of locomotor behavior.

### 3.1.1. Locomotion associated activation of VGluT2$^+$ neurons in the MS

Population activity of glutamatergic cells in the MS was measured via an implanted light fiber in VGluT2-cre mice expressing a floxed version of GCaMP5G (**Figure 14A**). The tip of the light fiber terminated close to the MSDB region and detected the summed fluorescence of cells expressing the $Ca^{2+}$ indicator protein GCaMP5G. Increasing $Ca^{2+}$ dependent fluorescence signals were reliably recorded for subsequent running intervals (**Figure 14C**) with changes in fluorescence ranging from ~1-10 % ΔF/F. This locomotion associated 2-fold increase (n=6, $\mu_{rest}$=1.78 ± 0.23 [%], $\mu_{run}$=3.47 ± 0.54 [%], p=0.005) was observed in multiple recording sessions and animals (**Figure 14B**). Increases in $Ca^{2+}$ signaling as a proxy for neuronal AP firing confirmed an elevated activity level in the MS during movement.

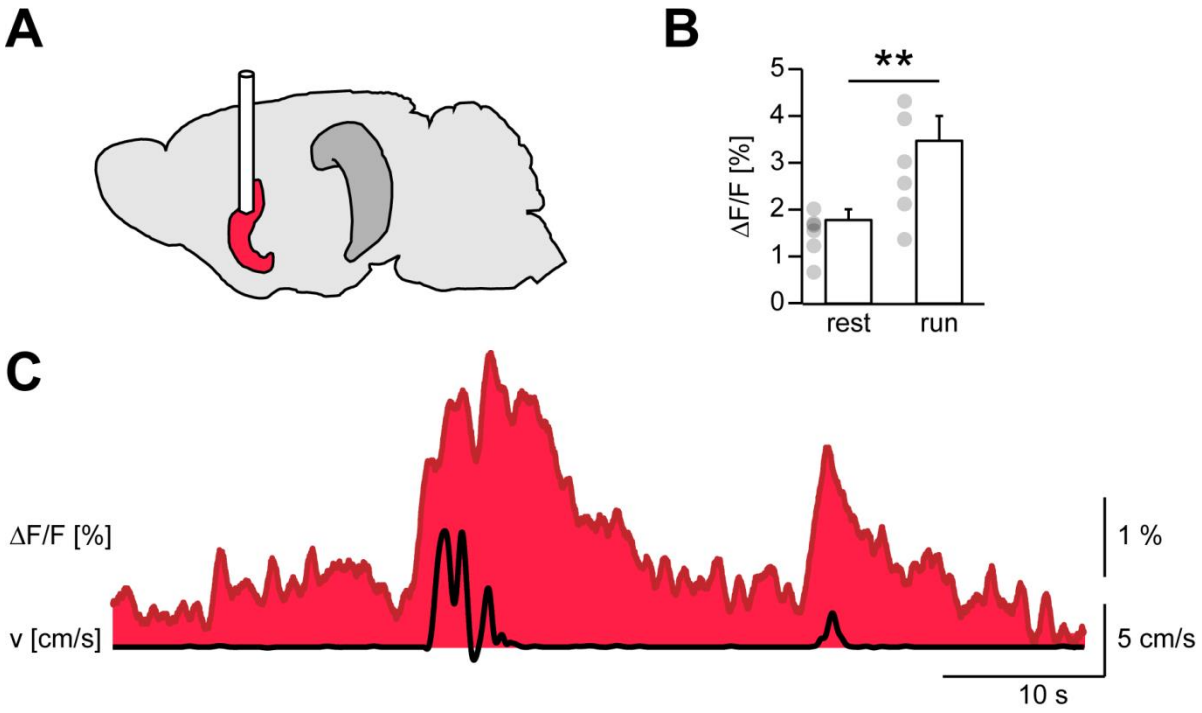


**Figure 14:** VGluT2-GCaMP5G transients increase during locomotion

**A** Schematic illustration of MS expressing GCaMP5G with adjacent light fiber. **B** Comparison of averaged GCaMP5G ΔF/F in VGluT2$^+$ MS neurons during resting intervals and running intervals; single animal data depicted as circles. **C** Exemplary MS GCaMP5G transients (red) and corresponding velocity trace (black).

### 3.1.2. Velocity-correlated increases in VGluT2$^+$ population activity

The locomotion associated changes of the MS VGluT2-GCaMP5G signals were further investigated regarding specific kinetics during distinct velocities. While the head-fixed animal moved on the linear treadmill at varying speeds (**Figure 15A**), binned velocities exceeding the threshold for running detection at 2 cm/s were correlated to the corresponding ΔF/F (**Figure 15B**). Weighted fitting of the data (**Figure 15B**; red line) was used as a measure to describe the linear relation between velocity and fluorescence in MS VGluT2$^+$ neurons revealing a positive interrelation (**Figure 15C**; n=6, μ=0.19 ± 0.06 [slope], p=0.046). Due to individual behavior of each animal and differing maximum velocity this finding was blurred in some recordings, most probably caused by low top speeds during a recording session (**Figure 15D**). Yet, this positive speed modulation of GCaMP5G fluorescence was detected in 5 of 6 animals underlining its physiological relevance.

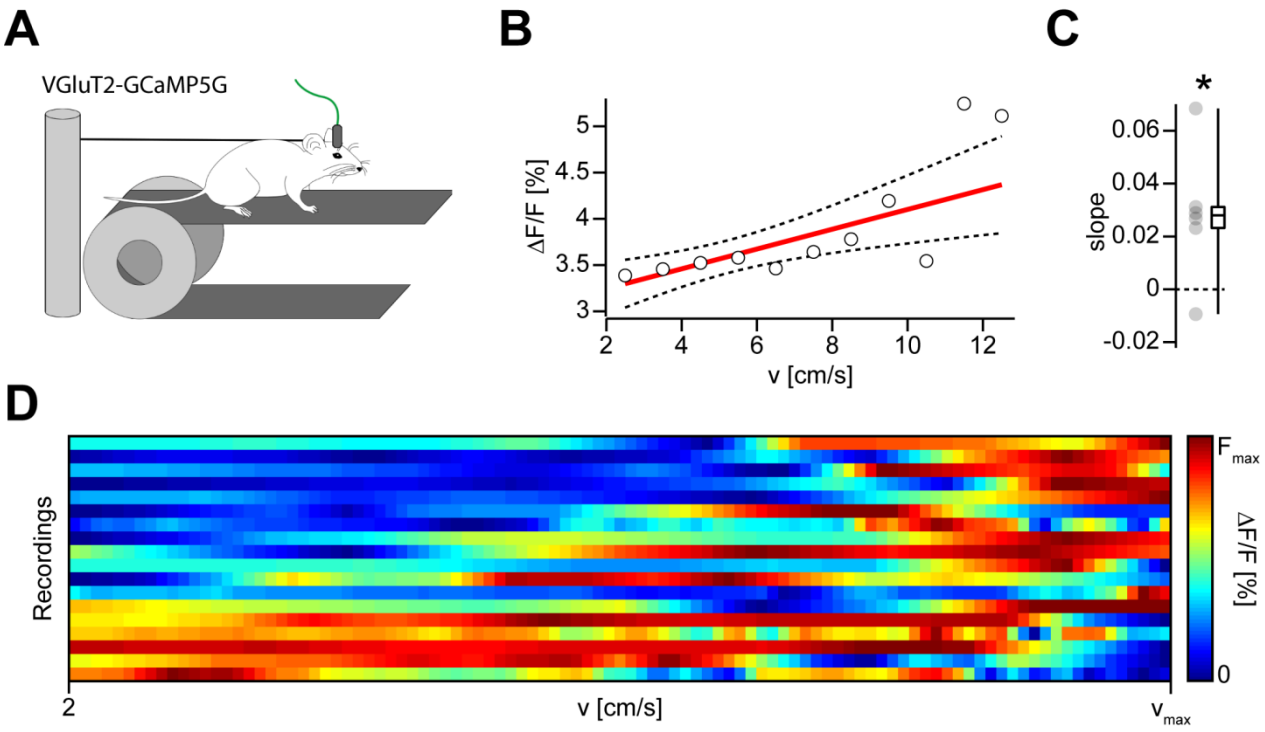


**Figure 15:** VGluT2-GCaMP5G fluorescence is positively correlated to the velocity of locomotion

**A** Illustration of a head fixed VGluT2-GCaMP5G animal on a linear treadmill with the light fiber patch cord. **B** Exemplary interrelation of binned velocity to changes in fluorescence intensity (circles), a weighted linear fit of the data (red), and the respective confidence interval of the fit (dashed line). **C** Median slope of fits of 6 recorded animals; single animal data depicted as circles. **D** Interrelation of normalized velocity to changes in normalized fluorescence intensity shown for all recorded data.

### 3.1.3. Movement-state related VGluT2$^+$ activity occurs prior to onset and deceleration phases

High temporal resolution of locomotion enabled a detailed analysis of distinct phases during movement. Onset detection, as well as determining the endpoint of the first acceleration phase, the start of the final deceleration, followed by the absolute termination of locomotion was used to relate specific $Ca^{2+}$ dependent fluorescence changes in VGluT2-GCaMP5G animals to each velocity state. By reproducibly aligning these phases, general kinetics underlying the change in speed along with adaptions occurring prior to the respective phase (**Figure 16**) could be revealed using the slope analysis (see chapter 2.4.2).

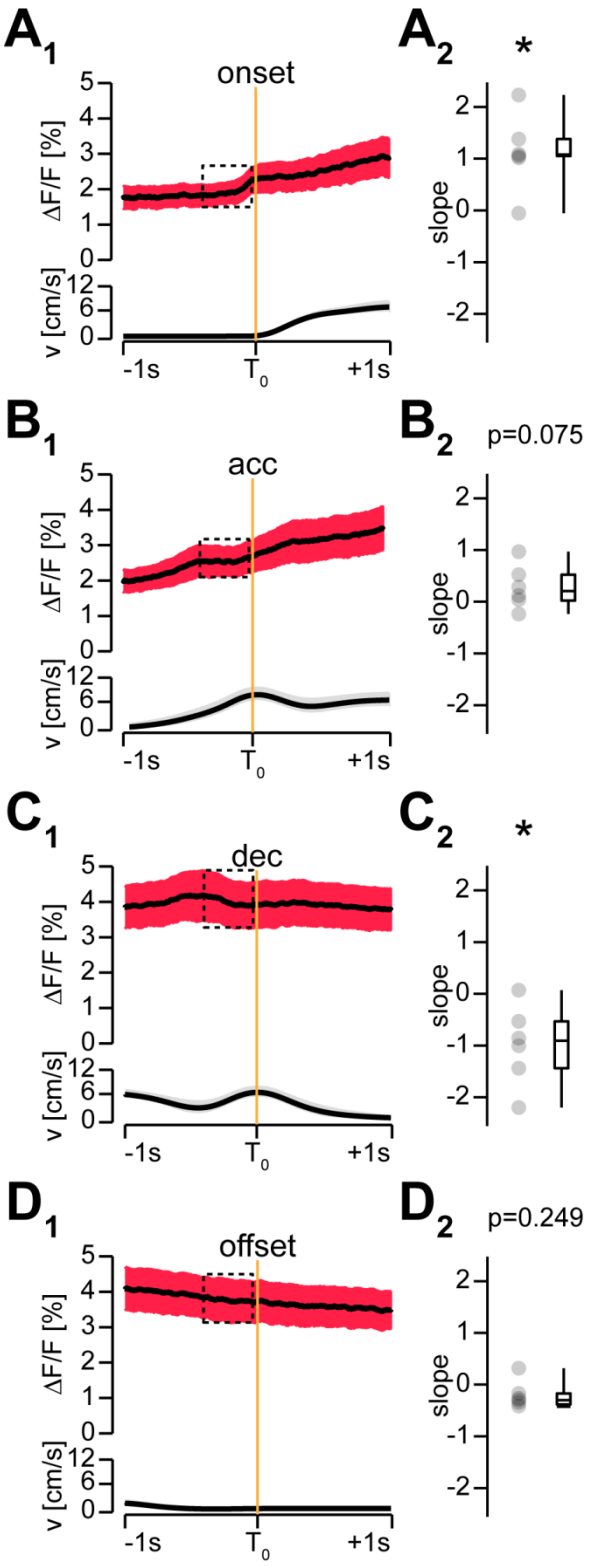


**Figure 16:** Movement related VGluT2-GCaMP5G transients display state specific changes during onset and deceleration

**$A_1$** Top: changes in GCaMP5G intensity (MEAN shown in black; SEM shown in red) aligned to the *onset* of locomotion ($T_0$, orange line) and the corresponding velocity trace (bottom; MEAN shown in black; SEM shown in red). **$A_2$** Median of slopes of the interval indicated by the dashed box on GCaMP5G traces; single animal data depicted as circles. **$B_1$**, **$B_2$** like $A_1$ and $A_2$ with alignment point *end of acceleration* (acc), **$C_1$**, **$C_2$** like $A_1$ and $A_2$ with alignment point *start of deceleration* (dec), and **$D_1$**, **$D_2$** like $A_1$ and $A_2$ with alignment point *offset* of locomotion (offset).

Detailed investigation of the onset phase (**Figure 16A$_1$**) revealed an increase of VGluT2-GCaMP5G fluorescence prior to the alignment point (**Figure 16A$_2$**; n=6, μ=1.12 ± 0.30 [%], p=0.046) followed by an ongoing increase of ΔF/F. The early increase was detected in an interval 400 ms before locomotion started although the exact time point could not be estimated. The succeeding acceleration phase was aligned to the first velocity peak after 1 s continuous acceleration (**Figure 16B$_1$**). The mean ΔF/F in this interval characteristically displayed leveling kinetics despite the still increasing velocity (**Figure 16B$_2$**; n=6, μ=0.28 ± 0.17 [%], p=0.075), is not in agreement with a strictly linear correlation of fluorescence and velocity (**Figure 15C**). Phases in which the animal slowed were investigated around the start of deceleration (**Figure 16C$_1$**). This interval was characterized by the last detectable velocity peak followed by decreasing speeds and a certain termination of locomotion (**Figure 16D$_1$**). The corresponding GCaMP5G signal of VGluT2$^+$ neurons showed a significantly negative slope of the linear fit in the 400 ms interval prior to the alignment point $T_0$ (**Figure 16C$_2$**; dec; n=6, μ=-0.99 ± 0.32 [%], p=0.046). The mean ΔF/F during detected offsets of movement displayed a slope indifferent to zero in the immediate 400 ms interval before total halt (**Figure 16D$_2$**; n=6, μ=-0.20 ± 0.11 [%], p=0.249). The kinetics of the GCaMP5G-protein appeared to be rather slow after a completed movement period. The minimum time needed to reduce fluorescence back to baseline level was not estimated here but clearly exceeded 2 s (**Figure 16D$_2$**, visible after offset). These slow decay kinetics of $Ca^{2+}$ indicators have been previously described (Akerboom et al., 2012) and prevent the precise definition of the time point of locomotion offset.

### 3.2. Increased activity in MS PV neurons during episodes of movement

In another set of experiments the change in GCaMP5G fluorescence was recorded from GABAergic PV$^+$ neurons in the MS (**Figure 17A**). Albeit small in peak intensity, ΔF/F was increased during running periods (**Figure 17C**). Similar to the findings in VGluT2-GCaMP5G animals (**Figure 14**), quantification and statistical evaluation of resting versus running intervals revealed a significant increase during locomotion (**Figure 17B**; n=8, $\mu_{rest}$=0.75 ± 0.12 [%], $\mu_{run}$=1.05 ± 0.22 [%], p=0.029). Positioning of the light fiber in PV-GCaMP5G animals was comparable to VGluT2-GCaMP5G animals, yet the majority of

PV neurons tended to be located in the medial part of the MS resulting in lower net fluorescence intensity (see **Figure 3**).

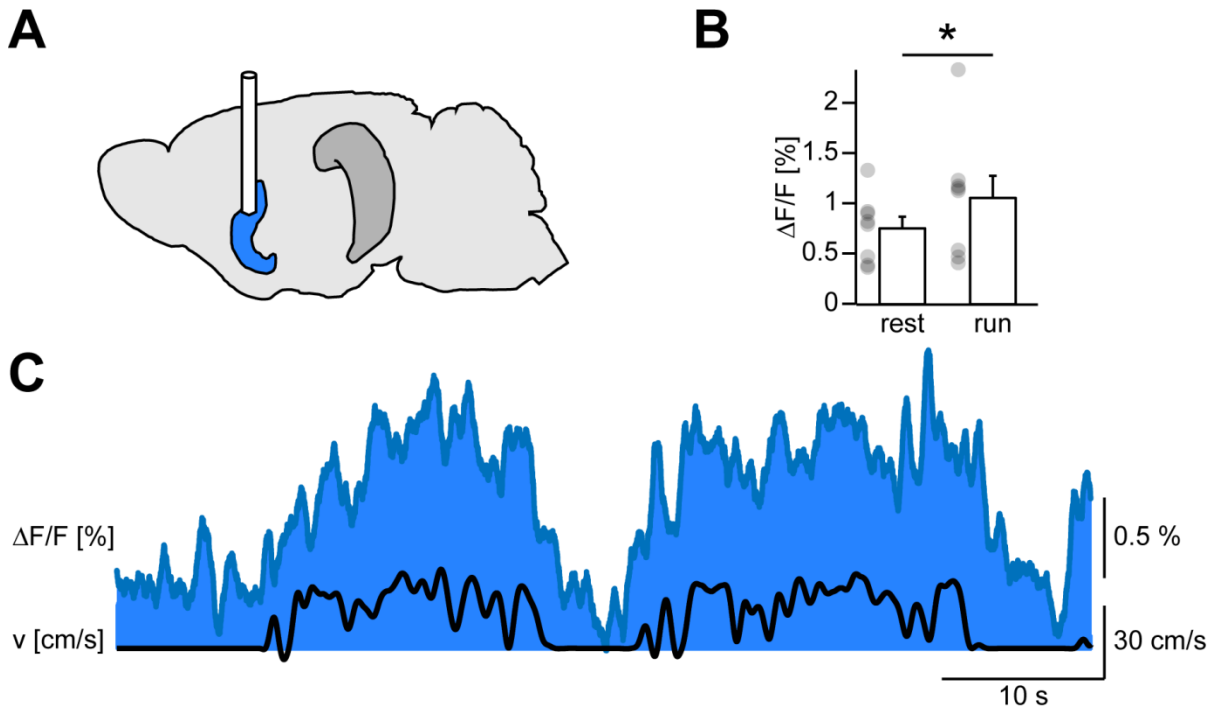


**Figure 17:** PV-GCaMP5G fluorescence increases during locomotion

**A** Schematic illustration of GCaMP5G expressing MS with adjacent light fiber. **B** Comparison of averaged GCaMP5G ΔF/F in $PV^+$ MS neurons during resting intervals and running intervals; single animal data depicted as circles. **C** Exemplary MS GCaMP5G transients (blue) and corresponding velocity trace (black).

### 3.2.1. Changes in $PV^+$ population activity correlated to the speed

$Ca^{2+}$ transients of PV-GCaMP5G animals performing voluntary movement while being head-fixed on a linear treadmill (**Figure 18A**) were correlated to binned velocity faster than 2 cm/s. Averaged bins (**Figure 18B**; circles) were weighted and linearly fitting (red line). The averaged slopes were averaged over every animal and used as measure to evaluate the fluorescence versus velocity interrelation. Statistical analysis of the slopes of the linear fits detected a positive correlation to the velocity (**Figure 18C**; n=8, $\mu=2.25*10^{-3}$ [slope], p=0.017). This phenomenon was found in the global approach but was consistently detected in the majority of individual recording sessions, as well (**Figure 18D**).

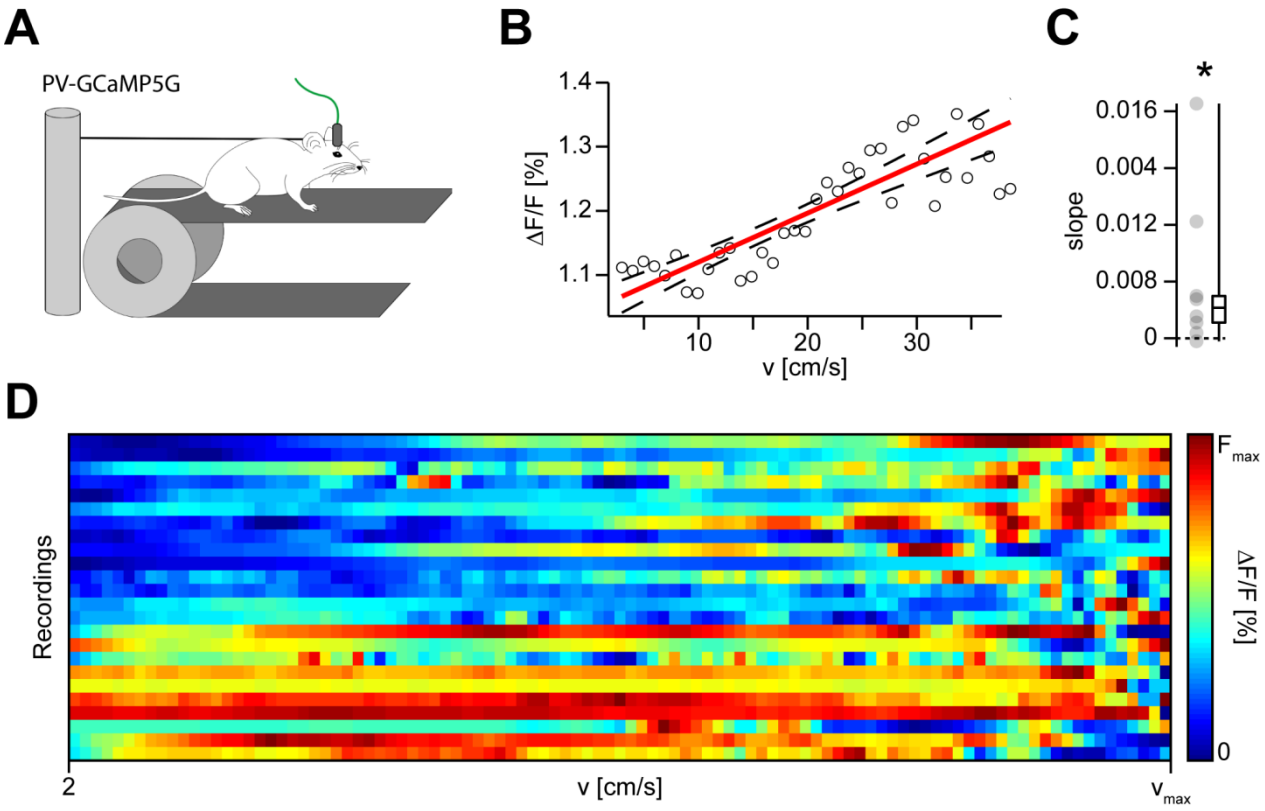


**Figure 18:** PV-GCaMP5G fluorescence is positively correlated to the velocity of locomotion

**A** Illustration of a head fixed PV-GCaMP5G animal on a linear treadmill with the light fiber patch cord attached. **B** Exemplary interrelation of binned velocity to changes in fluorescence intensity (circles), a weighted linear fit of the data (red), and the respective confidence interval of the fit (dashed line). **C** Median slope of fits of 8 recorded animals; single animal data depicted as circles. **D** Interrelation of normalized velocity to changes in normalized fluorescence intensity shown for all recorded data.

### 3.2.2. Onset and offset of locomotion is represented in the activity of septal PV$^+$ neurons

To relate population activity of PV$^+$ neurons in the MS to changing locomotor states, the ΔF/F traces were aligned to the previously described movement phase's onset, end of acceleration, start of deceleration, and offset (**Figure 19**).

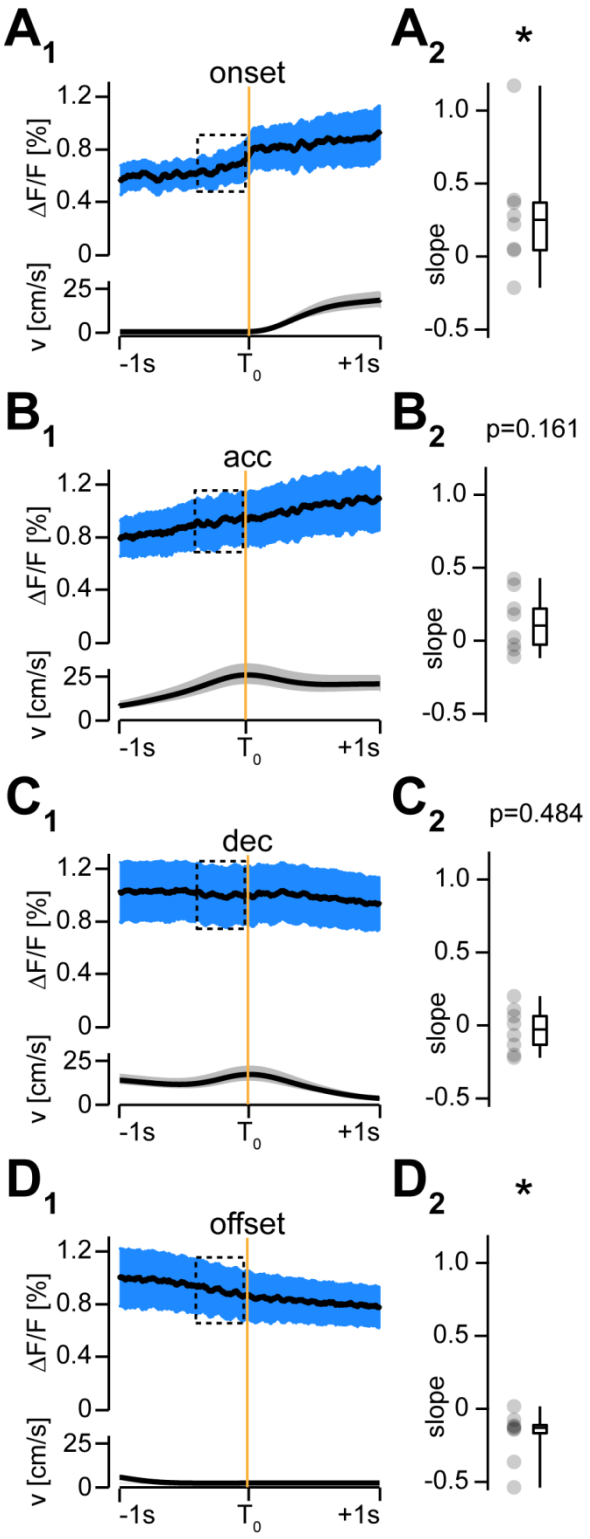


**Figure 19:** Movement related PV-GCaMP5G transients display state specific changes during onset and termination phases

**$A_1$** Top: changes in GCaMP5G intensity (MEAN shown in black; SEM shown in red) aligned to the *onset* of locomotion ($T_0$, orange line) and the corresponding velocity trace (bottom; MEAN shown in black; SEM shown in red). **$A_2$** Median of slopes of the interval indicated by the dashed box on GCaMP5G traces; single animal data depicted as circles. **$B_1$**, **$B_2$** like $A_1$ and $A_2$ with alignment point *end of acceleration* (acc), **$C_1$**, **$C_2$** like $A_1$ and $A_2$ with alignment point *start of deceleration* (dec), and **$D_1$**, **$D_2$** like $A_1$ and $A_2$ with alignment point *offset* of locomotion (offset).

Deep brain fiberoptometry via the implanted light fiber enabled monitoring of $Ca^{2+}$-dependent fluorescence transients originating from GABAergic $PV^{+}$ neurons in the MS. Fluorescence remained at baseline level before movement onset, but started to increase during the immediate 400 ms time interval prior to the alignment point (**Figure 19A$_1$**). The slopes of the linearly fitted ΔF/F during this short period were statistically tested (see chapter 2.4.2) and the positive median was significantly different from 0 (**Figure 19A$_2$**; n=8, μ=0.25 [%], p=0.036). During the subsequent acceleration peaking at $T_0$ of the acc phase $Ca^{2+}$-dependent transients were highly variable among the animals tested (**Figure 19B$_1$**; blue area). Statistical testing of the slopes during the 400 ms interval prior to the alignment point showed that the ΔF/F increase was not statistically significant (**Figure 19B$_2$**; n=8, μ=0.11 [%], p=0.161). This characteristic leveling of the ΔF/F prior to the velocity peak perfectly resembled the findings in VGluT2-GCaMP5G animals (**Figure 19B$_2$**). Over the course of movement, GCaMP intensity remained at elevated levels as previously demonstrated (**Figure 19B**; rest versus run comparison) and decreased slowly once the animal slowed down (**Figure 19C$_1$**, **D$_1$**). During the deceleration phase, the analysis of the slopes was not different from 0 prior to $T_0$ (**Figure 19C$_2$**; n=8, μ=-0.03 [%], p=0.484) while displaying a negative slope during the 400 ms interval before the offset of movement (**Figure 19D$_2$**; n=8, μ=-0.13 [%], p=0.017). As mentioned in chapter 3.1.3 (VGluT2-GCaMP5G alignment), GCaMP5G ΔF/F levels required more than 2 s to reach baseline levels (**Figure 19D$_1$**, showing ongoing decay of ΔF/F 1 s after standstill).

## 3.3. In-vivo monitoring of oscillatory activity in hippocampal CA1 stratum pyramidale

Brain regions structured in layers tend to display oscillatory activity caused by current flowing in specific patterns. Under physiological conditions, rhythmic activity in the hippocampal CA1 pyramidal cell layer typically oscillated at frequencies between 4-12 Hz in mice (see chapter 1.6). These theta oscillations could be recorded using electrodes terminating close to the very cell layer. Changes in the potential of the local field represented changes in the general population activity in the area.

### 3.3.1. Power and peak frequency of HC CA1 LFP increased in theta range

The electrical local field in hippocampal CA1 was routinely monitored with custom-made tungsten wire electrodes which were chronically implanted into pyramidal cell layer in s.p. (**Figure 20A**). The LFP signal was monitored while the habituated and head-fixed animal was moving voluntarily on a linear treadmill. The recorded theta oscillations were changed when the immobile animal began to move (**Figure 20B**). Direct comparison of resting and running periods (**Figure 20C**) revealed an increase in theta mean power (**Figure 20D**; n=41, $\mu_{rest}=2.63*10^{-6}$ [$\mu V^2/Hz$], $\mu_{run}=3.24*10^{-6}$ [$\mu V^2/Hz$], p=0.001). Moreover, the peak frequency of the occurring oscillation was increased after the transition from resting to running (**Figure 20E**; n=41, $\mu_{rest}=6.16$ [Hz], $\mu_{run}=6.92$ [Hz], $p<0.0001$). Taken together, the adaption of the oscillatory activity indicated an increase in activity of the whole neuronal population in hippocampal CA1 s.p.

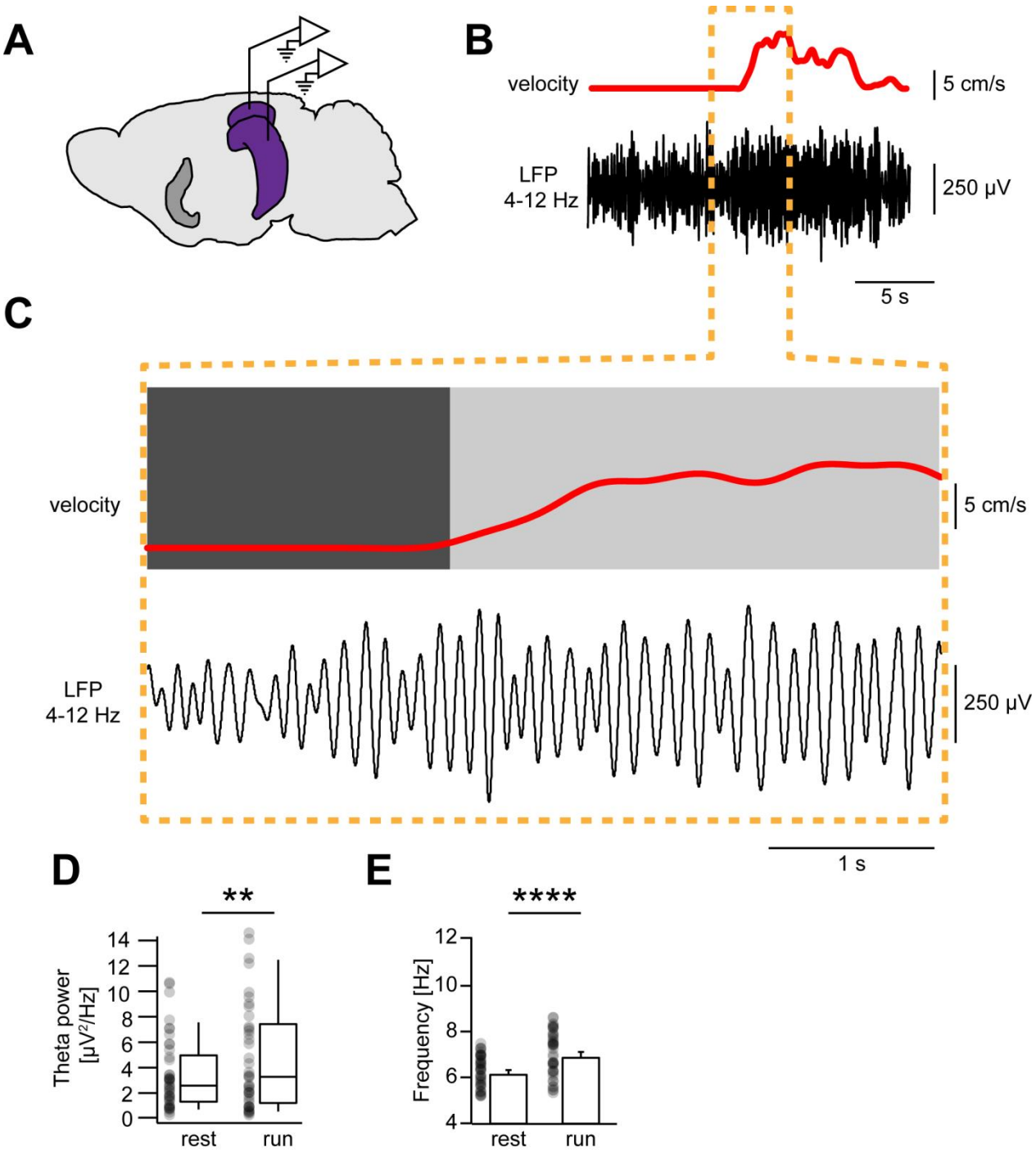


**Figure 20:** Theta oscillation power and peak frequency increase during locomotion

**A** Schematic illustration of local field potential electrodes implanted into the HC. **B** Exemplary local field potential signal (black) and the corresponding velocity trace (red). **C** Enlarged section in B with the velocity trace displaying a period of resting (dark grey area) in contrast to a running period (light grey area). The oscillatory local field potential is shown in below. **D** Comparison of median theta power and **E** Mean theta peak frequency during resting intervals and running intervals; single animal data depicted as circles.

### 3.3.2. Frequency specific representation of locomotion in hippocampal CA1 pyramidal layer

As described before, the transition from immobility to locomotion is accompanied by changes in the attributes of theta oscillation occurring in the HC (**Figure 21A**). Splitting theta oscillations into its spectrum of frequencies, the most prominent oscillations could be found between 6-10 Hz (**Figure 21B**). Focusing on single-Hz frequency bands depicted frequency-specific encoding of locomotion (**Figure 21C**-**J**). Oscillations between 4-7 Hz were low in amplitude during periods of running (**Figure 21C**, **D**, **E**). Higher frequencies from 7-10 Hz were strongest during locomotion (**Figure 21F**, **G**, **H**), while oscillatory events at frequencies faster than 10 Hz displayed only little amplitudes overall (**Figure 21I**, **J**). Quantification of the respective power traces of each frequency band (**Figure 21K**) revealed decreasing power in the 4 Hz and 5 Hz frequency band (Theta 4 Hz: n=41, $\mu_{run/rest}$=0.53 [%], p<0.0001; Theta 5 Hz: n=41, $\mu_{run/rest}$=0.7 [%], p<0.0001). Oscillations at the frequency band of 7 Hz and 8 Hz were increased during running (Theta 7 Hz: n=41, $\mu_{run/rest}$=1.42 [%], p<0.0001; Theta 8 Hz: n=41, $\mu_{run/rest}$=1.26 [%], p=0.001). Higher frequencies in the frequency band of 10 Hz and 11 Hz again showed decreasing mean power (Theta 10 Hz: n=41, $\mu_{run/rest}$=0.81 [%], p=0.001; Theta 11 Hz: n=41, $\mu_{run/rest}$=0.84 [%], p<0.0001). The intermediate frequency bands at 6 Hz and 9 Hz were unchanged (Theta 6 Hz: n=41, $\mu_{run/rest}$=0.84 [%], p=0.636; Theta 9 Hz: n=41, $\mu_{run/rest}$=0.9 [%], p=0.876). Subsequently, similar behaving frequency bands encoding locomotion were combined into larger frequency bands defined as theta 4-6 Hz, theta 7-9 Hz, and theta 10-12 Hz (**Figure 21K**).

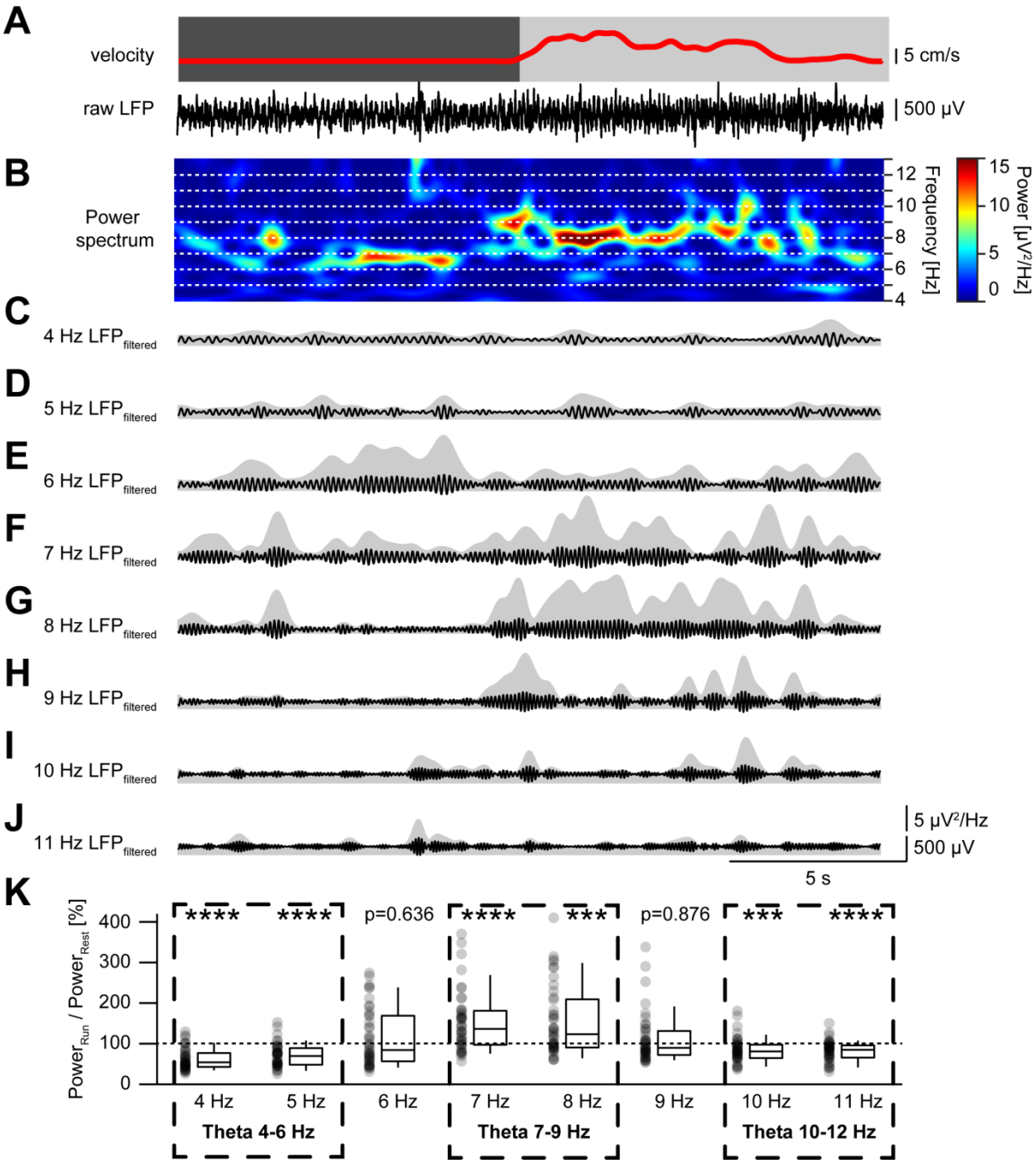


**Figure 21:** HC Theta frequency bands change in amplitude during locomotion

**A** Exemplary velocity trace (red) including a resting interval (dark grey area) and a running interval (light grey area) with the corresponding LFP below (black). **B** Power spectrogram of the LFP in A between 4 to 12 Hz; the dashed lines confining 1 Hz frequency bands. **C-J** Filtered LFP signal (black line) of the 1 Hz frequency bands shown in B with the mean power shown as grey area. **K** Comparison of median theta power during resting intervals and running intervals for every frequency band; single animal data depicted as circles for every 1 Hz frequency band shown in C-J; single animal data depicted as circles. The dashed boxes indicate similar frequency bands depending on their kinetics: Theta 4-6 Hz, theta 7-9 Hz, and theta 10-12 Hz.

### 3.3.3. Hippocampal theta oscillations increase in both peak frequency and amplitude in correlation to the movement speed

To investigate potential speed modulation of theta oscillations in the hippocampal CA1 region, the LFP signal was separately tested in regard of theta frequency (peak frequency), theta mean power, theta 4-6 Hz amplitude, theta 7-9 Hz amplitude, and theta 10-12 Hz amplitude (**Figure 22**). Theta mean power was correlated to the binned velocity (**Figure 22A$_1$**) and linearly fitted, considering the absolute duration of each velocity bin by weighting the fit (**Figure 22A$_1$**; red line). The majority of recordings showed comparable distribution of data points in this correlation (**Figure 22A$_3$**). Slopes of the fits were tested and showed a positive correlation of theta mean power and velocity (**Figure 22A$_2$**; n=41, $\mu=3.11e^{-8}$ [slope], p=0.001). The peak frequency of the contemporary oscillation was correlated to the same velocity bins (**Figure 22B$_1$**). The overall relation appeared similar to the findings on theta mean power (**Figure 22B$_2$**), and statistical analysis of the slopes revealed a positive correlation of peak frequency to speed during running (**Figure 22B$_2$**; n=41, $\mu=0.012$ [slope], p=0.001). This positive correlation was observed in more than 80 % of the recorded animals. Plotting the lower theta frequencies 4-6 Hz versus each velocity bin differed from the previous findings (**Figure 22C$_1$**, **C$_3$**) and quantification of the estimated slopes showed no significant modulation (**Figure 22C$_2$**; n=41, $\mu=-3.8e^{-9}$ [slope], p=0.115). The interrelation of the theta 7-9 Hz frequency band and velocity (**Figure 22D$_1$**) matched the kinetics seen for theta mean power and peak frequency (**Figure 22D$_3$**), with the statistical analysis confirming a positive correlation (**Figure 22D$_2$**; n=41, $\mu=1.02e^{-8}$ [slope], p=0.001). The highest frequencies in the frequency band between 10-12 Hz were low in amplitude (**Figure 22E$_1$**) and seemed to anti-correlate to the velocity (**Figure 22E$_3$**), even though the slope analysis evidenced a median slope indifferent to 0 (**Figure 22E$_2$**; n=41, $\mu=-1.36e^{-9}$ [slope], p=0.098). Nevertheless, except for theta 7-9 Hz, the mean amplitude of theta frequency bands were decreasing while velocity increased (**Figure 22C$_3$**, **E$_3$**).

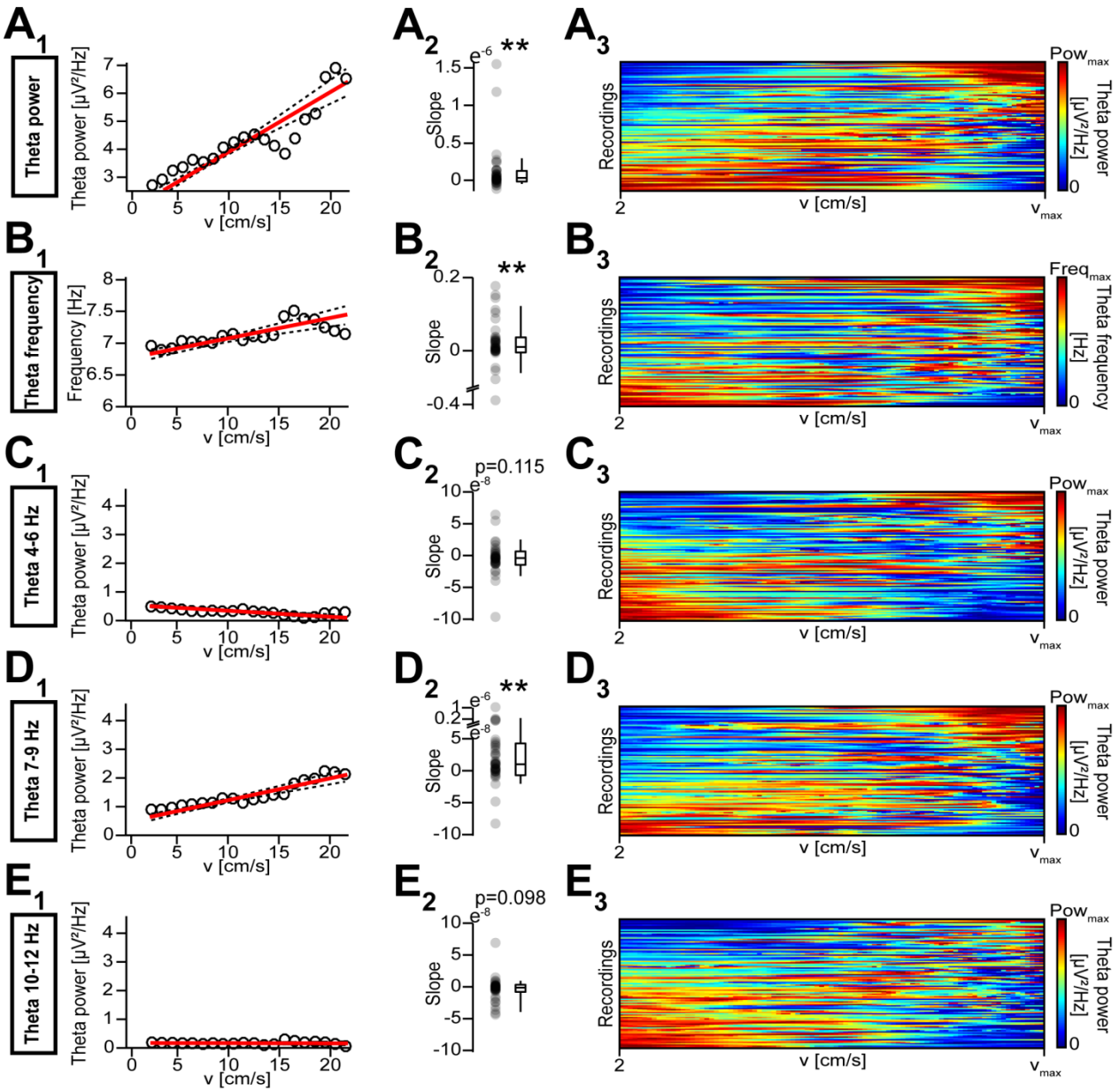


**Figure 22:** Theta oscillations are positively correlated to the velocity of locomotion

**$A_1$** Exemplary interrelation of binned velocity to mean theta power between 4-12 Hz (circles), a weighted linear fit of the data (red), and the respective confidence interval of the fit (dashed line). **$A_2$** Median slope of fits of all recorded animals. **$A_3$** Interrelation of normalized velocity to normalized mean theta power between 4-12 Hz shown for all recorded data (99 recordings in 42 animals). **$B_1$, $B_2$, $B_3$** same as $A_1$, $A_2$, $A_3$ for theta peak frequency. **$C_1$, $C_2$, $C_3$** same as $A_1$, $A_2$, $A_3$ for theta 4-6 Hz frequency band. **$D_1$, $D_2$, $D_3$** same as $A_1$, $A_2$, $A_3$ for theta 7-9 Hz frequency band. **$E_1$, $E_2$, $E_3$** same as $A_1$, $A_2$, $A_3$ for theta 10-12 Hz frequency band.

### 3.3.4. Hippocampal theta oscillation frequency bands contain information on changes in the movement state

Following the reproducible detection of movement phase alignment points the three theta frequency bands theta 4-6 Hz, theta 7-9 Hz, and theta 10-12 Hz were analyzed corresponding to each locomotion state. Referring to the varying velocity modulation of theta described previously, strong differences were expected in the kinetics of theta band powers over the course of a movement interval (**Figure 23**). The changes in velocity during the distinct movement states were consistent among all recorded animals (**Figure 23A$_1$-A$_4$**) and changes in the LFP were addressed with the slope analysis (see chapter 2.4.2). The mean power spectrum between 4-12 Hz showed a clear shift towards higher frequencies around the onset point (**Figure 23B$_1$**). This increase in theta peak frequency and power was also visible in the acc phase (**Figure 23B$_2$**), and the dec phase (**Figure 23B$_3$**), but faded away during the offset phase (**Figure 23B$_4$**). Quantification of the mean power for each frequency band during the onset interval (**Figure 23C$_1$**, **D$_1$**, **E$_1$**) revealed a decrease of theta 4-6 Hz mean power during the 400 ms interval prior to locomotion onset (**Figure 23F$_1$**; n=26, $\mu$=-2.38e$^{-7}$ [slope], p=0.0.001). In contrast, the theta 7-9 Hz band displayed an increase in the mean power (**Figure 23F$_1$**; n=26, $\mu$=3.91e$^{-7}$ [slope], p=0.001), while theta 10-12 Hz was unchanged (**Figure 23F$_1$**; n=26, $\mu$=-3.93e$^{-9}$ [slope], p=0.732). Before the end of the acceleration (**Figure 23C$_2$**, **D$_2$**, **E$_2$**) the 4-6 Hz frequency band was still decreasing (**Figure 23F$_2$**; n=26, $\mu$=-4.16$^{-8}$ [slope], p=0.0.049). Theta between 7-9 Hz and 10-12 Hz showed insignificant kinetics during the acc phase (**Figure 23F$_2$**; Theta 7-9 Hz: n=26, $\mu$=-4.16e$^{-8}$ [slope], p=0.638; Theta 10-12 Hz: n=26, $\mu$=-1.96e$^{-8}$ [slope], p=0.517). In the deceleration interval, the low frequencies ranging from 4-6 Hz (**Figure 23C$_3$**) began to increase in mean power (**Figure 23F$_3$**; n=31, $\mu$=7.62e$^{-8}$ [slope], p=0.007). Theta 7-9 Hz (**Figure 23D$_3$**) and theta 10-12 Hz (**Figure 23E$_3$**) displayed no changes in the dec phase (**Figure 23F$_3$**; Theta 7-9 Hz: n=31, $\mu$=-9.13e$^{-8}$ [slope], p=0.068; Theta 10-12 Hz: n=31, $\mu$=-5.51e$^{-10}$ [slope], p=0.433).

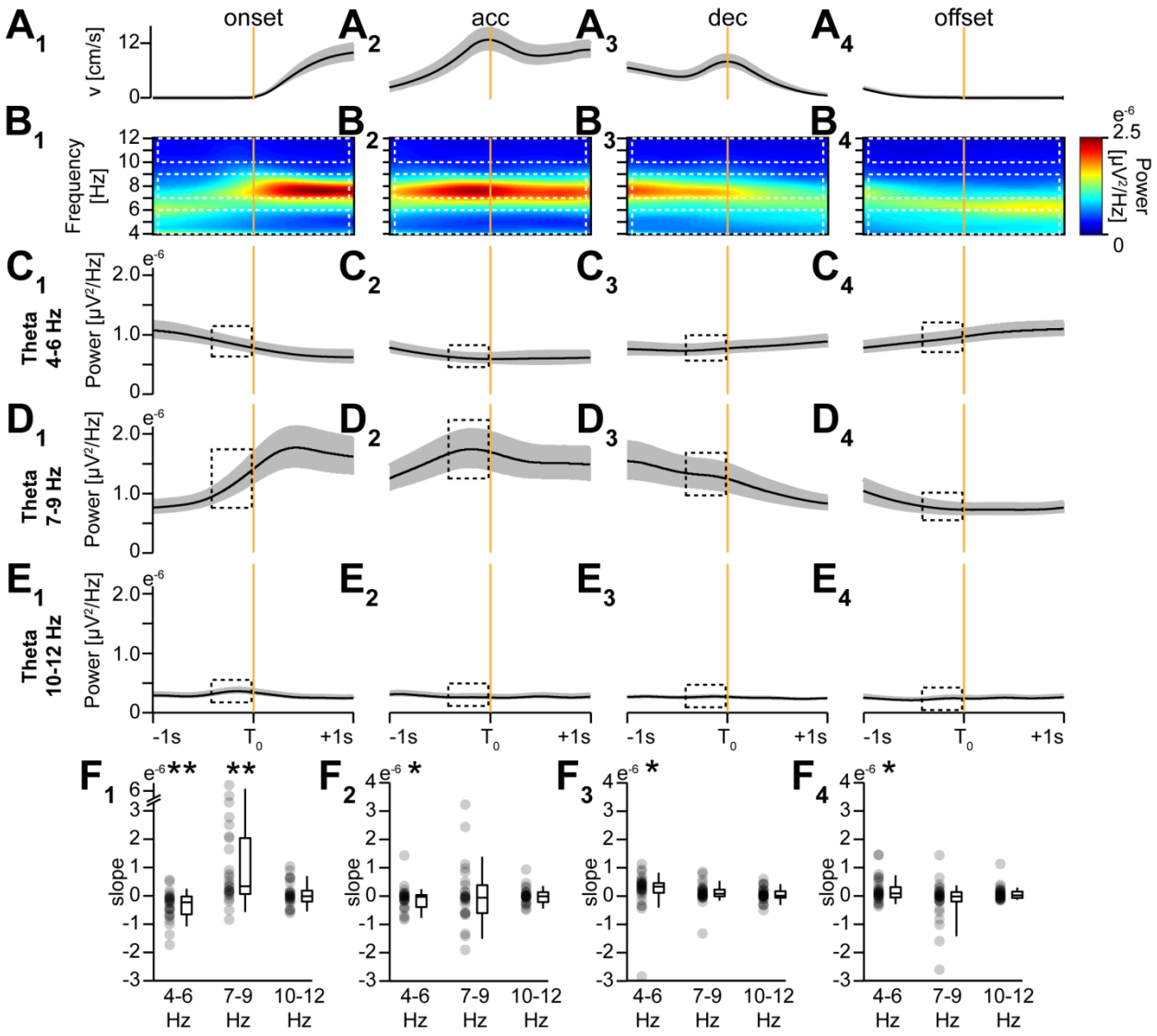


**Figure 23:** Theta frequency band-specific changes during states of movement

**$A_1$-$A_4$** Averaged velocity trace (MEAN shown in black; SEM shown in grey) aligned to the defined time point (orange line) during the movement phases onset, end of acceleration (acc), start of deceleration (dec), and offset. **$B_1$, $B_2$, $B_3$, $B_4$** Averaged power spectrogram of LFP recordings between 4-12 Hz aligned to movement phases shown in A; the dashed lines mark the frequency bands between 4-6 Hz (bottom), 7-9 Hz (middle), and 10-12 Hz (top). **$C_1$, $C_2$, $C_3$, $C_4$** Averaged mean power of the theta 4-6 Hz frequency band (MEAN shown in black; SEM shown in grey) aligned to the alignment point $T_0$ (orange line); the dashed box indicates the interval taken for the slope calculation of a linear fit prior to the alignment point (shown in F). **$D_1$, $D_2$, $D_3$, $D_4$** same as C for theta 7-9 Hz. **$E_1$, $E_2$, $E_3$, $E_4$** same as C for theta 10-12 Hz. **$F_1$, $F_2$, $F_3$, $F_4$** Median slopes of fits for the three frequency bands and all recorded animals with at least 5 alignments per phase ($n_{onset}$=26, $n_{acc}$=26, $n_{dec}$=31, $n_{offset}$=31).

Prior to termination of movement, the theta 4-6 Hz frequency band (**Figure 23C$_4$**) displayed still increasing mean power (**Figure 23F$_4$**; n=31, μ=8.25e$^{-8}$ [slope], p=0.018). Theta 7-9 Hz and theta 10-12 Hz (**Figure 23D$_4$**, **E$_4$**) were unaffected during this period (**Figure 23F$_4$**; Theta 7-9 Hz: n=31, μ=-2.49e$^{-8}$ [slope], p=0.41; Theta 10-12 Hz: n=31, μ=-1.18e$^{-8}$ [slope], p=0.217). Changes in the kinetics of the 7-9 Hz frequency band mean power (**Figure 23D$_1$-D$_4$**) preceded every detected movement phase (**Figure 23B$_1$ B$_4$**). Yet, the statistical analysis of the data during the movement phases could only confirm an increase prior to the onset of locomotion (**Figure 23F$_1$-F$_4$**). To evaluate this kinetics statistically, a modified analytical approach would be required.

### 3.4. Intraseptal neuronal ensemble activity represents movement

Using multi-unit electrodes and velocity read-out simultaneously, representation of locomotion in the single neuron activity could be investigated. Acute electrophysiological recordings of multi-unit activity in the MS were performed by stereotactically placing electrode arrays into the central regions in the MS (**Figure 24A**). Active neurons were then identified as *single units* using information on firing rate and waveform of the recorded APs afterwards. The timing and frequency of APs could be analyzed in in correlation to the velocity of the animal (**Figure 24B**). Many units were identified that displayed high firing rates during running periods (**Figure 24C**; light grey area behind the velocity trace) while firing at lower rates or non-firing at all during resting intervals (dark grey areas). The summed activity of all units recorded by one electrode array during a single recording session consistently showed high activity during running; yet, this multi-unit activity could be dominated by highly active units with the majority of units behaving in a different fashion. Therefore a single-unit analysis rather than a population approach was required. Quantification of the ratio between firing rate during movement ($Freq_{run}$) and firing frequency during immobility ($Freq_{rest}$) indicated that units in the MS tended to discharge APs more often while the animals were in motion (**Figure 24D**; n=320, μ=1.21, p<0.0001).

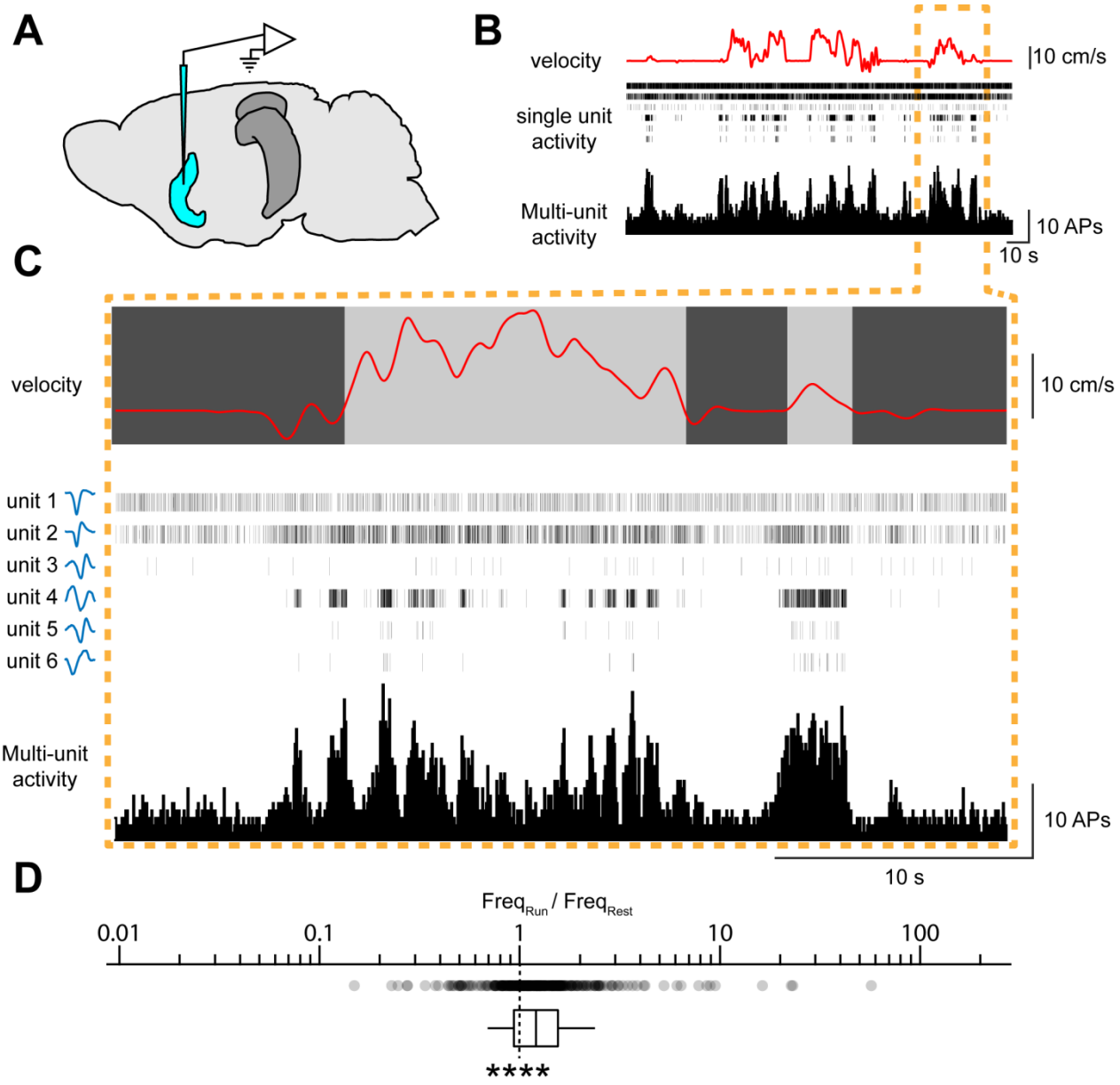


**Figure 24:** MS unit firing frequency shows dependence on locomotor activity

**A** Schematic illustration of an acute tetrode recording in the MS. **B** Exemplary recording showing the velocity (red), single-unit activity of 6 recorded units (black markers), and the combined multi-unit activity recorded with one tetrode (black bars). **C** Enlarged section in B, with the velocity trace displaying a period of resting (dark grey area) in contrast to a running period (light grey area). The single-unit activity for 6 units (waveform of each unit shown as blue curve next to the unit number) is presented as AP time points (black markers), with the overall multi-unit activity shown below (black bars). **D** Median ratio of mean firing frequency during running intervals to resting intervals for all recorded single-units in the MS; single animal data depicted as circles.

### 3.4.1. MS unit activity heterogeneously modulated by velocity

The detailed investigation of speed dependent increase of unit activity yielded information about how single neurons in the MS (**Figure 25A**) alter their electrophysiological output frequencies when the animal moves at different velocities. Correlation of AP frequency versus 1 cm/s velocity bins enabled the calculation of weighted linear fits for each unit (**Figure 25B**; red line). The slope of each fit was used as an indicator of velocity modulation. The statistical analysis of these slopes detected an overall positive speed modulation of units in the MS (**Figure 25C**; n=314, μ=0.013 [slope], p=0.031). A sorted presentation of all calculated correlations for every unit showed opposing modulations in large populations of MS units (**Figure 25D**). This observation could be confirmed after counter-checking the confidence intervals of the respective linear fits for positive lower and negative upper bounds respectively (see chapter 2.4.5). The individual mathematical evaluation of every single-unit revealed significant speed modulation in a subset of units (**Figure 25E**). The approach identified 49/314 positively speed modulated units (**Figure 25F$_1$**; $\mu_{pos}$=0.203 [slope]), 228/314 unmodulated units (**Figure 25F$_2$**; $\mu_{non}$=0.009 [slope]), and 37/314 negatively speed modulated units (**Figure 25F$_3$**; $\mu_{neg}$=-0.165 [slope]) in the MS.

### 3.4.2. Theta coupling in MS single-units

MS activity is crucial for generation of hippocampal theta oscillations. To assess the theta modulation of the recorded units in the MS, the AP timing was correlated to the phase of theta oscillation (see chapter 2.4.3). By individually determining whether a MS unit was linked to the theta cycle in the HC, a fraction of cells could be identified to be preferentially active at distinct phases of theta (**Figure 26A$_1$**; n=128 ≡ 40 %).Yet, the majority of units showed no significant theta phase-modulation (**Figure 26A$_2$**; n=212 ≡ 60 %). Preferred theta phases were homogeneously distributed and ranged primarily from 103 ° to 243 ° (**Figure 26B$_1$**; $\mu_{phase}$=173 °), and the average of phase modulated units showed no preference for a theta phase on the population level (**Figure 26B$_2$**). In the next step, AP firing was analyzed by auto correlating single-unit AP output.

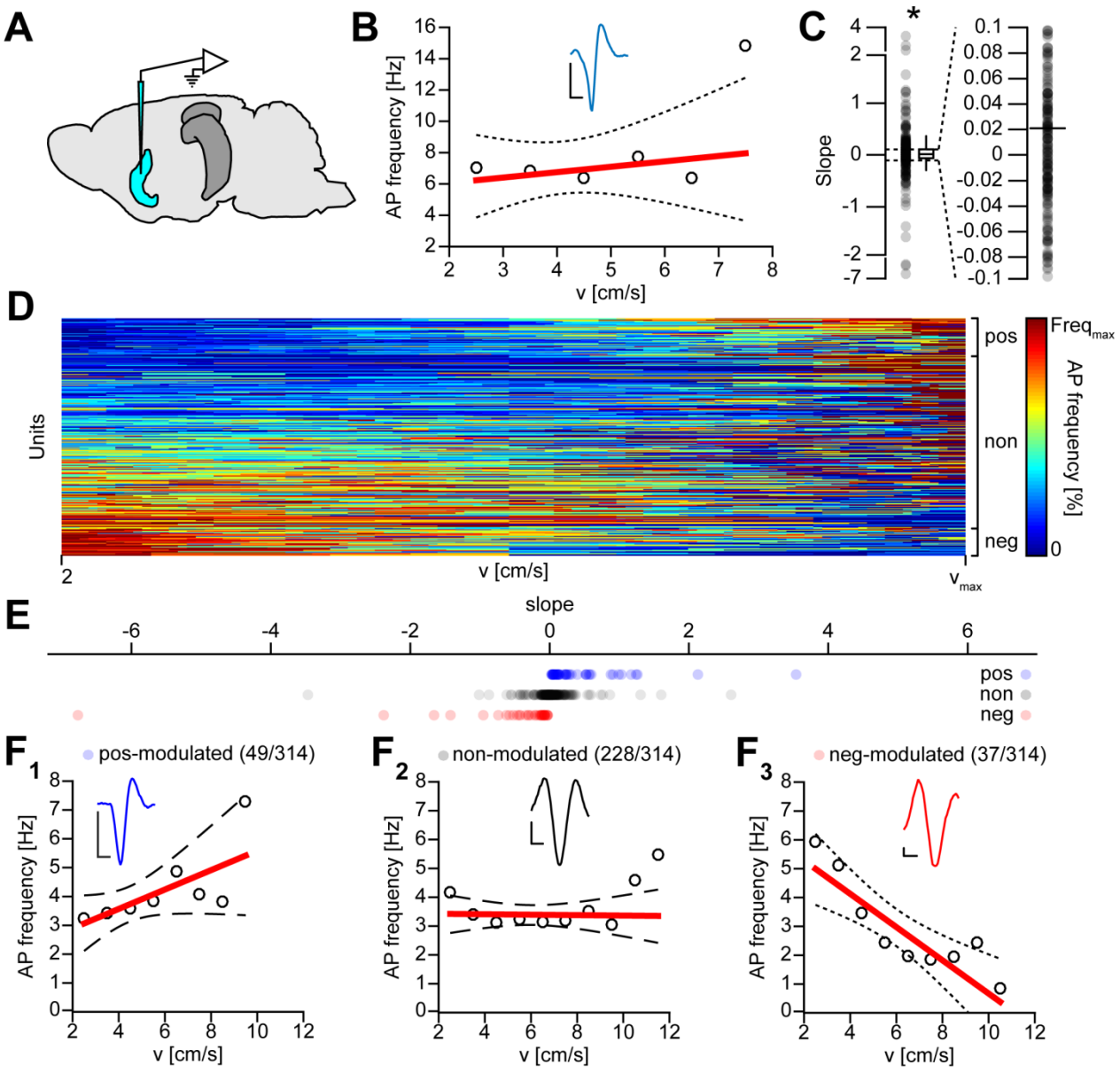


**Figure 25:** Global MS unit activity sensitive to changes in velocity

**A** Schematic illustration of an acute tetrode recording in the MS. **B** Exemplary single-unit (waveform shown as blue curve) interrelation of binned velocity to AP frequency (circles), a weighted linear fit of the data (red), and the respective confidence interval of the fit (dashed line); scale bar of the inset: 200 µV/1 ms. **C** Median slope of fits of all recorded MS single-units; single unit data depicted as circles. **D** Interrelation of normalized velocity to normalized firing frequency shown for all recorded single-units (n=314). **E** Slopes shown in C divided into significantly positive, significantly negative, and insignificant slopes. **$F_1$** Exemplary interrelation of a positively-modulated (n=49), **$F_2$** a negatively-modulated (n=37), and **$F_3$** an unmodulated (n=228) single-unit (waveform shown as inset; scale bar 200 µV/1 ms).

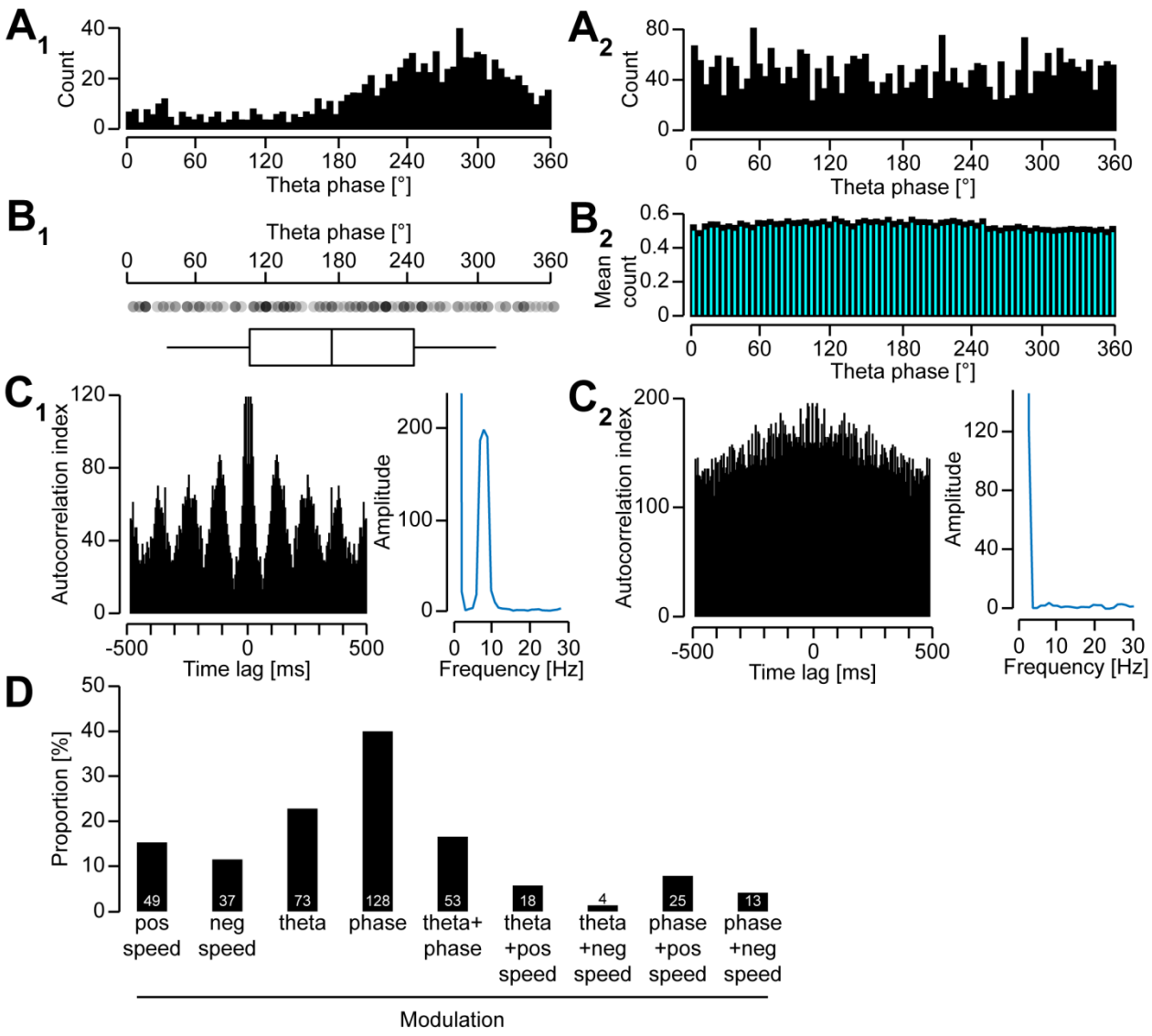


**Figure 26:** MS single-unit firing is modulated by speed and theta

**$A_1$** Histogram of APs fired by a significantly phase-modulated single-unit during a theta cycle. **$A_2$** Histogram of APs fired by a non-phase-modulated single-unit during a theta cycle. **$B_1$** Preferred theta phases of phase modulated single-units. **$B_2$** Averaged histogram of APs fired by all significantly phase-modulated single-units (MEAN in cyan; SEM in black) during a theta cycle. **$C_1$** Left: Autocorrelation of AP firing for a theta-modulated single-unit. Right: FFT of the autocorrelation displaying a peak at ~9 Hz. **$C_2$** Left: autocorrelation of AP firing for a non-theta-modulated single-unit. Right: FFT of the autocorrelation. **D** Proportion of units being modified in their AP firing. Modulations shown are: positive speed-modulation (pos speed), negative speed-modulation (neg speed), theta-modulation (theta), phase-modulation (phase), and combinations of different modulations.

The autocorrelation revealed a subset of units that fired significantly at frequencies between 4-12 Hz (**Figure 26C$_1$**; n=73 ≡ 22.81 %), with the rest firing at various frequencies (**Figure 26C$_2$**; n=247 ≡ 77.19 %). In general, MS units were affected by different modulations ranging from positive and negative speed-modulation (**Figure 25**) to theta frequency-modulation and phase-modulation (**Figure 26D**). Interestingly, units that were positively correlated to movement speed were more likely to be modulated by the phase of theta (n=25 ≡ 7.81 %) or fire in theta frequency (n=18 ≡ 5.6 %) as well, while among negatively speed-modulated units only 4.06 % (n=13) were additionally phase-modulated and 1.25 % (n=4) fired significantly at in theta range.

### 3.4.3. MS multi-unit activity heterogeneously encodes movement phases

Despite the heterogeneous characteristics of MS multi-unit activity, mean firing rates of all units were aligned to the movement phases as described previously (**Figure 27**; see chapter 2.4.1). This analysis should conclude whether neurons in the MS not only encode the speed of an animal but also the coming movement state (see chapter 2.4.2). Surprisingly, during the onset phase of a locomotion interval (**Figure 27A$_1$**) the firing rate did not increase prior to movement initiation. Although the linear representation of the 400 ms interval prior to the alignment point was positive in general, quantification of the single slopes was insignificant for the complete population of MS units (**Figure 27A$_2$**; n=159, μ=0.0034 [slope], p=0.065).

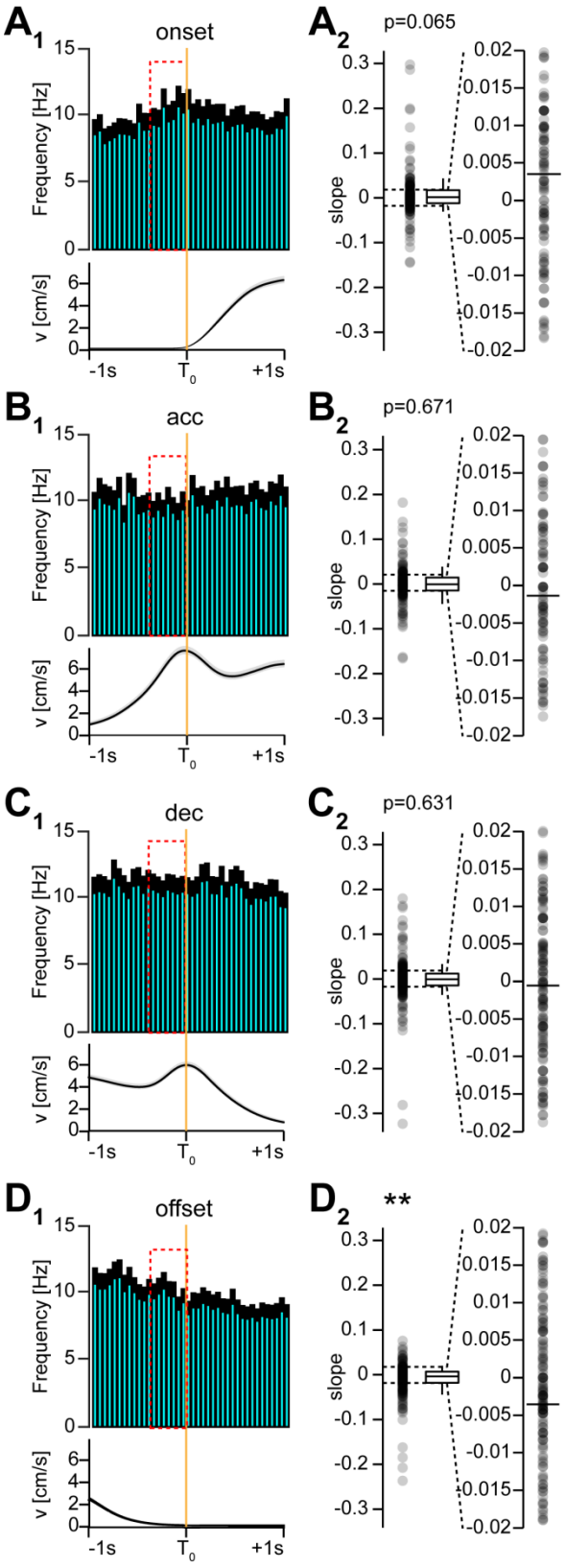


**Figure 27:** Global MS unit activity heterogeneously adapts to the state of locomotion

**$A_1$** Top: Averaged 50-ms time bins of MS multi-unit AP frequency (MEAN shown in cyan; SEM shown in black) aligned to the defined *onset* time point at $T_0$ (orange line) and the corresponding velocity (bottom; MEAN shown in black; SEM shown in grey). **$A_2$** Median of slopes of the interval indicated by the dashed box on the AP frequency trace with the range close to the median being enlarged; single animal data depicted as circles. **$B_1$**, **$B_2$** same as $A_1$ and $A_2$ for alignment point *end of acceleration* (acc). **$C_1$**, **$C_2$** same as $A_1$ and $A_2$ for alignment point *start of deceleration* (dec). **$D_1$**, **$D_2$** same as $A_1$ and $A_2$ for alignment point *offset of locomotion* (offset).

The increase in firing rate during the transition from immobility to locomotion was clearly visible in the multi-unit activity, and general activity remained at high levels over the course of movement (**Figure 27A$_1$** right side, **B$_1$**, **C$_1$**, and **D$_1$** left side). Still, in the end of the acceleration phase (**Figure 27B$_1$**) and at the start of the deceleration (**Figure 27C$_1$**) the slope analysis showed highly heterogeneous kinetics in septal multi-unit activity (**Figure 27B$_2$**; acc: n=159, μ=-0.0013 [slope], p=0.671; **Figure 27C$_2$**; dec: n=209, μ=-0.0007 [slope], p=0.631). The termination of locomotion at the offset alignment point was preceded by a decrease in AP firing rates in the multi-unit activity (**Figure 27D$_1$**) which was validated by the slope analysis (**Figure 27D$_2$**; n=207, μ=-0.0036 [slope], p=0.001).

### 3.4.4. MS single-units predict future movement states

As the population of MS units (**Figure 28A**) was heterogeneously active during periods of locomotion, an additional approach was used to identify units that encoded information on any upcoming movement state (see chapter 2.4.2).

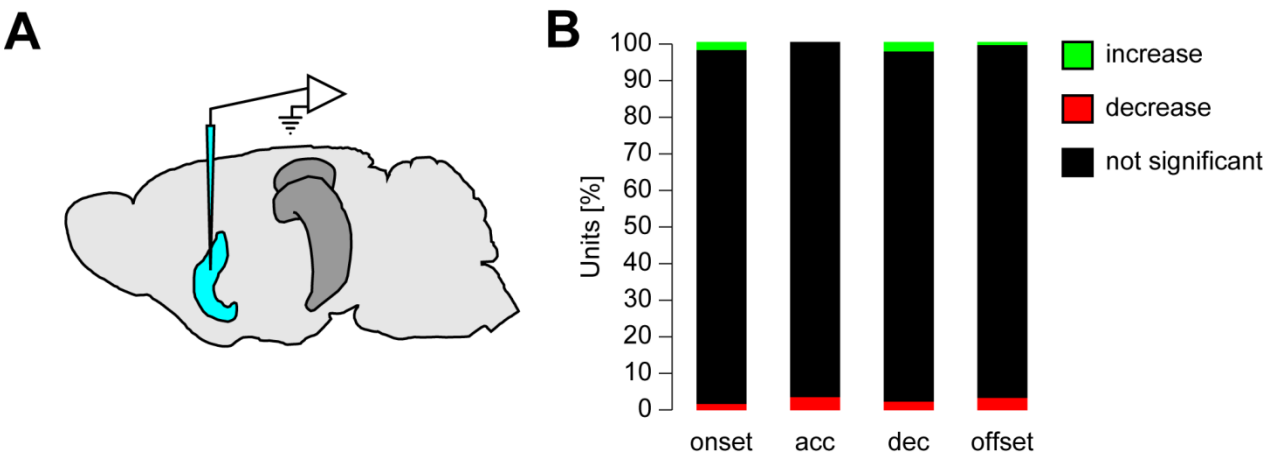


**Figure 28:** Individual MS units change their firing frequency prior to change in locomotion

**A** Schematic illustration of an acute tetrode recording in the MS. **B** Proportion of units with significantly increasing, significantly decreasing, or insignificant firing rates prior to the alignment points onset, acc, dec, and offset, respectively.

The comparison of single-unit slopes from the intervals preceding the respective alignment point (**Figure 27A$_2$**, **B$_2$**, **C$_2$**, and **D$_2$**) to a slope equal to zero (=not predictive) revealed a group of 6/159 units that were capable of reliably predicting the onset of locomotion (**Figure 28B**; increase: 4/159 ≡ 2.51 %, decrease: 2/159 ≡ 1.26 %, insignificant: 153/159 ≡ 96.23 %). The end of acceleration could be predicted by 5/159 units that decreased their firing rates (increase: 0/159 ≡ 0 %, decrease: 5/159 ≡ 3.14 %, insignificant: 154/159 ≡ 96.85 %). The beginning of the deceleration was reliably predicted by 10/209 units (increase: 6/209 ≡ 2.87 %, decrease: 4/209 ≡ 1.91 %, insignificant: 199/209 ≡ 95.21 %), while the termination of movement at the offset alignment point could be predicted in 7/207 units (increase: 1/207 ≡ 0.48 %, decrease: 6/207 ≡ 2.90 %, insignificant: 200/207 ≡ 96.62 %).

### 3.5. HC CA1 unit firing increased during running

Precisely positioned electrode arrays in CA1 were used to investigate the electrophysiological representation of locomotion in the HC (**Figure 29A**). Aligning simultaneously recorded velocity, single-unit activity, and the summed multi-unit activity (**Figure 29B**) revealed that high frequencies of AP firing were condensed in running phases (**Figure 29C**; light grey area behind the velocity trace) compared to resting phases (**Figure 29C**; dark grey area). Even short periods of immobility flanked by movement phases were clearly distinguishable in some units (**Figure 29C**; e.g. unit 3). Quantifying the ratio of AP frequency during running to AP frequency during resting revealed a 1.86-fold increase in firing frequency when the animal was in motion (**Figure 29D**; n=149, $\mu$=1.86, $p<0.0001$).

#### 3.5.1. HC single-units display diverse speed-modulation

Correlating 1 cm/s velocity bins to the respective firing frequency for each unit recorded in HC CA1 (**Figure 30A**) enabled a conclusion on speed modulation of these neurons. The slope of the weighted linear fits of the correlated data (**Figure 30B**; red line) was used to estimate the overall positive speed modulation in all hippocampal CA1 units (**Figure 30C**; n=149, $\mu$=0.036, p=0.001).

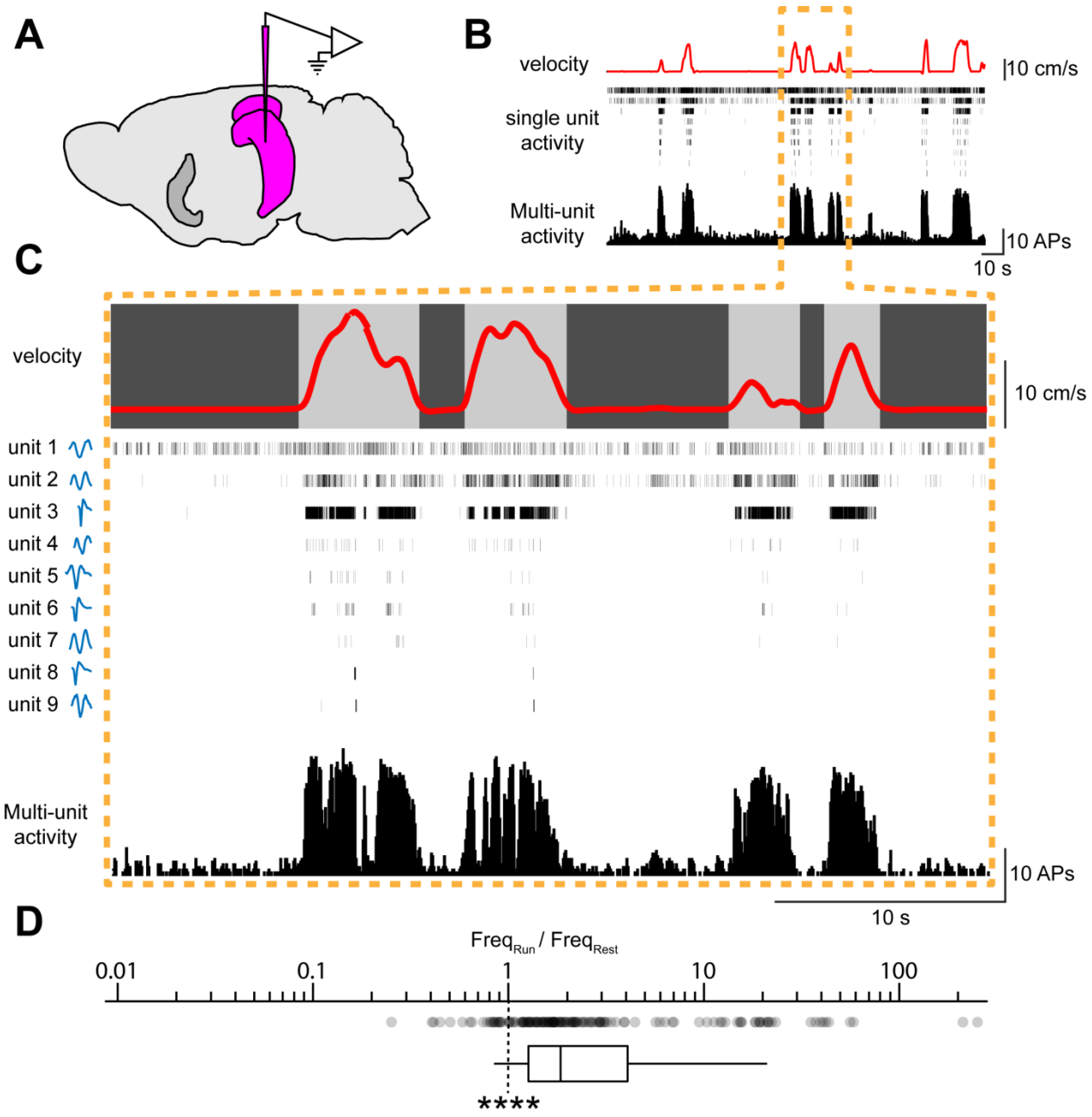


**Figure 29:** Elevated AP firing rates in HC neurons during locomotion

**A** Schematic illustration of an acute tetrode recording in the HC. **B** Exemplary recording showing the velocity (red), single-unit activity of 9 recorded units (black markers), and the combined multi-unit activity recorded with one tetrode (black bars). **C** Enlarged section of B, with the velocity trace displaying a period of resting (dark grey area) in contrast to a running period (light grey area). The single-unit activity for 9 units (waveform of each unit shown as blue curve next to the unit name) is presented as AP time points (black markers), with the overall multi-unit activity shown below (black bars). **D** Median ratio of mean firing frequency during running intervals to resting intervals for all recorded single-units in the MS; single animal data depicted as circles.

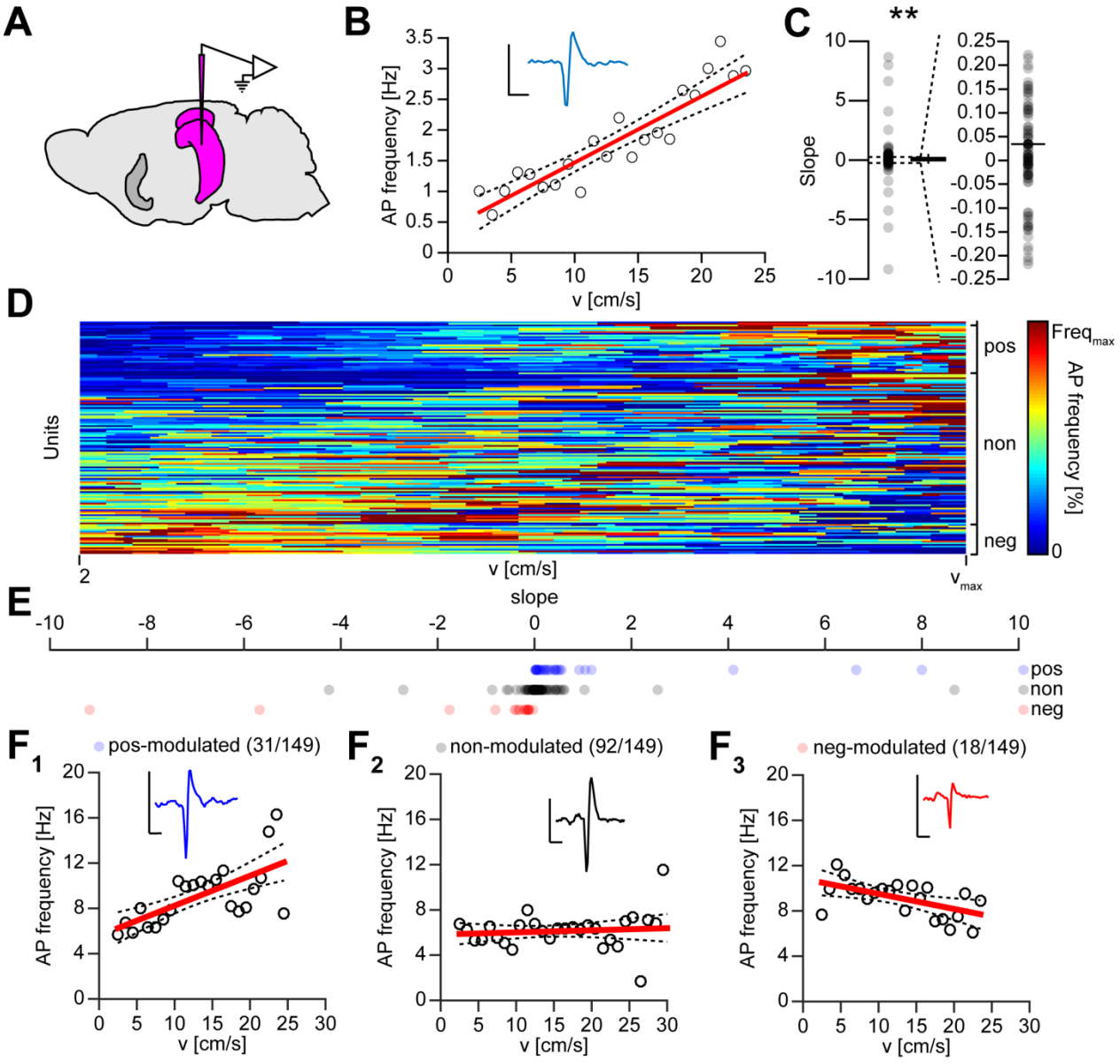


**Figure 30:** Global HC unit activity sensitive to changes in velocity

**A** Schematic illustration of an acute tetrode recording in the HC. **B** Exemplary single-unit (waveform shown as blue curve) interrelation of binned velocity to AP frequency (circles), a weighted linear fit of the data (red), and the respective confidence interval of the fit (dashed line); scale bar of the inset: 200 µV/1 ms. **C** Median slope of fits of all recorded MS single-units; single unit data depicted as circles. **D** Interrelation of normalized velocity to normalized firing frequency shown for all recorded single-units (n=314). **E** Slopes shown in C divided into significantly positive, significantly negative, and insignificant slopes. **$F_1$** Exemplary interrelation of a positively-modulated (n=49), **$F_2$** a negatively-modulated (n=37), and **$F_3$** an unmodulated (n=228) single-unit (waveform shown as inset; scale bar 200 µV/1 ms).

In order to identify variations in the speed-modulation of units within the population (**Figure 30D**), the upper/lower bounds of the confidence interval of the respective linear fit of every hippocampal unit was checked. This approach revealed subsets of differentially modulated units (**Figure 30E**). By this, an amount of 31/149 positively speed-modulated units (**Figure 30F$_1$**; $\mu_{pos}$=0.264 [slope]), 92/149 non-speed-modulated units (**Figure 30F$_2$**; $\mu_{non}$=0.018 [slope]), and 18/149 negatively-modulated units (**Figure 30F$_3$**; $\mu_{neg}$=-0.209 [slope]) were identified within the population of hippocampal units.

### 3.5.2. Single-units in HC CA1 coupled to theta phase and frequency

Theta oscillations in the HC are generated by inputs onto CA1 pyramidal cells. Yet, the activity of these cells is not necessarily dictated by the activity of the local field. To investigate how pyramidal neurons in CA1 are affected by the local field surrounding them, single-unit data acquired from HC s.p. was correlated to the LFP recorded from the contralateral hemisphere. Phase specific AP firing was found in 24.32 % of the units (**Figure 31A$_1$**; n=36) while the rest was active independent of the theta phase (**Figure 31A$_2$**; n=112 ≡ 75.68 %). Preferred theta phases were primarily between 128 ° and 268 ° (25 and 75 percentile, respectively) with the median at 233 ° (**Figure 31B$_1$**). Averaged histograms of phase modulated units revealed the largest mean count of APs at the transition from decay to rising phase between 240 ° and 280 ° (**Figure 31B$_2$**). Firing specifically in the range of theta frequency between 4-12 Hz was investigated by calculating autocorrelations for every single-unit. The Fourier-transformation of the -500 ms to +500 ms interval of the autocorrelation revealed the primary firing frequency of the individual unit. This approach detected that 20.27 % of HC units were significantly firing at theta frequencies (**Figure 31C$_1$**; n=30), leaving the rest to fire at other frequencies outside the range of theta (**Figure 31C$_2$**; n=112 ≡ 79.73 %). Still, unit firing in the HC was strongly modulated by external drives. In general, hippocampal units showed speed-modulation both positive and negative (**Figure 30**), as well as theta frequency and theta phase modulation (**Figure 31D**).

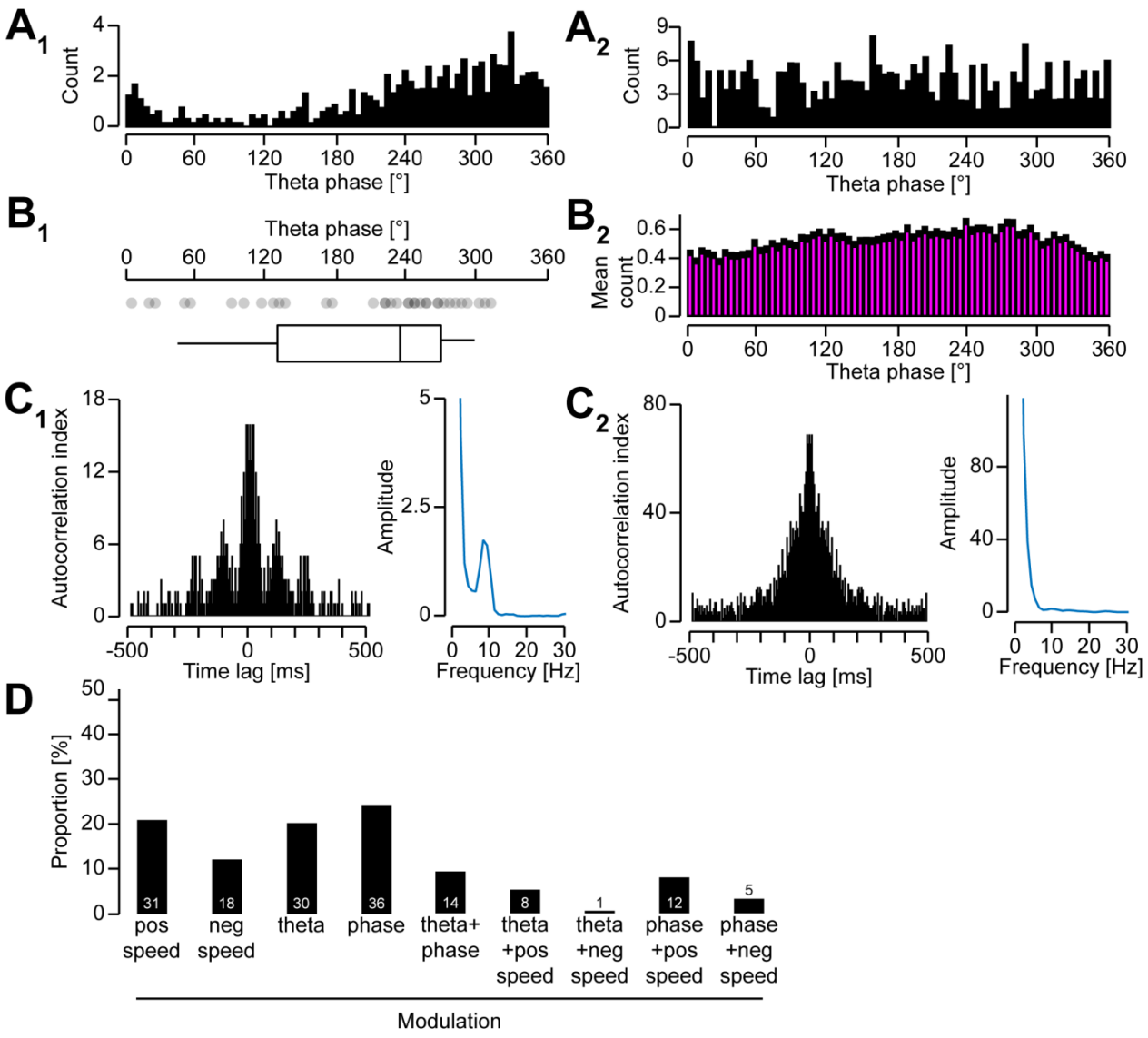


**Figure 31:** Distinct modulation of HC CA1 single-unit firing

**$A_1$** Histogram of APs fired by a significantly phase-modulated single-unit during a theta cycle. **$A_2$** Histogram of APs fired by a non-phase-modulated single-unit during a theta cycle. **$B_1$** Preferred theta phases of phase modulated single-units. **$B_2$** Averaged histogram of APs fired by all significantly phase-modulated single-units (MEAN in magenta; SEM in black) during a theta cycle. **$C_1$** Left: Autocorrelation of AP firing for a theta-modulated single-unit. Right: FFT of the autocorrelation displaying a peak at ~9 Hz. **$C_2$** Left: Autocorrelation of AP firing for a non-theta-modulated single-unit. Right: FFT of the autocorrelation. **D** Proportion of units being modified in their AP firing. Modulations shown are: positive speed-modulation (pos speed), negative speed-modulation (neg speed), theta-modulation (theta), phase-modulation (phase), and combinations of different modulations.

Positive speed modulated units tended to be modulated more often by theta frequency (n=8 ≡ 5.4 %) or theta phase (n=12 ≡ 8.11 %) than negatively speed-modulated units. Among the latter, only 1 unit (≡ 0.68 %) was firing significantly in theta range and solely 5 units (≡ 3.39 %) presented theta phase-coupled firing.

### 3.5.3. Hippocampal multi-unit activity predicts the onset of locomotion

Movement state specific alignment of hippocampal CA1 multi-unit activity showed up to 5-fold changes in activity over the course of a movement phase (**Figure 32**). In the 400 ms interval prior to the onset phase of locomotion (**Figure 32A$_1$**), an increase in mean firing rates was detected (**Figure 32A$_2$**; n=39, μ=0.0119 [slope], p<0.001). During the following acceleration, multi-unit activity increased further until 700 ms prior to the acc alignment point (**Figure 32B$_1$**). Firing rates started to decrease even though the analysis of the slope in the immediate 400 ms interval preceding the first velocity peak did not point out any significant kinetics (**Figure 32B$_2$**; n=42, μ=-0.0006 [slope], p=0.648). Multi-unit firing rates remained at high rates during the process of running (see **Figure 29**). When the animal started to slow down, mean firing rates peaked approximately 400 ms before the last peak in velocity (**Figure 32C$_1$**). Heterogeneous firing in this interval caused the statistical analysis to show no significant changes in the interval around the dec alignment point (**Figure 32C$_2$**; n=82, μ=-0.003 [slope], p=0.102). Following the deceleration, the animal terminally stopped its movement at $T_0$ in the offset phase (**Figure 32D$_1$**). During this interval, the multi-unit activity was decreasing steadily while the animal slowed down, yet, the slope analysis prior to the alignment point already detected a median slope equal to zero (**Figure 32D$_2$**; n=76, μ=-0.0003 [slope], p=0.592).

### 3.5.4. A small proportion of units in HC CA1 predict upcoming movement states

Individual analysis of hippocampal single-unit kinetics (**Figure 33A**) prior to the detected alignment points (onset, acc, dec, and offset) detected a proportion of units reliably predicting future changes in locomotion.

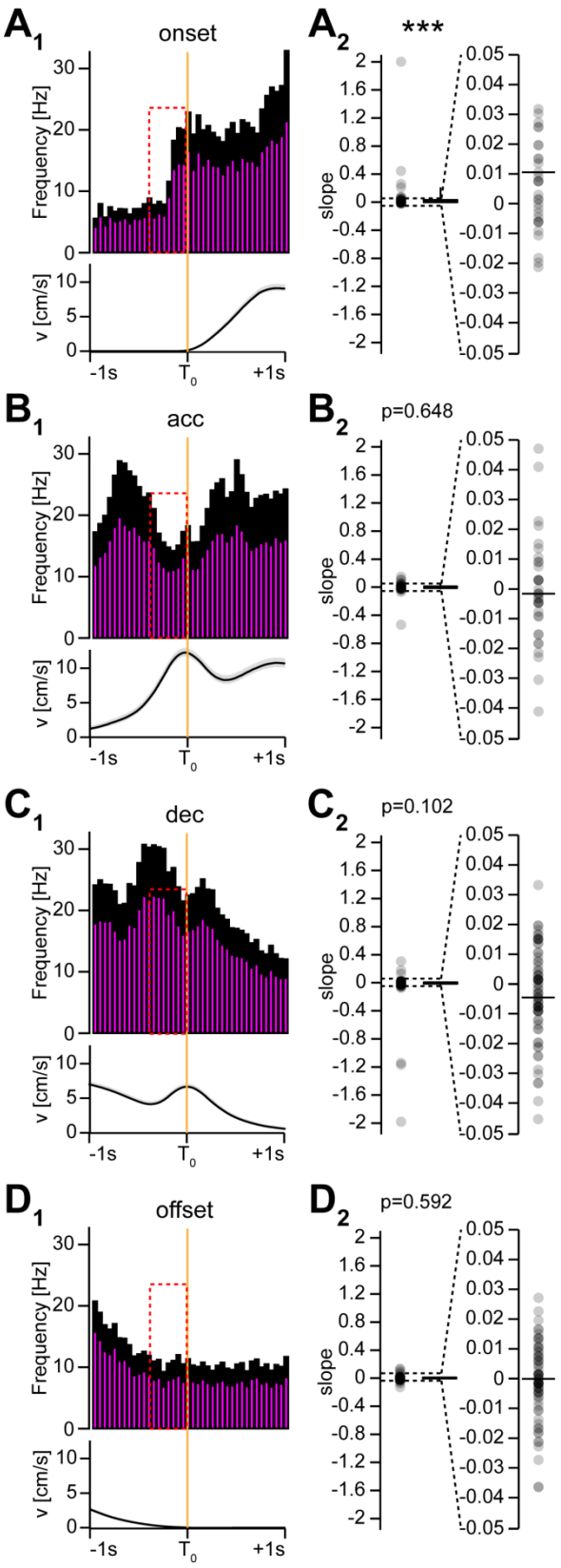


**Figure 32:** Hippocampal multi-unit activity predicts the start of movement

**$A_1$** Top: Averaged 50-ms time bins of HC multi-unit AP frequency (MEAN shown in magenta; SEM shown in black) aligned to the defined *onset* time point at $T_0$ (orange line) and the corresponding velocity shown below (MEAN shown in black; SEM shown in grey). **$A_2$** Median of slopes of the interval indicated by the dashed box on the AP frequency trace with the range close to the median being enlarged; single animal data depicted as circles. **$B_1$**, **$B_2$** same as $A_1$ and $A_2$ for alignment point *end of acceleration* (acc). **$C_1$**, **$C_2$** same as $A_1$ and $A_2$ for alignment point *start of deceleration* (dec). **$D_1$**, **$D_2$** same as $A_1$ and $A_2$ for alignment point *offset of locomotion* (offset).

The predictive unit would either significantly decrease or increase its firing rate before the actual change in locomotion occurs (see chapter 2.4.2). The analysis (**Figure 33B**) revealed that the onset of movement could be reliably predicted by 5/39 units (increase: 4/39 ≡ 10.26 %, decrease: 1/39 ≡ 2.56 %, insignificant: 34/39 ≡ 87.18 %). The end of acceleration could only be predicted by 1/42 units in the HC (increase: 0/42 ≡ 0 %, decrease: 1/42 ≡ 2.38 %, insignificant: 41/42 ≡ 97.62 %), while the start of the deceleration phase was predictively represented in 6/82 units (increase: 1/82 ≡ 1.22 %, decrease: 5/82 ≡ 6.10 %, insignificant: 76/82 ≡ 92.68 %). The termination of locomotion was reliably encoded in 2/76 units (increase: 1/76 ≡ 1.31 %, decrease: 1/76 ≡ 1.31 %, insignificant: 74/76 ≡ 97.38 %). Even though the total amount of cells predicting specific movement phases was low, it was possible to estimate changes in velocity by monitoring single-unit AP firing rates.

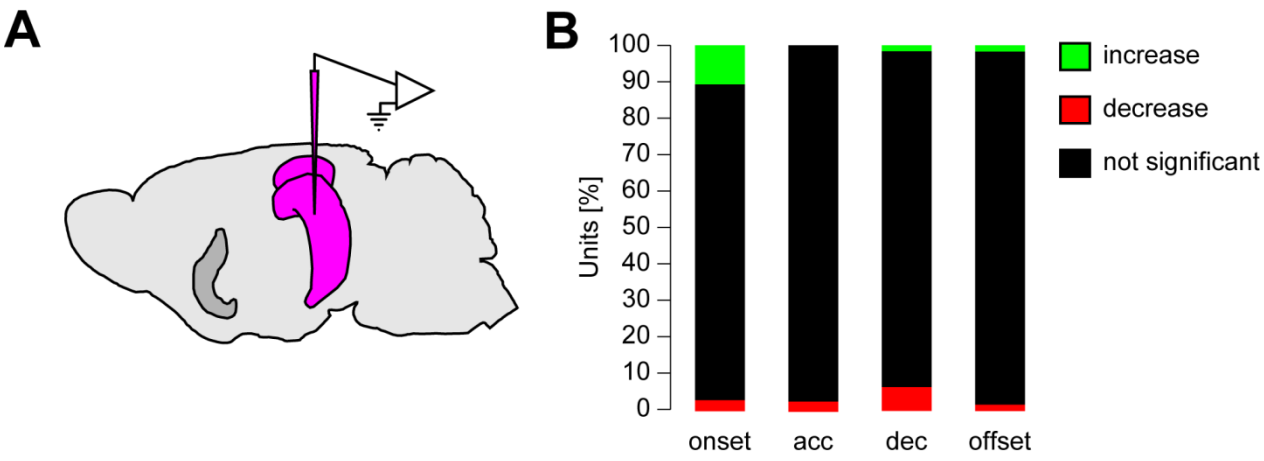


**Figure 33:** Movement state prediction of single-units in hippocampal CA1

**A** Schematic illustration of an acute tetrode recording in the HC. **B** Proportion of units with significantly increasing, significantly decreasing, or insignificant firing rates prior to the alignment points onset, acc, dec, and offset, respectively.

### 3.6. Kinetics of hippocampal theta oscillation's amplitude and peak frequency predictively change prior to the velocity

Representations of locomotion in the oscillatory events occurring in the HC have been described in this work (chapter 3.3). The early increase in theta frequency and amplitude before movement onset suggest a possible prediction of locomotion. To validate these findings, the whole time course of movement had to be taken into account. Complete recording sessions (t>20 min) were used to investigate whether changes seen in the velocity trace are reliably represented in the curves of theta power, theta peak frequency, theta 4-6 Hz band amplitude, theta 7-9 Hz band amplitude, and theta 10-12 Hz band amplitude. The kinetics of locomotion and signal were compared to each other by correlating the binned velocity to the signal and extracting the slope of the linear fit. Similar kinetics would generate larger slopes than diverse kinetics. In the next step the signal trace was shifted by -1000 ms to +1000 ms in 50 ms steps (adding up to 41 steps in total) and correlated to the non-shifted speed of the animal, afterwards. Each time shift yielded an individual correlation that was linearly fitted and the resulting slope was extracted (see chapter 2.4.6). The time shift which generated the largest significant slope (see chapter 2.4.5) displayed the best overlap between signal and velocity. Time shifts between -1000 ms and -50 ms represented signal kinetics that followed behind the changes in velocity, while time shifts larger than zero pointed out that similar kinetics in the signal traces occurred prior to kinetics in the velocity trace. This time shift analysis performed on theta power (**Figure 34A$_1$**) pointed out that the amplitude of theta oscillations between 4-12 Hz predictively took course similar to the velocity trace by approximately 150 ms prior to changes in the velocity of the animal (**Figure 34A$_2$**; n=34, μ=+150 [ms], p=0.034). The predominant frequency of the theta oscillation changed over the course of movement, as presented before (**Figure 23Figure 34B$_1$-B$_4$**). Time shifting of the peak frequency (**Figure 34B$_1$**) revealed that the theta peak frequency kinetics occurred 450 ms before the velocity changes (**Figure 34B$_2$**; n=41, μ=+450 [ms], p=0.025). Based on the variable representation of locomotion in different frequency bands within the range of theta oscillations, slow oscillations between 4-6 Hz, medium oscillations between 6-9 Hz, and high oscillations between 10-12 Hz were time shifted individually (**Figure 34C$_1$**, **D$_1$**, and **E$_1$**).

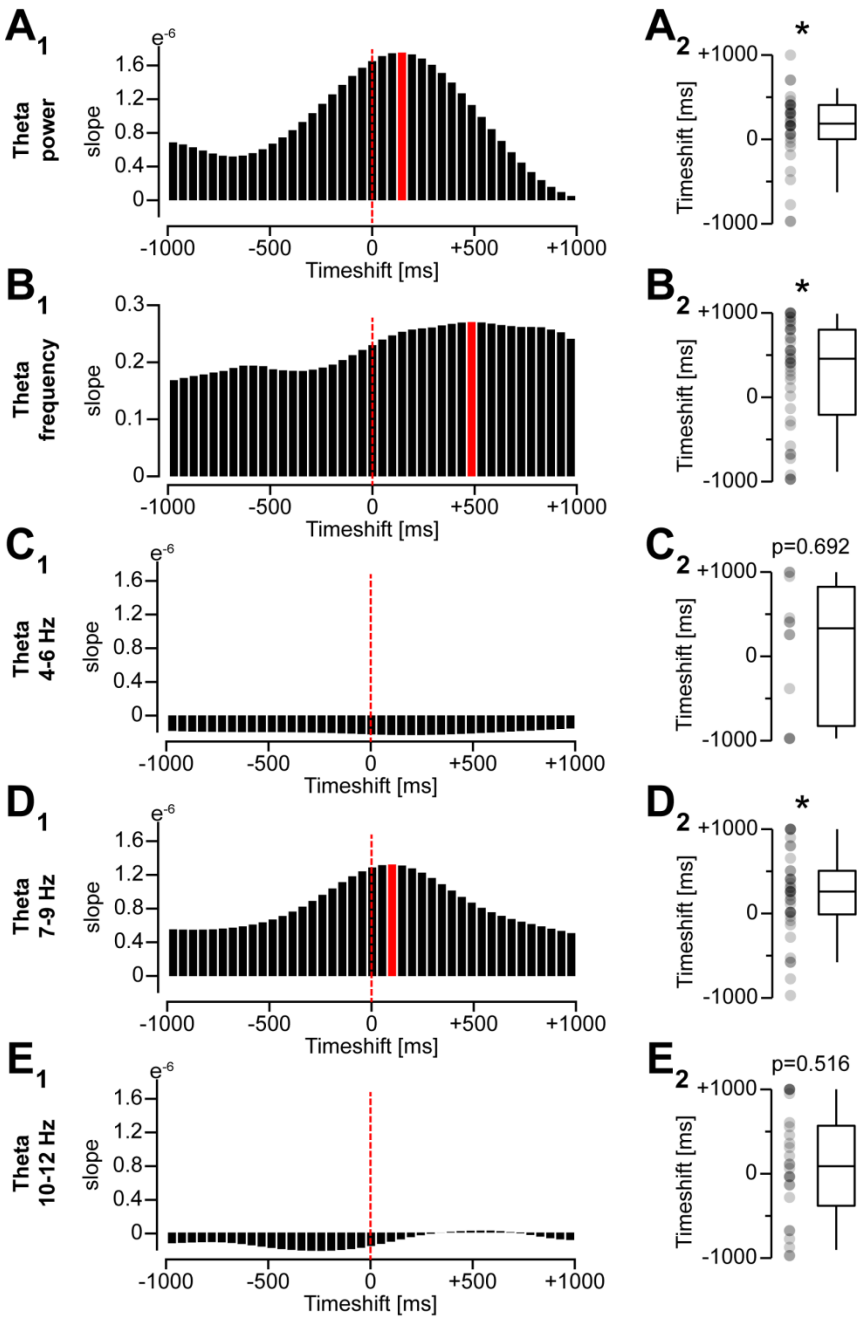


**Figure 34:** Time shift analysis reveals different time points of highest prediction for individual theta bands

**$A_1$** Exemplary result of a time shift analysis showing the slopes of linearly fitted interrelations of time shifted theta power traces and velocity. The red bar marks the time shift that created the largest slope. **$A_2$** Median of time shifts that created the largest and significantly positive slope (red bar in $A_1$) for all animals (n=34). **$B_1$**, **$B_2$** same as $A_1$ and $A_2$ for theta frequency. **$C_1$**, **$C_2$** same as $A_1$ and $A_2$ for theta 4-6 Hz frequency band. **$D_1$**, **$D_2$** same as $A_1$ and $A_2$ for theta 7-9 Hz frequency band. **$E_1$**, **$E_2$** same as $A_1$ and $A_2$ for theta 10-12 Hz frequency band.

The correlation of theta 4-6 Hz amplitude and movement speed generated a significantly positive slope in only 12/41 animals in any of the time shifts. The statistical analysis of the median of these identified best overlaps was indifferent to zero (**Figure 34C$_2$**; n=12, μ=+325 [ms], p=0.692). This indicated that kinetics of theta 4-6 Hz and velocity were the most similar without any time shift. In contrast, mid-frequency theta in the range of 7-9 Hz (**Figure 34D$_1$**) showed an increased overlap of mean amplitude and velocity when the signal was time shifted by +175 ms (**Figure 34D$_2$**; n=37, μ=+175 [ms], p=0.015).This result prove that changes in locomotion were represented in the theta 7-9 Hz band 175 ms before physical movement was executed. The best overlap calculated for the low amplitude theta 10-12 Hz frequency band (**Figure 34E$_1$**) was indifferent to zero (**Figure 34E$_2$**; n=26, μ=-50 [ms], p=0.516).

### 3.7. Locomotion predictively encoded in a subset of neurons in the MS

Previous analyses showed that septal single-unit activity represents locomotion in various ways (see **Figure 25**). Yet, it was still unclear whether single-unit activity could be used to predict upcoming changes in velocity. Focusing on short movement phases (see **Figure 27**) only allows drawing conclusions about the prediction of single phases rather than predicting movement in general. Therefore the time shift analysis was used on unit recordings in the MS (**Figure 35A**). The septal multi-unit activity was time shifted in 50 ms steps by both -1000 ms and +1000 ms to determine the best fit of binned velocity and binned AP firing rates in single-units ($timelag_{max}$). The correlation of velocity and the AP frequency was linearly fitted and the resulting slope of the fit was used as a proxy for the rate of similarity (see chapter 2.4.6). The averaged slopes for every time shift in every unit recorded in the MS was heterogeneously distributed (**Figure 35B**). In order to deal with diverse phenotypes among septal single-units, every unit was analyzed for individual significance with the bootstrap method (see chapter 2.4.5).The approach revealed a subset of units which displayed a significant increase in overlap of AP rate and velocity at time shifts different larger or smaller than zero. Units that showed their best overlap at $timelag_{max}$ values between -1000 ms and -50 ms were considered to follow the changes in the velocity trace and were specified as *follower* units (**Figure 35C**; red circles).

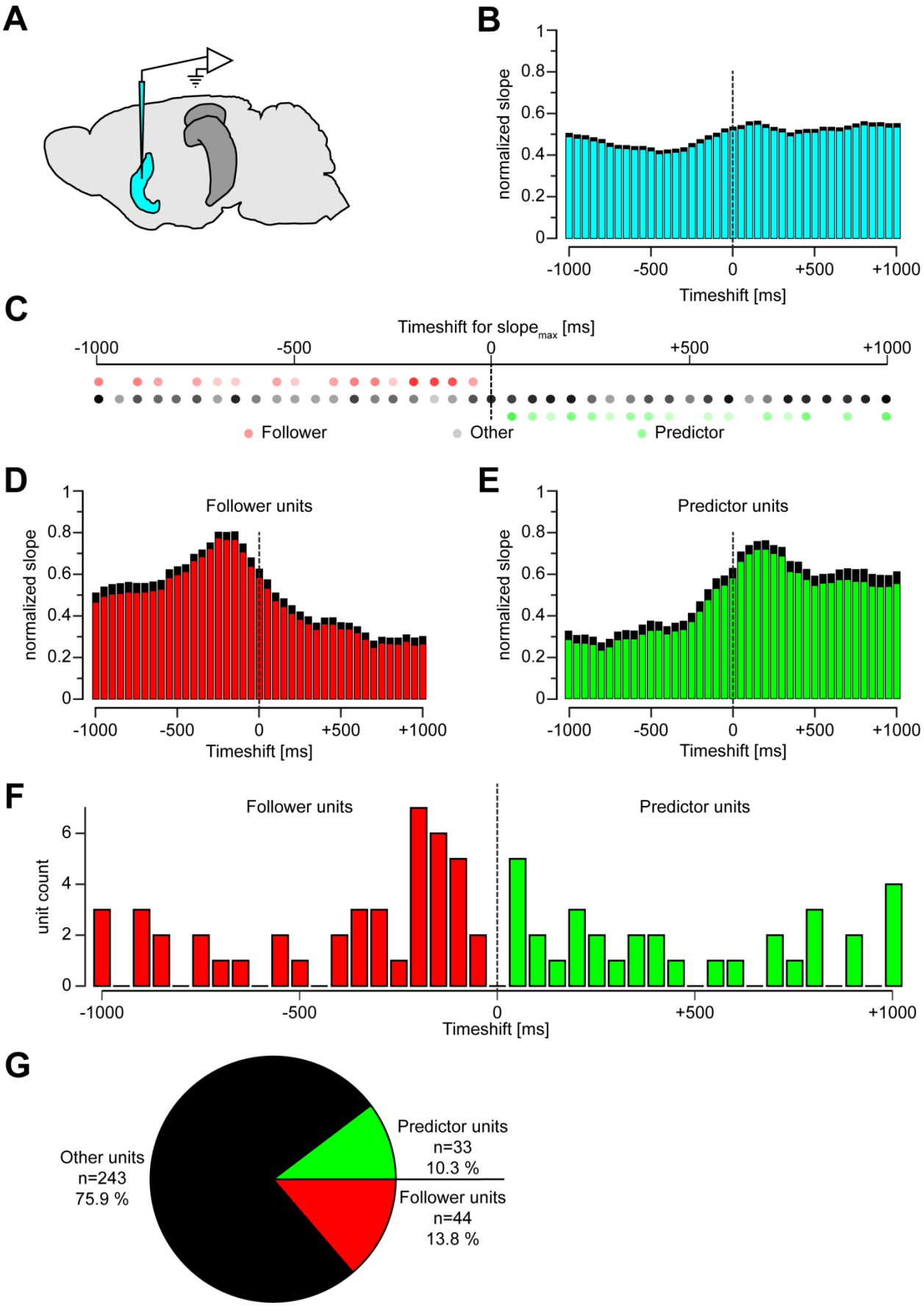
A
B
normalized slope
1
0.8
0.6
0.4
0.2
0
-1000
-500
0
+500
+1000
Timeshift [ms]
C
Timeshift for slope$_{max}$ [ms]
-1000
-500
0
+500
+1000
Follower
Other
Predictor
D
Follower units
normalized slope
Timeshift [ms]
E
Predictor units
normalized slope
Timeshift [ms]
F
Follower units
Predictor units
unit count
6
4
2
0
-1000
-500
0
+500
+1000
Timeshift [ms]
G
Other units
n=243
75.9 %
Predictor units
n=33
10.3 %
Follower units
n=44
13.8 %

**Figure 35:** AP firing rates of septal single-units predict locomotor behavior

**A** Schematic illustration of an acute tetrode recording in the MS. **B** Time shift analysis showing the slopes of linearly fitted correlations of septal multi-unit firing frequency and velocity (MEAN shown in cyan; SEM shown in black). **C** Time shifts of the best overlaps of all single-units recorded in MS. Units were subdivided into follower units (red circles), other units (grey circles), and predictor units (green circles). Follower units were defined as units displaying the best overlap at time shifts < 0 ms; predictor units were defined as units showing the best overlap at time shifts > 0 ms; other units combined all remaining units. **D** Averaged normalized slopes of time shifted follower units (MEAN shown in red; SEM shown in black). **E** Averaged normalized slopes of time shifted predictor units (MEAN shown in green; SEM shown in black). **F** Absolute count of best overlaps at each time shift for both follower (red) and predictor units (green). **G** Proportion of predictor units (green; n=33), follower units (red; n=44), and other units (black; n=243).

On the other side, units that presented their largest slope when at time shifts between +50 ms and +1000 ms were considered predictive to the velocity and therefore termed *predictor* units (**Figure 35C**; green circles). All insignificant units were referred to as *other* units (**Figure 35C**; grey circles). Averaged slopes for the follower and predictor units showed clear peaks in the according time shift direction (**Figure 35D**, **E**). Quantification of every $timelag_{max}$ values calculated for both groups displayed a heterogeneous distribution for the $timelag_{max}$ rather than a uniform clustering (**Figure 35F**). A total amount of 320 units was analyzed (**Figure 35G**), revealing 33/320 predictor units (≡ 10.3 %), identifying 44/320 follower units (≡ 13.8 %), and tagging 243/320 other units (≡ 75.9 %).

### 3.8. Predictability of locomotion on the basis of single-unit activity in HC CA1

Multi-unit recordings of neurons in the pyramidal cell layer of the HC were processed using the time shift analysis (**Figure 36A**). This approach should reveal whether HC units that change their firing rate in accordance to changes in velocity present this behavior either already before movement or after, or whether they are entirely unaffected by locomotion. As previously done on MS units, the AP time points of HC units were time shifted in 50 ms steps by -1000 ms up to +1000 ms, each step yielding a slope of the linear fit of the correlation between firing rates and the animal's movement speed.

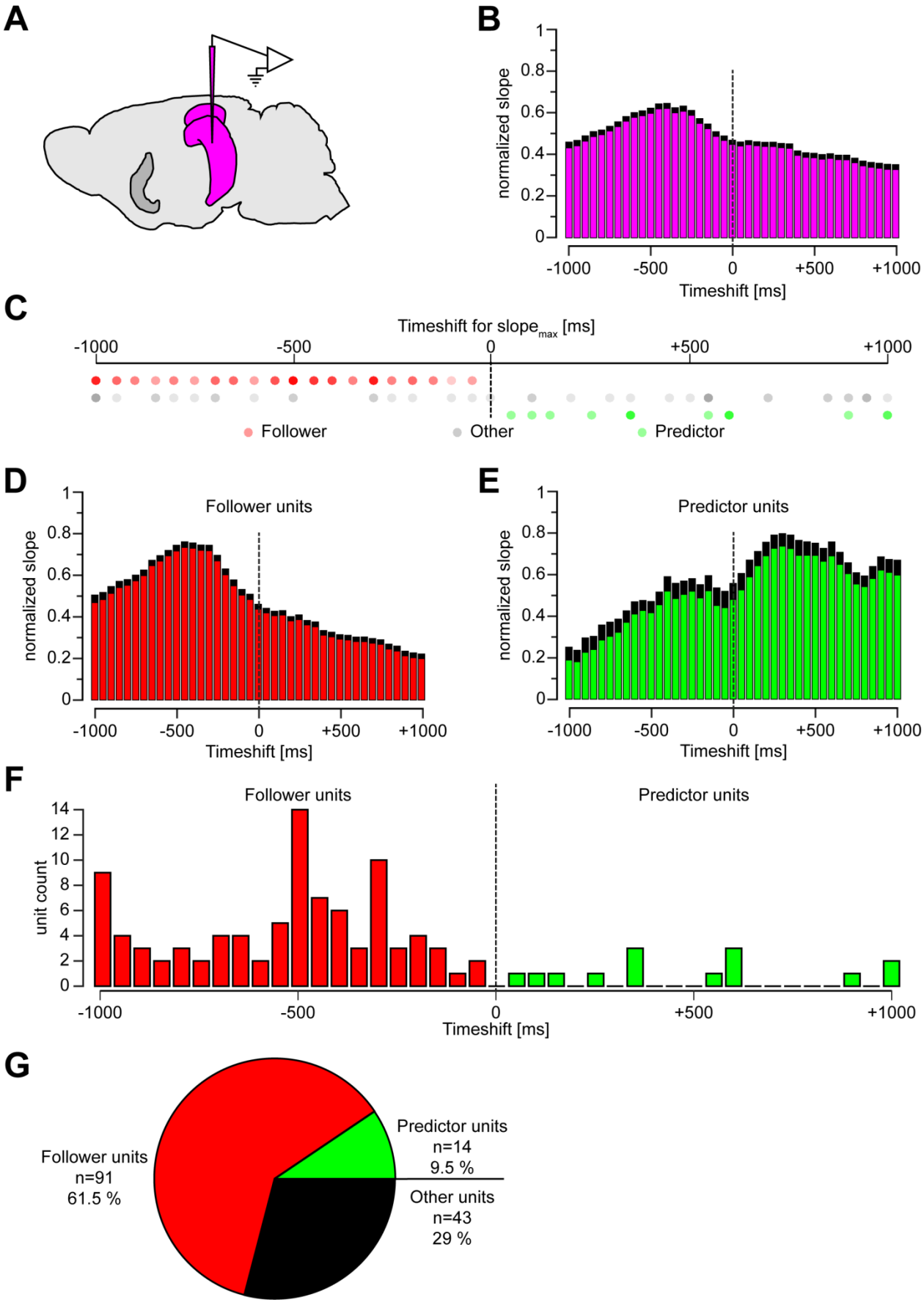
A
B
normalized slope
Timeshift [ms]
C
Timeshift for slope$_{max}$ [ms]
Follower
Other
Predictor
D
Follower units
E
Predictor units
F
unit count
G
Follower units
n=91
61.5 %
Predictor units
n=14
9.5 %
Other units
n=43
29 %

**Figure 36:** AP firing rates of hippocampal single-units reliably predict locomotion

**A** Schematic illustration of an acute tetrode recording in the MS. **B** Time shift analysis showing the slopes of linearly fitted correlations of hippocampal multi-unit firing frequency and velocity (MEAN shown in magenta; SEM shown in black). **C** Time shifts of the best overlaps of all single-units recorded in MS. Units were subdivided into follower units (red circles), other units (grey circles), and predictor units (green circles). Follower units were defined as units displaying the best overlap at time shifts < 0 ms; predictor units were defined as units showing the best overlap at time shifts > 0 ms; other units combined all remaining units. **D** Averaged normalized slopes of time shifted follower units (MEAN shown in red; SEM shown in black). **E** Averaged normalized slopes of time shifted predictor units (MEAN shown in green; SEM shown in black). **F** Absolute count of best overlaps at each time shift for both follower (red) and predictor units (green). **G** Proportion of predictor units (green; n=14), follower units (red; n=91), and other units (black; n=43).

The averaged slopes of the whole population of HC units displayed a peak after being shifted by -400 ms (**Figure 36B**). Yet, individual analysis for randomness in this dataset identified significant follower units, significant predictor units, and an insignificant rest of units (**Figure 36C**). The averaged time shift analyses of follower units confirmed the finding on the population level with its peak at -400 ms (**Figure 36D**). In contrast, the cohort of predictor units displayed the largest slopes when shifted between +50 ms up to +1000 ms, peaking at 300 ms (**Figure 36E**). The $timelag_{max}$ values of the identified follower units were ambiguously distributed along the range of negative time shifts while the majority of units showed the best overlap between -250 ms and -500 ms (**Figure 36F**; red bars). $Timelag_{max}$ values of identified predictor units were scattered between +50 ms and +1000 ms without accumulating at any time shift step (**Figure 36F**; green bars). The total amount of 14/148 predictor units (≡ 9.5 %) was relatively low compared to the majority of 91/148 follower units (≡ 61.5 %) and 43/148 indiscriminate units (≡ 29 %; **Figure 36G**).

# 4. Discussion

To understand how neuronal processing of incoming sensory information may be adapted to different locomotion velocities is crucial. Many previous studies addressed the neuronal representation of movement in general, comparing immobility versus locomotion (Vanderwolf, 1969; Wyble et al., 2004; Hinman et al., 2016). To investigate these distinct conditions and their neuronal activation patterns is an important first step to understand all that happens in the brain during movement. Yet, real movement is much more complex and goes beyond binary resting and locomotion states.

The present study investigates the physiological processes that are involved in the brain-state transition from immobility to locomotion. It confirms existing models on movement initiation involving the MS-HC network (Oddie and Bland, 1998; Fuhrmann et al., 2015) and adds significant insights on both population and single-unit level of septal and hippocampal neurons. This work extends previous approaches by investigating physiological brain activity during a well-defined locomotor behavior on a linear treadmill.

The central results of this work are the following:

**(1)** MS VGluT2$^{+}$ and PV$^{+}$ neuron populations are positively speed-modulated and increase their activity prior to locomotion onset.

**(2)** HC CA1 theta oscillations' amplitude and peak frequency are positively speed-modulated and begin to increase before the start of movement.

**(3)** MS and HC action potential firing rates are increased during locomotion with distinct populations showing firing patterns that reliably predict future locomotion.

## 4.1. Movement associated activity in the MS

The MS is positioned centrally in the basal forebrain and holds a key function in connecting behaviorally relevant brain regions and relaying signals (Petsche et al., 1962). The intraseptal micro circuitry contains a strongly interconnected local network which contains glutamatergic, cholinergic, and GABAergic neurons (Kiss et al., 1990; Gritti et al., 1993; Kiss et al., 1997; Gritti et al., 2003; Hajszan et al., 2004; Halasy et al., 2004). The distribution patterns of these cells (**Figure 3C**) and the unique electrophysiological properties enable a versatile range of neuronal output (Sotty et al., 2003; Manseau et al., 2005) that is highly increased during movement (Petsche et al., 1962; Morris and Hagan, 1983; Fuhrmann et al., 2015; Justus et al., 2017). The existence of glutamatergic neurons in the MS has been demonstrated previously (Kohler et al., 1984). Yet, research mostly focused on other cell types as VGluT2$^+$ cells constitute the smallest population within the septal area (Colom et al., 2005). These cells recently gained more attention since recent studies revealed a direct connection between VGluT2$^+$ neurons and locomotion in animals (Bender et al., 2015; Fuhrmann et al., 2015; Kropff et al., 2015; Justus et al., 2017).

### 4.1.1. Population activity of VGluT2$^+$ and PV$^+$ neurons in the MS display a movement related increase in activity

In this study I find an increase of MS VGluT2$^+$ neuronal activity before and during episodes of locomotion, using fiberoptometric monitoring of population calcium signals (**Figure 14**, **Figure 15**, **Figure 16**). The data confirm the results of *Fuhrmann et al., 2015* who used similar methods and analyses. The physiological relevance of MS VGluT2$^+$ activity during locomotion is demonstrated by showing that these cells are recruited during voluntary movement initiation. It was investigated in higher detail than was done in previous studies. This approach of temporal dissection was important to understand that VGluT2$^+$ activity specifically changes over the course of locomotion. In detail, this activity indicates transitions from one movement state to the next one rather than a linear increase or decrease once movement was initiated. The present work demonstrates that while acceleration is still ongoing, VGluT2$^+$ activity already ceases to increase (**Figure 16B$_1$**). Similarly, activity starts to decrease before the final deceleration takes place

(**Figure 16C$_1$**). This temporal recruitment pattern was previously unknown. It suggests that glutamatergic cells in the MS are involved in relaying signals about future movements.

With the link between septal VGluT2$^+$ activity and locomotion confirmed, the mechanism mediating this correlation still remains not fully resolved. Experiments involving optogenetic stimulation of VGluT2$^+$ neurons in the MS reliably initiated movement and evoked theta oscillations in the HC depending on the stimulation frequency (Fuhrmann et al., 2015; Robinson et al., 2016). However, optogenetic activation of VGluT2$^+$ axons leaving the MS via the fornix (projecting into the HC) was insufficient to modulate theta oscillation in hippocampal CA1 (Robinson et al., 2016). The disruption of the glutamatergic network in the MS by local administration of NMDA receptor blocker prolonged stimulated movement but impaired theta oscillation generation and uncoupled theta oscillations from movement speed (Fuhrmann et al., 2015). Moreover, disrupting MS activity by micro infusion of pharmacological compounds or lesioning of the MS region strongly reduced theta while an effect on the behavioral performance is not clear yet (Leutgeb and Mizumori, 1999; Koenig et al., 2011; Wang et al., 2015). These findings suggest that the intraseptal glutamatergic network rather than VGluT2$^+$ septal-hippocampal projections are essential for hippocampal theta entrainment. Together, these studies indicate that the HC might play a minor role for movement initiation and are not in full agreement to the recent publication of *Bender et al., 2015*. By using optogenetic control of the MS-HC in order to control theta oscillations, Bender and colleagues were able to narrow the range of velocities an animal would run, yet, the likelihood of movement initiation was unaffected. Lesioning of the HCF in rats by infusion of excitotoxic compounds into the hippocampal and parahippocampal regions left locomotion behavior unaltered (Kim and Frank, 2009). Moreover, human studies involving the bilateral ablation of the HCF as in the case of patient H.M. did not describe any motor phenotype (Scoville and Milner, 1957; Penfield and Milner, 1958).

VGluT2$^+$ neurons are highly important for the network activity within the MS. Immunohistochemical studies showed that the major proportion of septal VGluT2$^+$ axons remain locally in the MSDB and terminate on PV$^+$ neurons (Hajszan et al., 2004). VGluT2$^+$ synapses could be detected on septal ChAT$^+$ and other VGluT2$^+$ neurons (Manseau et al., 2005). Septal VGluT2$^+$ neurons and PV$^+$ interneurons are reciprocally connected,

while only few ChAT$^+$ synapses could be detected on other neurons in the MS (Manseau et al., 2005; Fuhrmann et al., 2015). This indicates that the intraseptal network is primarily driven by glutamatergic excitation mediated by VGluT2$^+$ cells. Yet, glutamatergic neurons in the MS contribute to the septal output and provide ~4-23 % of the septal-hippocampal projections (Colom et al., 2005). They project on both principal pyramidal neurons and interneurons in the HC (Huh et al., 2010; Sun et al., 2014) thereby influencing the local network activity in CA1 (Petsche et al., 1962; Mysin et al., 2015). This glutamatergic input was shown to rather lead to modulation than generation of theta oscillation (Buzsaki et al., 1980; Fuhrmann et al., 2015; Robinson et al., 2016). PV$^+$ neurons in the MS, however, are indispensable for controlling the local field activity in the hippocampal CA1 region (Freund and Antal, 1988; Oddie and Bland, 1998; Leutgeb and Mizumori, 1999; Mysin et al., 2015). GABAergic cells constitute the major part of neurons in the MS (Gritti et al., 1993; Gritti et al., 2003) and are known to induce rhythmic activity patterns in the HC by evoking local disinhibition (Freund and Antal, 1988; Li et al., 2014). Moreover, PV$^+$ neurons efficiently drive theta oscillations and stimulation of septal PV$^+$ axons in the dorsal HC is sufficient to control theta frequency and power (Bender et al., 2015). They evoke inhibition in CA1 interneurons, but monosynaptic connectivity onto pyramidal cells has also been described (Sun et al., 2014).

The present study provides evidence for a specific pre-movement activation of PV$^+$ neurons in the MS similar to the activity of MS VGluT2$^+$ neurons (**Figure 17**). These GABAergic interneurons displayed increased GCaMP5G transients prior to the onset of movement and maintained high levels of activity during locomotion, which increased corresponding to the velocity (**Figure 18**). The movement phase specific alignment of GCaMP5G transients emitted by PV$^+$ cells revealed an early onset of activity (**Figure 19A$_1$**). The experiments also showed that GCaMP5G transients were no longer linearly increasing prior to the endpoint of acceleration (**Figure 19B$_1$**). The termination phase around the offset alignment point showed significantly decreasing kinetics, but it remains unclear whether this decrease was corresponding to the state of immobility or rather correlated to an earlier time point during deceleration (**Figure 19D$_1$**). In general, GCaMP5G time courses of VGluT2$^+$ and PV$^+$ neurons were comparable. However, visualizing inactivation using GCaMP5G suffers from reduced temporal resolution due to

comparatively slow fluorescence decay kinetics. Also, $PV^+$ neurons in the MS tend to fire at high frequencies (Morris et al., 1999). Resolving such activity with $Ca^{2+}$-dependent fluorescent proteins is challenging due to these slow off-kinetics (Akerboom et al., 2012; Akerboom et al., 2013). Considering this, the interpretation of the time course during the deceleration phase and the offset phase should be treated with some caution. On the other hand, the increasing activity during the onset interval and the acceleration interval can be reliably visualized with GCaMP5G.

MS $PV^+$ neurons are strongly excited by the intraseptal network (Colom et al., 2005; Manseau et al., 2005; Mysin et al., 2015). That may explain the co-activation during running episodes. However, once the glutamatergic transmission within the MS micro network is disrupted, theta oscillations break down and cannot be maintained (Fuhrmann et al., 2015), elucidating that $VGluT2^+$ neurons may not be the generators of hippocampal theta oscillations (Buzsaki et al., 1980). Yet, glutamatergic cells in the MS drive septal $PV^+$ neurons which are shown to be strong theta inducers (Li et al., 2014; Sun et al., 2014; Mysin et al., 2015). Under physiological conditions, both cell types are simultaneously active. Blocking the intraseptal glutamatergic excitation of $PV^+$ neurons impaired theta oscillations in the HC likely due to reduced activity of the theta generators (Fuhrmann et al., 2015). Accounting for the intraseptal connectivity, similar kinetics of the excitatory $VGluT2^+$ and inhibitory $PV^+$ neurons are therefore necessary.

The results of Fuhrmann and colleagues indicate that the onset of locomotion is directly linked to the activity of neurons in the MS. Indeed, the initiation of movements after indifferent septal $VGluT2^+$ stimulation might be an effect of distinct MS efferents (Fuhrmann et al., 2015). Yet, it is unlikely that these finding are mediated by HC projecting $VGluT2^+$ neurons in the MS. Instead, glutamatergic projections leaving the MSDB via the fimbria are promising candidates for the observed locomotor control (Buzsaki et al., 1980). Evidence supporting this hypothesis is given by a study which describes motor impairments after performing a lesion of the fimbria/fornix output of the MS (Morris and Hagan, 1983). As the fornix stimulation of MS glutamatergic projections was unable to reliably initiate a movement (Fuhrmann et al., 2015; Robinson et al., 2016), movement induction is likely dependent on the fimbric efferents. A similar stimulation of septal $PV^+$ fibers in the hippocampal CA1 region did not increase the probability of locomotion onsets

(Bender et al., 2015). Furthermore, intraseptal optogenetic activation of GABAergic neurons left locomotion unaltered (Sweeney and Yang, 2016), providing more evidence for a septal VGluT2$^+$ activity which is involved in the initiation of locomotion via fimbric efferents.

### 4.1.2. Unit activity in the MS is heterogeneous during locomotion

The electrophysiological changes in neuronal activity in the MS were monitored to evaluate single-cell activity. By performing septal recordings using electrode arrays, the time resolution with which neuronal activity was monitored could be drastically increased while cells could no longer be differentiated based on their genetic properties.

In general, the findings that VGluT2$^+$ and PV$^+$ neurons in the MS are both activated during running episodes could be confirmed by the multi-unit data acquired with tetrodes. The majority of recorded septal units were significantly more active when the animals moved (**Figure 24**), which is in accordance to the findings in *Fuhrmann et al., 2015*. Furthermore, AP frequency was positively correlated to the velocity (**Figure 25**). *Justus et al., 2017* showed that these so called *speed-cells* in the MS carry the information about the current velocity and project onto speed-cells in the medial entorhinal cortex (Kropff et al., 2015; Justus et al., 2017). My data points out that these mechanisms were not applicable to every neuron in the MS, as some cells reduced their AP firing rate during locomotion. Also, subsets of units were shown to be either negatively correlated to the speed of the animal or unaffected by locomotion. These versatile firing phenotypes agree with the idea that the MS is not passively encoding movement speeds, and imply a septal involvement in other tasks than speed-encoding, e.g. spatial learning or exhibition of trained behaviors (Henderson and Greene, 1977).

Deeper investigation of modulations affecting neuronal firing of cells in the MS revealed prominent phase coupling to hippocampal theta oscillations (**Figure 26**). A strong coupling of septal neurons to the phase of theta would be expected for neurons which generate theta oscillations in the downstream HC. In regard of an efficient control of theta oscillation, PV$^+$ cells have been described to lock their firing to distinct phases of HC theta waves (King et al., 1998; Borhegyi et al., 2004). In addition, a population of units showed

a preference to fire at frequencies in the range of theta. Interestingly, a set of cells preferentially fired at theta frequency even though uncoupled from hippocampal theta. These cells may project onto targets different than the HC and control rhythmic activity in other parts of brain. In-vivo intracellular recordings in the MSDB previously described three types of neurons with respect to their relationship to hippocampal theta phases and intracellular theta rhythms, being in line with the presented results (Barrenechea et al., 1995). The combination of positive speed-modulation and either theta-modulation or phase-modulation was more abundant than the combination of negative speed-modulation and theta-modulation or phase-modulation (**Figure 26**). This coherence strengthens the interpretation that the hippocampal transition into an activity-state for enhanced computation of sensory input (activation of theta) during locomotion is mediated by neurons in the MS (Fuhrmann et al., 2015).

The movement phase specific analysis of AP firing of septal neurons yielded heterogeneous results. The alignment of AP frequencies units in the MS to the onset of locomotion showed no clear increase in firing rate prior to the alignment point (**Figure 27**). This does not agree with the findings of the GCaMP5G experiments. It can be explained by highly diverse and heterogeneous firing patterns of glutamatergic cells in the MS, which was uncovered by electrophysiological studies in brain slices: AP firing ranges from slow and clustered-firing (Sotty et al., 2003; Manseau et al., 2005) to fast-firing with prominent $I_h$ currents and rhythmic spontaneous AP frequencies in theta range, which is comparable to septal GABAergic neurons (Huh et al., 2010). In accordance to the clear increase of AP frequency from resting to running, the population of MS neurons indeed increased their firing around movement onset and maintained this elevated activity level. Though AP frequencies remained stable over the course of the movement interval, the offset of locomotion was accompanied by an explicit drop in firing rate (**Figure 27D$_1$**). These heterogeneous firing patterns are not surprising, considering that only a fraction of cells in the MS is involved in the representation of locomotion while the rest is more responsive to other sensory stimuli (Kaifosh et al., 2013). Yet again, my work points out that a population of septal units was able to predict individual movement states (**Figure 28**), implying that the information on upcoming changes in locomotion is contained in the AP firing of a few cells within the MS micro network.

## 4.2. Movement associated activity in the hippocampal CA1 region

Sensory information of multiple sources is processed within the HC (Knierim et al., 2006). A prominent proportion of excitatory and inhibitory inputs into the HC originate from the MS (Agster and Burwell, 2013). These afferents control and regulate both the amplitude and the frequency of the oscillatory activity (Leung, 1998; Buzsaki, 2002). Inhibition of theta mostly goes along with severe impairments in spatial memory and orientation (Leutgeb and Mizumori, 1999; Hasselmo et al., 2002b; Koenig et al., 2011).

### 4.2.1. HC CA1 theta amplitude and peak frequency increase during running

Various studies on rhythmic activity in the HC investigated the connection between theta and movement. Early findings could show that the distinct behavioral states of wakefulness, sleep, and arousal are encoded in the hippocampal electrical activity (Green and Arduini, 1953; Vanderwolf and Heron, 1964). Further work on the HC pointed out that voluntary movements like locomotion and jumping are preceded and accompanied by trains of rhythmical activity in the HC (Vanderwolf, 1969; Whishaw and Vanderwolf, 1973).

My experiments are in agreement with these studies. They show an increase in both frequency and amplitude of theta during voluntary locomotion (**Figure 20**). The detailed analysis of frequency bands revealed that this observation is mainly caused by an increased power of frequencies between 7-9 Hz and a lowered abundance of 4-6 Hz oscillations, while frequencies faster than 10 Hz were generally low in amplitude and seemingly unaffected by movement (**Figure 21**). Intermediate frequencies (6-7 Hz and 9-10 Hz) were neither increased nor decreased during locomotion compared to rest, thereby these frequencies sharpened the contrast between the three frequency bands defined in the analysis. Interestingly, the movement associated range of theta between 7-9 Hz increased its amplitude in a similar magnitude as theta 4-6 Hz was decreased (**Figure 21**). Faster oscillations were also decreased, yet, the relative change was less for theta 10-12 Hz. Pharmacological experiments blocking muscarinic receptors identified frequencies within theta range which reacted differently to compound infusion, indicating that different frequencies are generated by independent sources (Kramis et al., 1975). These results are in accordance to experiments that indicated velocity-dependent

modulation of theta. By directly correlating movement speed to the frequency or the amplitude of hippocampal theta, a positive correlation to the motor behavior could be shown (Rivas et al., 1996; Oddie and Bland, 1998). In fact, this work shows that theta amplitude and peak frequency are positively correlated to the speed of an animal (**Figure 22**). Furthermore, separating theta into the previously described classes pointed out that this positive relation is based on the emerging prominence of theta 7-9 Hz (**Figure 22D$_1$**). These results fit into the functional understanding of the MS-HC network which increases its general activity during locomotion. This model implies direct control of theta oscillations by PV$^+$ neurons in the MS which in turn are primarily driven by the glutamatergic activation of MS VGluT2$^+$ cells (Freund and Antal, 1988; Manseau et al., 2005; Huh et al., 2010; Bender et al., 2015). The results presented in this work suggest a functional coupling of septal VGluT2$^+$, septal PV$^+$, and hippocampal theta oscillations which is supported by an observed synaptic coupling of MS and HC (Freund and Antal, 1988; Buzsaki, 2002; Manseau et al., 2005).

The switch from a behavioral state that is independent of theta oscillations to a theta-associated state has been intensively investigated. An alignment of theta power to the onset/offset of a movement showed an early increase in power, representing the transition from a non-theta state to a theta-state, or vice versa (Vanderwolf, 1969; Wyble et al., 2004). The method presented in this work verified a power increase in the 7-9 Hz frequency band prior to locomotion onset by means of statistics (**Figure 23D$_1$**). The early increase in theta peak frequency and amplitude is in accordance to the increased activity of septal PV$^+$ neurons before movement initiation. The kinetics observed for theta 7-9 Hz around the acceleration endpoint well resembled the observations in the GCaMP5G transients of VGluT2$^+$ and PV$^+$ neurons in the MS. Furthermore, the amplitude of the theta frequency band between 7-9 Hz was reduced to baseline level before the movement was completely terminated (**Figure 23D$_1$**). The functional connection between neurons in the MS and theta oscillation in the HC implies that HC projecting VGluT2$^+$ and PV$^+$ neurons most probably reduced their firing rates back to baseline before locomotion offset, too. Yet, this hypothesis could not be verified by the experiments presented in the current study.

The early shift from slow frequencies to higher frequencies during movement is in accordance to the other studies (Vanderwolf, 1969; Wyble et al., 2004). Initial studies in rats defined hippocampal theta as rhythmic activity between 4-12 Hz (Vanderwolf, 1969; Whishaw and Vanderwolf, 1971; Bland and Vanderwolf, 1972; Kramis et al., 1975). Yet, the analysis of the theta band from 10-12 Hz could not detect any characteristic changes for these frequencies, despite a decrease in mean amplitude during running (**Figure 21K**, **Figure 23**).

### 4.2.2. Hippocampal units are diversely activated during locomotion

In order to describe the locomotion dependent activity changes in the hippocampal CA1 region it was necessary to monitor the activity of individual neurons. This requirement was met by recording AP firing of multiple cells with an electrode array acutely placed into CA1 s.p. Experiments that involved tetrode recordings in the HC of behaving animals suggested that running speed can affect neuronal firing (O'Keefe and Conway, 1978). The presented work confirms that the population of hippocampal neurons significantly increases its firing rate from resting to running (**Figure 29**). This elevated baseline activity enabled neurons with spike rate modulation as a possible way to transfer information (Heck et al., 2013; Pfeiffer and French, 2015). The alteration of hippocampal activity is most likely caused by medial septal neurons, either by disinhibiting CA1 pyramidal cells via GABAergic projection onto hippocampal interneurons or by direct excitatory connection onto hippocampal interneurons (Roland et al., 2014; Robinson et al., 2016). Yet, this adaption to movement was not applicable to every recorded unit. Studies in guinea pigs showed that neuronal firing in the HC is increased linearly in accordance to the running speed (Rivas et al., 1996). This finding fits to the results presented in this work (**Figure 30**). One population of hippocampal units was indeed positively correlated to movement speed, a second population was unaffected by the velocity, and a third population decreased its firing rate with increasing running speed (**Figure 30$F_1$-$F_3$**). The latter group (anti-speed cells) has been described in the medial EC but these cells were more than 40 % less abundant than positively speed-correlated neurons and the functional relevance remains unresolved (Kropff et al., 2015). Still, anti-speed cells also switched from slow baseline-firing to elevated movement associated baseline-firing which

was then reduced in order to encode movement. This initial shift to higher baseline firing is necessary as principal neurons in HC CA1 tend to display very slow AP firing rates below 1 Hz during (Mizuseki et al., 2011).

Apart from speed-modulation, a group of units showed significant theta-phase modulation. These cells preferentially fired during the rising phase of the theta cycle (**Figure 31**). AP coupling to distinct phases of theta oscillations was described to be crucial for place cell formation in hippocampal CA1 (Losonczy et al., 2010). Moreover, a smaller proportion of neurons preferred firing at frequencies between 4-12 Hz. Yet, only half of these cells were coupled to the recorded theta in the contralateral HC (**Figure 31D**). The remaining neurons fired incoherenlyt to the theta oscillations recorded from the contralateral hemisphere. It is unlikely that these theta-uncoupled cells are part of the intrahippocampal theta oscillator, so their physiological role remains unresolved (Holsheimer et al., 1982; Buzsaki, 2002). Possibly, these cells constitute an extra-regional theta oscillator for a downstream area, but up to now, there is no evidence for this. A small fraction of cells displayed rhythmic firing above 12 Hz and exceeded the theta range. These *anti-theta* cells stayed silent during theta oscillations but switched to rhythmic firing at 15-25 Hz in the absence of theta related oscillatory activity (Buzsaki et al., 1983; Mizumori et al., 1990). Rhythmic activity in the HC occurs mainly during periods of locomotion causing anti-theta cells to be primarily active while the animal remains immobile (Green and Arduini, 1953; Vanderwolf and Heron, 1964). Increased activity of hippocampal neurons during theta unrelated behavior was rarely seen and the function has yet to be determined (Mizumori et al., 1990). Comparable to neuronal modulation in the MS, the presented hippocampal speed-cells in this study were more often theta-modulated than anti-speed cells (**Figure 31D**). This is in agreement to the positive speed-correlation of theta peak frequency (**Figure 22**), as increased oscillation frequencies cause faster firing rates in neurons coupled to the local field activity. Plus, it has been shown that pyramidal cells in the HC couple their firing to the negative phase of theta (Holsheimer et al., 1982). This indicates that at least a fraction of units is required to display positive speed-modulation as well as phase-modulation. Otherwise, such firing patterns would counteract and diminish theta, which would most probably result in a decreased ability of retrospection (Leutgeb and Mizumori, 1999).

The alignment of septal multi-unit activity depicted elevated neuronal activity during locomotion (**Figure 27**), but was mostly constant during distinct movement states and thereby differed from the findings of the GCaMP5G recordings (**Figure 16**, **Figure 19**). Still, individual units could be identified which predicted reliably upcoming changes in locomotion (**Figure 28**). Assuming a massive synaptic coupling of hippocampal neurons by septal neurons, only few cells in the MS would be sufficient to evoke the observed theta kinetics over the course of locomotion intervals. In fact, the results of the alignment of hippocampal multi-unit activity to the start of movement showed a strong increase in unit activity prior to the onset (**Figure 32A$_1$**). This fast rise in multi-unit activity was followed by a further increase in AP frequency. The end of acceleration was preceded and followed by activity peaks, and similarly the start of deceleration was flanked by peaking AP firing rates (**Figure 32B$_1$**, **C$_1$**). The termination of movement was clearly indicated by the strongly decreasing multi-unit activity more than 400 ms before the animal terminally stopped (**Figure 32D$_1$**). The presented kinetics differs in part from the alignment traces shown for theta recorded in the contralateral HC CA1 region. This discrepancy points out, that the LFP must not to be mistaken as a proxy for neuronal firing. Theta oscillations reflect the inputs entering a local field which contains theta cells, theta-unassociated cells, and anti-theta cells rather than representing the firing of local neurons (Mizumori et al., 1990). The activity patterns of pyramidal cells in the HC have been described to be highly diverse and originate from a highly diverse intrahippocampal network with a multitude of interneuron types (Alger and Nicoll, 1982; Freund and Buzsaki, 1996; Müller and Remy, 2014). The peaks in activity close to the alignment points in the acc and the dec interval could represent these diverse firing patterns of hippocampal neurons (**Figure 32B$_1$**, **C$_1$**). A subset of cells increased its firing rate in accordance to the described kinetics of theta, while another population of cells displayed similar changes ~1 s later. This delay in elevated activity could represent a replay of ongoing internal activity dynamics, as described in studies investigating reoccurring sequences of hippocampal pyramidal cell firing during episodes of running (Malvache et al., 2016). Still, the investigation of single-unit AP firing prior to the aligned movement phases revealed that both the onset and the start of deceleration were most reliably predicted by single-units (**Figure 33**). The end of acceleration and the offset of locomotion could be predicted by only few single-units. My analysis used a time-window of 400 ms prior to an alignment point to evaluate AP firing

rates and thereby did not allow for any specific activity pattern that occurred before the interval. Therefore, the identified cells displayed highly conserved activity patterns during each respective movement phase.

### 4.3. Predictive encoding of locomotion

The activity patterns in the MS-HC network are strongly correlated to the current locomotor behavior. Analyzing the slope in a 400 ms interval before an upcoming onset of movement revealed an increase in activity in both septal VGluT2$^+$ and PV$^+$ neurons, as well as in amplitude of the theta frequency band 7-9 Hz (**Figure 16**, **Figure 19**, **Figure 23**). On the level of multi-units, an increase in septal firing rates corresponding to the increase in the GCaMP transients that was found in fiberoptometric recordings was not detected (**Figure 27**). These findings were inconclusive and further experiments will be required. In order to evaluate the capability of the recorded parameters to predict future locomotion, the time shift analysis was established (see 2.4.6). This approach allowed for an assessment of the overlap between recorded parameter and the velocity of the animal.

The time shift analysis was used on the theta parameters and single-unit firing rates. Analyzing GCaMP5G data with this method seemed inappropriate, as the slow off-kinetics of the fluorescence impedes a reliable outcome. Shifting the decay of large and slow GCaMP transients after movement offset would lead to inaccurate assumptions. Instead of specific movement-related transients, large amplitude data would correspond to periods of immobility. Faster activity indicator proteins such as newer isoforms of GCaMP or even voltage sensors would render a time shift analysis of an optical population signal possible (Akerboom et al., 2012; Chen et al., 2013).

Time shifting the parameters extracted from the theta oscillations confirmed the previous findings. Both theta mean power and power of the 7-9 Hz frequency band were changing similarly ahead of the velocity trace, yielding the best overlap after shifting their traces by ~175 ms to future time points. In contrast, theta 4-6 Hz and theta 10-12 Hz did not yield better correlations and are in full agreement with the previous results. An increase in theta amplitude preceding the onset of a movement was described in other studies (Vanderwolf, 1969; Wyble et al., 2004). The presented work adds a suitable measure for evaluating

and quantifying this kinetics. Such an approach was not described previously and could become a valuable tool for prediction analysis. Interestingly, the positively speed-correlated theta peak frequency displayed the best overlap with the velocity trace after being time shifted by +450 ms. This result indicates that locomotion specific increase in theta peak frequency starts already approximately half a second before movement onset. The required time for a complete transition of the field oscillating at 4-6 Hz to faster frequencies is unknown, yet, it has been reported that the increase in frequency prior to locomotion is completed before movement execution (Vanderwolf, 1969). This shift was interpreted as an electrical transition within the forebrain which mediates organization and initiation of voluntary motor behavior (Vanderwolf, 1969). And indeed, the spectral analysis of the LFP recording during the onset interval depicted that the movement associated theta frequencies prevail already before any locomotion begins (**Figure 34**). Thereby, the necessary elevated brain activity for sensory information procession during locomotion is provided (Fuhrmann et al., 2015).

In the next step, the multi-unit activity in the MS was further analyzed in regard of its capability to predict motor behavior. Testing the whole population of recorded septal units yielded a uniform distribution of correlations (**Figure 35B**). This result was similar to the observations gathered from the movement phase alignment of multi-unit activity in the MS. Yet, a more detailed analysis of single units revealed two populations of cells which revealed enhanced correlations with the velocity trace in the time shift analysis (**Figure 35C**). Depending on the time shift which yielded the most positive linear correlation of AP firing rate and velocity of the animal, the group of significant cells could be subdivided into *follower units* (best overlap at time shifts between -50 ms to -1000 ms), *predictor units (*best representation between +50 ms and +1000 ms), and *other units* (combining all remaining units). The averaged slopes for both follower and predictor units depicted clear peaks between -100 to -300 ms (follower) and +100 ms to +300 ms (predictor), respectively. Interestingly, half of the identified follower units showed their best overlap between -100 ms to -300 ms, while the best overlaps of predictor units were distributed more homogeneous over the range of time shifts. The absolute amount of significant follower and predictor units was comparable (~10-14 %). However, the overall proportion of identified significant units was below 25 % of all recorded septal neurons.

Still, given the fact that the MS supposedly contains approximately 10,000 to 20,000 neurons (Yoder and Pang, 2005; Guijarro et al., 2006; Ang et al., 2015), the representation of movement states within the MS is mediated by a large absolute number of cells. My analysis could confirm the existence of septal neurons which adjust their firing rate prior to locomotion, thereby agreeing with the results of the GCaMP5G experiments. The existence of follower units in the MS could be explained by the previously mentioned “replay of ongoing internal activity dynamics”, probably involved in the post-procession of sensory signals (Malvache et al., 2016).

Applying the time shift analysis on the recorded hippocampal multi-activity depicted a strong overlap among the population at time shifts between -200 ms and -500 ms. The analysis of single-units revealed a group of follower units preferentially adjusting their firing rate subsequently to the motor behavior, as well as a group of predictor units preceding the velocity of the animal (**Figure 36**). On average, the population of follower units displayed the most positive slopes around -200 ms to -500 ms. On the other hand, the putative predictor units showed the best overlap with the velocity at time shifts between +200 ms to +500 ms. However, the proportion of cells that showed significant encoding of locomotion constituted more than 70 % of all hippocampal units recorded. This outcome is in agreement with the idea, that the HC is required to adjust its baseline activity in order to process and compute the incoming stream of sensory information during locomotion (Leutgeb and Mizumori, 1999; Hufner et al., 2011). Yet, the large amount of follower units compared to lower number of predictor units clearly outlines the main role of the HC as the central region for memory formation and post-procession of sensory inputs (e.g. spatial information) as a consequence of behavior (Bird and Burgess, 2008).

# 5. Conclusion

In conclusion, this work elucidates the physiological relevance of the septal-hippocampal network for locomotor behavior. It points out, that this circuit contains diversely active neurons, which link their firing to distinct time points during a movement interval. Furthermore, it shows that the network activity increases prior to locomotion and highlights the non-linearity of this activity increase in relation to the animal's velocity despite the observed speed-modulation. Taken together, the results presented here suggest a primary role of the MS during the execution of locomotion and in controlling theta oscillations in the HC. This conclusion is in accordance with previous assumptions about the role of the MS (Dragoi et al., 1999; Borhegyi et al., 2004; Hangya et al., 2009).

Future studies should attempt to compare and correlate the electrical activity patterns of septal and hippocampal neurons simultaneously, rather than in separate experiments. In order to understand this highly efficient network within the brain during behavior, these units need to be molecularly identified and classified into groups that then can be associated to distinct forms of behavior.

# 6. Appendix

## 6.1. Abbreviations

| | |
|---|---|
| **ΔF/F** | Change of fluorescence over baseline fluorescence |
| **µ** | Mean |
| **µ V** | Microvolts |
| **AAV** | Adeno-associated virus |
| **acc** | Movement phase: end of acceleration |
| **AMPA** | α-amino-3-hydroxy-5-methyl-4-isoxazolepropionic acid |
| **AP** | Action potential |
| **$Ca^{2+}$** | $Calcium^{2+}$ |
| **CA1** | Cornu ammonis region 1 |
| **CA2** | Cornu ammonis region 2 |
| **CA3** | Cornu ammonis region 3 |
| **cCA1** | Contralateral CA1 |
| **$ChAT^{+}$** | Choline acetyl transferase-positive |
| **cm** | Centimeter |
| **cre** | Creates-recombination protein |
| **dec** | Movement phase: start of deceleration |
| **DB** | Diagonal band of Broca |
| **DNA** | Deoxyribonucleic acid |
| **DR** | Dorsal raphe nucleus |
| **e.g.** | For example |
| **EC** | Entorhinal cortex |
| **FFT** | Fast Fourier Transformation |
| **$Freq_{rest}$** | Frequency at resting |

| | |
|---|---|
| **$Freq_{run}$** | Frequency at running |
| **g.c.l.** | Granule cell layer |
| **GABA** | γ-aminobutyric-acid |
| **GCaMP5G** | Genetically encoded calcium indicator isoform 5G |
| **GECI** | Genetically encoded calcium indicator |
| **GFP** | Green fluorescent protein |
| **$Glut^{+}$** | Glutamate-positive |
| **HC** | Hippocampus |
| **HCF** | Hippocampal formation |
| **Hz** | Hertz |
| **LC** | Locus coeruleus |
| **LFP** | Local field potential |
| **lx** | loxP sites |
| **m.l.** | Molecular layer |
| **MPO** | Medial preoptic distribution |
| **MS** | Medial septum |
| **ms** | Millisecond |
| **MSDB** | Medial septum and diagonal band of Broca |
| **NC** | Neocortex |
| **neg speed** | Negative speed-correlated |
| **NMDA** | N-Methyl-D-Aspartate |
| **offset** | Movement phase: offset of locomotion |
| **OLM** | Oriens-lacunosum-moleculare |
| **onset** | Movement phase: onset of locomotion |
| **ORF** | Open reading frame |
| **P** | Promotor |

| | |
|---|---|
| **pA** | Poly-A cassette |
| **PC** | Prefrontal cortex |
| **PMC** | Primary motor cortex |
| **pos speed** | Positive speed-correlated |
| **$PV^+$** | Parvalbumin-positive |
| **REM** | Rapid eye movement |
| **RSA** | Rhythmic slow activity |
| **s** | Second |
| **s.l.m.** | Stratum lacunosum moleculare |
| **s.o.** | Stratum oriens |
| **s.p.** | Stratum pyramidalis |
| **s.r.** | Stratum radiatum |
| **SC** | Subiculum |
| **SEM** | Standard error of the mean |
| **Stop** | Stop codon |
| **$T_0$** | Alignment point for movement phase analysis |
| **TH** | Thalamus |
| **$Timelag_{max}$** | Time shift displaying the most positive slope |
| **v** | Velocity |
| **$VGluT2^+$** | Vesicular glutamate transporter isoform 2-positive |
| **VTA** | Ventral tegmental area |
| **WPRE** | Woodchuck hepatitis virus posttranscriptional regulatory element |

## 6.2. Contributions

The experiments and the analysis of the data were done by C.H. The experiments regarding the VGluT2$^{+}$-GCaMP5G recordings have been partly published in *Justus et al*., 2016.

# 7. Bibliography

Agster KL, Burwell RD (2013) Hippocampal and subicular efferents and afferents of the perirhinal, postrhinal, and entorhinal cortices of the rat. Behav Brain Res 254:50-64.

Akerboom J et al. (2013) Genetically encoded calcium indicators for multi-color neural activity imaging and combination with optogenetics. Frontiers in molecular neuroscience 6:2.

Akerboom J et al. (2012) Optimization of a GCaMP calcium indicator for neural activity imaging. The Journal of neuroscience : the official journal of the Society for Neuroscience 32:13819-13840.

Alger BE, Nicoll RA (1982) Feed-forward dendritic inhibition in rat hippocampal pyramidal cells studied in vitro. J Physiol 328:105-123.

Alivisatos AP et al. (2013) Nanotools for neuroscience and brain activity mapping. ACS Nano 7:1850-1866.

Amaral DG, Witter MP (1989) The three-dimensional organization of the hippocampal formation: a review of anatomical data. Neuroscience 31:571-591.

Andersen P, Morris R, Amaral D, Bliss T, O'Keefe J (2007) The hippocampus book. Oxford University Press.

Ang ST, Lee AT, Foo FC, Ng L, Low CM, Khanna S (2015) GABAergic neurons of the medial septum play a nodal role in facilitation of nociception-induced affect. Sci Rep 5:15419.

Barrenechea C, Pedemonte M, Nunez A, Garcia-Austt E (1995) In vivo intracellular recordings of medial septal and diagonal band of Broca neurons: relationships with theta rhythm. Exp Brain Res 103:31-40.

Bender F, Gorbati M, Cadavieco MC, Denisova N, Gao X, Holman C, Korotkova T, Ponomarenko A (2015) Theta oscillations regulate the speed of locomotion via a hippocampus to lateral septum pathway. Nat Commun 6:8521.

Bird CM, Burgess N (2008) The hippocampus and memory: insights from spatial processing. Nat Rev Neurosci 9:182-194.

Bland BH, Vanderwolf CH (1972) Diencephalic and hippocampal mechanisms of motor activity in the rat: effects of posterior hypothalamic stimulation on behavior and hippocampal slow wave activity. Brain research 43:67-88.

Bland SK, Bland BH (1986) Medial septal modulation of hippocampal theta cell discharges. Brain research 375:102-116.

Borhegyi Z, Varga V, Szilagyi N, Fabo D, Freund TF (2004) Phase segregation of medial septal GABAergic neurons during hippocampal theta activity. The Journal of neuroscience : the official journal of the Society for Neuroscience 24:8470-8479.

Brandon MP, Koenig J, Leutgeb JK, Leutgeb S (2014) New and distinct hippocampal place codes are generated in a new environment during septal inactivation. Neuron 82:789-796.

Buzsaki G (1986) Hippocampal sharp waves: their origin and significance. Brain research 398:242-252.

Buzsaki G (2002) Theta oscillations in the hippocampus. Neuron 33:325-340.

Buzsaki G, Acsadi G, Jani A (1980) Differential contribution of fimbria and fornix fibers to behavior. Behav Neural Biol 28:79-88.

Buzsaki G, Leung LW, Vanderwolf CH (1983) Cellular bases of hippocampal EEG in the behaving rat. Brain research 287:139-171.

Campbell NA, Reece JB (2006) Biology 6th edition. Pearson.

Caronia-Brown G, Yoshida M, Gulden F, Assimacopoulos S, Grove EA (2014) The cortical hem regulates the size and patterning of neocortex. Development 141:2855-2865.

Chen TW, Wardill TJ, Sun Y, Pulver SR, Renninger SL, Baohan A, Schreiter ER, Kerr RA, Orger MB, Jayaraman V, Looger LL, Svoboda K, Kim DS (2013) Ultrasensitive fluorescent proteins for imaging neuronal activity. Nature 499:295-300.

Colom LV, Castaneda MT, Reyna T, Hernandez S, Garrido-Sanabria E (2005) Characterization of medial septal glutamatergic neurons and their projection to the hippocampus. Synapse 58:151-164.

Costa C, Sgobio C, Siliquini S, Tozzi A, Tantucci M, Ghiglieri V, Di Filippo M, Pendolino V, de Iure A, Marti M, Morari M, Spillantini MG, Latagliata EC, Pascucci T, Puglisi-Allegra S, Gardoni F, Di Luca M, Picconi B, Calabresi P (2012) Mechanisms underlying the impairment of hippocampal long-term potentiation and memory in experimental Parkinson's disease. Brain 135:1884-1899.

Csicsvari J, Jamieson B, Wise KD, Buzsaki G (2003) Mechanisms of gamma oscillations in the hippocampus of the behaving rat. Neuron 37:311-322.

Deadwyler SA, Foster TC, Hampson RE (1987) Processing of sensory information in the hippocampus. Crit Rev Clin Neurobiol 2:335-355.

Delmaire C, Vidailhet M, Elbaz A, Bourdain F, Bleton JP, Sangla S, Meunier S, Terrier A, Lehericy S (2007) Structural abnormalities in the cerebellum and sensorimotor circuit in writer's cramp. Neurology 69:376-380.

Doherty A (1999) Hippocampal pathways. MRC centre for synaptic plasticity, university of Bristol.

Dragoi G, Carpi D, Recce M, Csicsvari J, Buzsaki G (1999) Interactions between hippocampus and medial septum during sharp waves and theta oscillation in the behaving rat. The Journal of neuroscience : the official journal of the Society for Neuroscience 19:6191-6199.

Freund TF, Antal M (1988) GABA-containing neurons in the septum control inhibitory interneurons in the hippocampus. Nature 336:170-173.

Freund TF, Buzsaki G (1996) Interneurons of the hippocampus. Hippocampus 6:347-470.

Frotscher M, Leranth C (1985) Cholinergic innervation of the rat hippocampus as revealed by choline acetyltransferase immunocytochemistry: a combined light and electron microscopic study. J Comp Neurol 239:237-246.

Fuhrmann F, Justus D, Sosulina L, Kaneko H, Beutel T, Friedrichs D, Schoch S, Schwarz MK, Fuhrmann M, Remy S (2015) Locomotion, Theta Oscillations, and the Speed-Correlated Firing of Hippocampal Neurons Are Controlled by a Medial Septal Glutamatergic Circuit. Neuron 86:1253-1264.

Green JD, Arduini AA (1953) Hippocampal electrical activity in arousal. J Neurophysiol 17:533-557.

Gritti I, Mainville L, Jones BE (1993) Codistribution of GABA- with acetylcholine-synthesizing neurons in the basal forebrain of the rat. J Comp Neurol 329:438-457.

Gritti I, Manns ID, Mainville L, Jones BE (2003) Parvalbumin, calbindin, or calretinin in cortically projecting and GABAergic, cholinergic, or glutamatergic basal forebrain neurons of the rat. J Comp Neurol 458:11-31.

Guijarro C, Rutz S, Rothmaier K, Turiault M, Zhi Q, Naumann T, Frotscher M, Tronche F, Jackisch R, Kretz O (2006) Maturation and maintenance of cholinergic medial septum neurons require glucocorticoid receptor signaling. Journal of neurochemistry 97:747-758.

Hagan JJ, Salamone JD, Simpson J, Iversen SD, Morris RG (1988) Place navigation in rats is impaired by lesions of medial septum and diagonal band but not nucleus basalis magnocellularis. Behav Brain Res 27:9-20.

Haith AM, Pakpoor J, Krakauer JW (2016) Independence of Movement Preparation and Movement Initiation. The Journal of neuroscience : the official journal of the Society for Neuroscience 36:3007-3015.

Hajszan T, Alreja M, Leranth C (2004) Intrinsic vesicular glutamate transporter 2-immunoreactive input to septohippocampal parvalbumin-containing neurons: novel glutamatergic local circuit cells. Hippocampus 14:499-509.

Halasy K, Hajszan T, Kovacs EG, Lam TT, Leranth C (2004) Distribution and origin of vesicular glutamate transporter 2-immunoreactive fibers in the rat hippocampus. Hippocampus 14:908-918.

Hangya B, Borhegyi Z, Szilagyi N, Freund TF, Varga V (2009) GABAergic neurons of the medial septum lead the hippocampal network during theta activity. The Journal of neuroscience : the official journal of the Society for Neuroscience 29:8094-8102.

Hartley T, Lever C, Burgess N, O'Keefe J (2014) Space in the brain: how the hippocampal formation supports spatial cognition. Philos Trans R Soc Lond B Biol Sci 369:20120510.

Hasselmo ME (2005) What is the function of hippocampal theta rhythm?--Linking behavioral data to phasic properties of field potential and unit recording data. Hippocampus 15:936-949.

Hasselmo ME, Bodelon C, Wyble BP (2002a) A proposed function for hippocampal theta rhythm: separate phases of encoding and retrieval enhance reversal of prior learning. Neural Comput 14:793-817.

Hasselmo ME, Hay J, Ilyn M, Gorchetchnikov A (2002b) Neuromodulation, theta rhythm and rat spatial navigation. Neural Netw 15:689-707.

Heck DH, De Zeeuw CI, Jaeger D, Khodakhah K, Person AL (2013) The neuronal code(s) of the cerebellum. The Journal of neuroscience : the official journal of the Society for Neuroscience 33:17603-17609.

Henderson J, Greene E (1977) Behavioral effects of lesions of precommissural and postcommissural fornix. Brain Res Bull 2:123-129.

Hinman JR, Brandon MP, Climer JR, Chapman GW, Hasselmo ME (2016) Multiple Running Speed Signals in Medial Entorhinal Cortex. Neuron 91:666-679.

Holmes G (1917) The symptoms of acute cerebellar injuries due to gunshot injuries. Brain 40:461-535.

Holsheimer J, Boer J, Lopes da Silva FH, van Rotterdam A (1982) The double dipole model of theta rhythm generation: simulation of laminar field potential profiles in dorsal hippocampus of the rat. Brain research 235:31-50.

Hooks BM, Lin JY, Guo C, Svoboda K (2015) Dual-channel circuit mapping reveals sensorimotor convergence in the primary motor cortex. The Journal of neuroscience : the official journal of the Society for Neuroscience 35:4418-4426.

Hufner K, Strupp M, Smith P, Brandt T, Jahn K (2011) Spatial separation of visual and vestibular processing in the human hippocampal formation. Ann N Y Acad Sci 1233:177-186.

Huh CY, Goutagny R, Williams S (2010) Glutamatergic neurons of the mouse medial septum and diagonal band of Broca synaptically drive hippocampal pyramidal cells: relevance for hippocampal theta rhythm. The Journal of neuroscience : the official journal of the Society for Neuroscience 30:15951-15961.

Huxter J, Burgess N, O'Keefe J (2003) Independent rate and temporal coding in hippocampal pyramidal cells. Nature 425:828-832.

Jahn TL, Votta JJ (1972) Locomotion of protozoa. Annu Rev Fluid Mech 4:93-116.

Jun JJ et al. (2017) Fully integrated silicon probes for high-density recording of neural activity. Nature 551:232-236.

Justus D, Dalugge D, Bothe S, Fuhrmann F, Hannes C, Kaneko H, Friedrichs D, Sosulina L, Schwarz I, Elliott DA, Schoch S, Bradke F, Schwarz MK, Remy S (2017) Glutamatergic synaptic integration of locomotion speed via septoentorhinal projections. Nature neuroscience 20:16-19.

Kaifosh P, Lovett-Barron M, Turi GF, Reardon TR, Losonczy A (2013) Septo-hippocampal GABAergic signaling across multiple modalities in awake mice. Nature neuroscience 16:1182-1184.

Kandel ER, Schwartz JH, Jessell TM (2000) Principles of neural science. McGraw-Hill 56890 DOWDOW 0987654.

Kemp JM, Powell TP (1971) The connexions of the striatum and globus pallidus: synthesis and speculation. Philos Trans R Soc Lond B Biol Sci 262:441-457.

Kim SM, Frank LM (2009) Hippocampal lesions impair rapid learning of a continuous spatial alternation task. PloS one 4:e5494.

King C, Recce M, O'Keefe J (1998) The rhythmicity of cells of the medial septum/diagonal band of Broca in the awake freely moving rat: relationships with behaviour and hippocampal theta. The European journal of neuroscience 10:464-477.

Kiss J, Patel AJ, Baimbridge KG, Freund TF (1990) Topographical localization of neurons containing parvalbumin and choline acetyltransferase in the medial septum-diagonal band region of the rat. Neuroscience 36:61-72.

Kiss J, Magloczky Z, Somogyi J, Freund TF (1997) Distribution of calretinin-containing neurons relative to other neurochemically identified cell types in the medial septum of the rat. Neuroscience 78:399-410.

Klausberger T, Marton LF, Baude A, Roberts JD, Magill PJ, Somogyi P (2004) Spike timing of dendrite-targeting bistratified cells during hippocampal network oscillations in vivo. Nature neuroscience 7:41-47.

Knierim JJ, Lee I, Hargreaves EL (2006) Hippocampal place cells: parallel input streams, subregional processing, and implications for episodic memory. Hippocampus 16:755-764.

Kocsis B, Bragin A, Buzsaki G (1999) Interdependence of multiple theta generators in the hippocampus: a partial coherence analysis. The Journal of neuroscience : the official journal of the Society for Neuroscience 19:6200-6212.

Koenig J, Linder AN, Leutgeb JK, Leutgeb S (2011) The spatial periodicity of grid cells is not sustained during reduced theta oscillations. Science 332:592-595.

Kohler C, Chan-Palay V, Wu JY (1984) Septal neurons containing glutamic acid decarboxylase immunoreactivity project to the hippocampal region in the rat brain. Anat Embryol (Berl) 169:41-44.

Kramis R, Vanderwolf CH, Bland BH (1975) Two types of hippocampal rhythmical slow activity in both the rabbit and the rat: relations to behavior and effects of atropine, diethyl ether, urethane, and pentobarbital. Experimental neurology 49:58-85.

Kropff E, Carmichael JE, Moser MB, Moser EI (2015) Speed cells in the medial entorhinal cortex. Nature.

Leao RN, Targino ZH, Colom LV, Fisahn A (2015) Interconnection and synchronization of neuronal populations in the mouse medial septum/diagonal band of Broca. Journal of neurophysiology 113:971-980.

Leao RN, Colom LV, Borgius L, Kiehn O, Fisahn A (2012) Medial septal dysfunction by Abeta-induced KCNQ channel-block in glutamatergic neurons. Neurobiology of aging 33:2046-2061.

Legatt AD, Arezzo J, Vaughan HG, Jr. (1980) Averaged multiple unit activity as an estimate of phasic changes in local neuronal activity: effects of volume-conducted potentials. Journal of neuroscience methods 2:203-217.

Leung LS (1998) Generation of theta and gamma rhythms in the hippocampus. Neurosci Biobehav Rev 22:275-290.

Leung LW, Borst JG (1987) Electrical activity of the cingulate cortex. I. Generating mechanisms and relations to behavior. Brain research 407:68-80.

Leutgeb S, Mizumori SJ (1999) Excitotoxic septal lesions result in spatial memory deficits and altered flexibility of hippocampal single-unit representations. The Journal of neuroscience : the official journal of the Society for Neuroscience 19:6661-6672.

Lewis PR, Shute CC (1967) The cholinergic limbic system: projections to hippocampal formation, medial cortex, nuclei of the ascending cholinergic reticular system, and the subfornical organ and supra-optic crest. Brain 90:521-540.

Li LB, Han LN, Zhang QJ, Sun YN, Wang Y, Feng J, Zhang L, Wang T, Chen L, Liu J (2014) The theta-related firing activity of parvalbumin-positive neurons in the medial septum-diagonal band of Broca complex and their response to 5-HT1A receptor stimulation in a rat model of Parkinson's disease. Hippocampus 24:326-340.

Lorente de Nó R (1934) Studies on the structure of the cerebral cortex II. Continuation of the study of the ammonic system. J Psychol Neurol 46:113-177.

Losonczy A, Zemelman BV, Vaziri A, Magee JC (2010) Network mechanisms of theta related neuronal activity in hippocampal CA1 pyramidal neurons. Nature neuroscience 13:967-972.

Lynch G, Rose G, Gall C (1978) Anatomical and functional aspects of the septo-hippocampal projections. In: Function of the septo-hippocampal system. Elsevier 58:5-24.

Malvache A, Reichinnek S, Villette V, Haimerl C, Cossart R (2016) Awake hippocampal reactivations project onto orthogonal neuronal assemblies. Science 353:1280-1283.

Mank M, Griesbeck O (2008) Genetically encoded calcium indicators. Chem Rev 108:1550-1564.

Manseau F, Danik M, Williams S (2005) A functional glutamatergic neurone network in the medial septum and diagonal band area. J Physiol 566:865-884.

Mattis J, Tye KM, Ferenczi EA, Ramakrishnan C, O'Shea DJ, Prakash R, Gunaydin LA, Hyun M, Fenno LE, Gradinaru V, Yizhar O, Deisseroth K (2011) Principles for applying optogenetic tools derived from direct comparative analysis of microbial opsins. Nature methods 9:159-172.

Mayse JD, Nelson GM, Avila I, Gallagher M, Lin SC (2015) Basal forebrain neuronal inhibition enables rapid behavioral stopping. Nature neuroscience 18:1501-1508.

Meibach RC, Siegel A (1977a) Efferent connections of the septal area in the rat: an analysis utilizing retrograde and anterograde transport methods. Brain research 119:1-20.

Meibach RC, Siegel A (1977b) Efferent connections of the hippocampal formation in the rat. Brain research 124:197-224.

Mizumori SJ, Barnes CA, McNaughton BL (1990) Behavioral correlates of theta-on and theta-off cells recorded from hippocampal formation of mature young and aged rats. Exp Brain Res 80:365-373.

Mizuseki K, Diba K, Pastalkova E, Buzsaki G (2011) Hippocampal CA1 pyramidal cells form functionally distinct sublayers. Nature neuroscience 14:1174-1181.

Morris NP, Harris SJ, Henderson Z (1999) Parvalbumin-immunoreactive, fast-spiking neurons in the medial septum/diagonal band complex of the rat: intracellular recordings in vitro. Neuroscience 92:589-600.

Morris RGM, Hagan JJ (1983) Hippocampal electrical activity and ballistic movement. In: Seifert, W ed Neurobiology of the hippocampus London: Academic Press; .

Müller C, Remy S (2014) Dendritic inhibition mediated by O-LM and bistratified interneurons in the hippocampus. Front Synaptic Neurosci 6:23.

Mysin IE, Kitchigina VF, Kazanovich Y (2015) Modeling synchronous theta activity in the medial septum: key role of local communications between different cell populations. Journal of computational neuroscience 39:1-16.

Nagel G, Ollig D, Fuhrmann M, Kateriya S, Musti AM, Bamberg E, Hegemann P (2002) Channelrhodopsin-1: a light-gated proton channel in green algae. Science 296:2395-2398.

Neychev VK, Fan X, Mitev VI, Hess EJ, Jinnah HA (2008) The basal ganglia and cerebellum interact in the expression of dystonic movement. Brain 131:2499-2509.

Nyakas C, Luiten PG, Spencer DG, Traber J (1987) Detailed projection patterns of septal and diagonal band efferents to the hippocampus in the rat with emphasis on innervation of CA1 and dentate gyrus. Brain Res Bull 18:533-545.

O'Keefe J, Conway DH (1978) Hippocampal place units in the freely moving rat: why they fire where they fire. Exp Brain Res 31:573-590.

Oddie SD, Bland BH (1998) Hippocampal formation theta activity and movement selection. Neurosci Biobehav Rev 22:221-231.

Pare D, Collins DR (2000) Neuronal correlates of fear in the lateral amygdala: multiple extracellular recordings in conscious cats. The Journal of neuroscience : the official journal of the Society for Neuroscience 20:2701-2710.

Pawela C, Brunsdon RK, Williams TA, Porter M, Dale RC, Mohammad SS (2017) The neuropsychological profile of children with basal ganglia encephalitis: a case series. Dev Med Child Neurol 59:445-448.

Penfield W, Milner B (1958) Memory deficit produced by bilateral lesions in the hippocampal zone. AMA Arch Neurol Psychiatry 79:475-497.

Petsche H, Stumpf C, Gogolak G (1962) [The significance of the rabbit's septum as a relay station between the midbrain and the hippocampus. I. The control of hippocampus arousal activity by the septum cells]. Electroencephalogr Clin Neurophysiol 14:202-211.

Pfeiffer K, French AS (2015) Naturalistic stimulation changes the dynamic response of action potential encoding in a mechanoreceptor. Front Physiol 6:303.

Purves D, Augustine GJ, Fitzpatrick D, Katz LC, LaMantia AS, McNamara JO, Williams SM (2001) Neuroscience 2nd edition. Sinauer Associates.

Rivas J, Gaztelu JM, Garcia-Austt E (1996) Changes in hippocampal cell discharge patterns and theta rhythm spectral properties as a function of walking velocity in the guinea pig. Exp Brain Res 108:113-118.

Robinson J, Manseau F, Ducharme G, Amilhon B, Vigneault E, El Mestikawy S, Williams S (2016) Optogenetic Activation of Septal Glutamatergic Neurons Drive Hippocampal Theta Rhythms. The Journal of neuroscience : the official journal of the Society for Neuroscience 36:3016-3023.

Roland JJ, Janke KL, Servatius RJ, Pang KC (2014) GABAergic neurons in the medial septum-diagonal band of Broca (MSDB) are important for acquisition of the classically conditioned eyeblink response. Brain Struct Funct 219:1231-1237.

Salinas E, Romo R (1998) Conversion of sensory signals into motor commands in primary motor cortex. The Journal of neuroscience : the official journal of the Society for Neuroscience 18:499-511.

Scoville WB, Milner B (1957) Loss of recent memory after bilateral hippocampal lesions. J Neurol Neurosurg Psychiatry 20:11-21.

Sherrington CS (1906) The integrative action of the nervous system. New Haven: Yale University Press.

Skaggs WE, McNaughton BL, Wilson MA, Barnes CA (1996) Theta phase precession in hippocampal neuronal populations and the compression of temporal sequences. Hippocampus 6:149-172.

Sotty F, Danik M, Manseau F, Laplante F, Quirion R, Williams S (2003) Distinct electrophysiological properties of glutamatergic, cholinergic and GABAergic rat septohippocampal neurons: novel implications for hippocampal rhythmicity. J Physiol 551:927-943.

Stepan J, Dine J, Eder M (2015) Functional optical probing of the hippocampal trisynaptic circuit in vitro: network dynamics, filter properties, and polysynaptic induction of CA1 LTP. Front Neurosci 9:160.

Stephan A, Laroche S, Davis S (2001) Generation of aggregated beta-amyloid in the rat hippocampus impairs synaptic transmission and plasticity and causes memory deficits. The Journal of neuroscience : the official journal of the Society for Neuroscience 21:5703-5714.

Stewart M, Fox SE (1990) Do septal neurons pace the hippocampal theta rhythm? Trends in neurosciences 13:163-168.

Sun Y, Nguyen AQ, Nguyen JP, Le L, Saur D, Choi J, Callaway EM, Xu X (2014) Cell-Type-Specific Circuit Connectivity of Hippocampal CA1 Revealed through Cre-Dependent Rabies Tracing. Cell reports 7:269-280.

Sutherland RJ, Rodriguez AJ (1989) The role of the fornix/fimbria and some related subcortical structures in place learning and memory. Behav Brain Res 32:265-277.

Swanson LW, Cowan WM (1979) The connections of the septal region in the rat. J Comp Neurol 186:621-655.

Sweeney P, Yang Y (2016) An Inhibitory Septum to Lateral Hypothalamus Circuit That Suppresses Feeding. The Journal of neuroscience : the official journal of the Society for Neuroscience 36:11185-11195.

Unal G, Joshi A, Viney TJ, Kis V, Somogyi P (2015) Synaptic Targets of Medial Septal Projections in the Hippocampus and Extrahippocampal Cortices of the Mouse. The Journal of neuroscience : the official journal of the Society for Neuroscience 35:15812-15826.

Vanderwolf CH (1969) Hippocampal electrical activity and voluntary movement in the rat. Electroencephalogr Clin Neurophysiol 26:407-418.

Vanderwolf CH, Heron W (1964) Electroencephalographic waves with voluntary movement. Arch Neurol 11:379-384.

Wainer BH, Levey AI, Rye DB, Mesulam MM, Mufson EJ (1985) Cholinergic and non-cholinergic septohippocampal pathways. Neuroscience letters 54:45-52.

Wallenstein GV, Hasselmo ME (1997) GABAergic modulation of hippocampal population activity: sequence learning, place field development, and the phase precession effect. Journal of neurophysiology 78:393-408.

Wang Y, Romani S, Lustig B, Leonardo A, Pastalkova E (2015) Theta sequences are essential for internally generated hippocampal firing fields. Nature neuroscience 18:282-288.

Whishaw IQ, Vanderwolf CH (1971) Hippocampal EEG and behavior: effects of variation in body temperature and relation of EEG to vibrissae movement, swimming and shivering. Physiology & behavior 6:391-397.

Whishaw IQ, Vanderwolf CH (1973) Hippocampal EEG and behavior: changes in amplitude and frequency of RSA (theta rhythm) associated with spontaneous and learned movement patterns in rats and cats. Behavioral biology 8:461-484.

Winson J (1972) Interspecies differences in the occurrence of theta. Behavioral biology 7:479-487.

Witter MP, Naber PA, van Haeften T, Machielsen WC, Rombouts SA, Barkhof F, Scheltens P, Lopes da Silva FH (2000) Cortico-hippocampal communication by way of parallel parahippocampal-subicular pathways. Hippocampus 10:398-410.

Wyble BP, Hyman JM, Rossi CA, Hasselmo ME (2004) Analysis of theta power in hippocampal EEG during bar pressing and running behavior in rats during distinct behavioral contexts. Hippocampus 14:662-674.

Yoder RM, Pang KC (2005) Involvement of GABAergic and cholinergic medial septal neurons in hippocampal theta rhythm. Hippocampus 15:381-392.

Zaborszky L, Pang K, Somogyi J, Nadasdy Z, Kallo I (1999) The basal forebrain corticopetal system revisited. Ann N Y Acad Sci 877:339-367.

## Ich bedanke mich herzlichst…

… bei meinem Doktorvater Prof. Dr. Stefan Remy für die unentwegte Unterstützung und wissenschaftliche Inspiration während den letzten Jahren.

… bei Prof. Dr. Walter Witke für sein Interesse an meinem Projekt und die Begutachtung meiner Arbeit.

… bei meiner AG Remy, die neben Wissenschaft und Alltagsstress auf persönlicher Ebene so oft für wunderbare Erinnerungen gesorgt hat und etwas ganz Besonderes ist.

… bei meiner Freundin, die mir in dieser Zeit mit Tat und Rat immer zur Seite stand.

… bei meiner Familie, auf die ich einfach immer zählen konnte.

Danke!